Imperial College London
Department of Chemical Engineering

Complex interfacial and wetting dynamics

Rajagopal Vellingiri

February 2014

Submitted in partial fulfilment of the requirements for the degree of
Doctor of Philosophy in Chemical Engineering of Imperial College London

Copyright Declaration

Abstract

Consider interface evolution in bounded and unbounded settings, namely in the spreading of droplets and stratified gas-liquid flows. A typical prototype consists of the surface-tension-dominated motion of a two-dimensional droplet on a substrate. The case of chemically heterogeneous substrates was examined here. Assuming small slopes, a single evolution equation for the droplet free surface was derived from the Navier-Stokes equations, with the singularity at the contact line being alleviated using the Navier slip condition. The chemical nature of the substrate is incorporated into the system by local variations in the microscopic contact angle. By using the method of matched asymptotic expansions, the flow in the vicinity of the contact lines is matched to that in the bulk of the droplet to obtain a set of coupled ordinary differential equations for the location of the two contact points. The solutions obtained by asymptotic matching are in excellent agreement with the solutions to the full governing evolution equation. The dynamics of the droplet is examined in detail via a phase-plane analysis. A number of interesting features that are not present in homogeneous substrates are observed: multiple droplet equilibria, pinning of contact points on localised heterogeneities, unidirectional motion of droplet and the possibility of stick-slip behaviour of contact points.

Unbounded gas-liquid flows are also often encountered in natural phenomena and applications. The prototypical system considered here consists of a liquid film flowing down an inclined planar substrate in the presence of a co-flowing turbulent gas. The gas and liquid problems are solved independently by making certain reasonable assumptions. The influence of gas flow on the liquid problem is analysed by developing a weighted integral-boundary-layer (WIBL) model, which is valid up to moderate Reynolds numbers. We seek solitary-wave solutions of this model using a pseudo-arclength continuation approach. As a general trend, it is found that the wave speed increases with increasing gas shear and the liquid flow rate. Further insight into the problem is provided by time-dependent computations of the WIBL model.

Finally, the absolute-convective instability of a falling film that is in contact with a counter-current turbulent gas is analysed. The Orr–Sommerfeld (O-S) problem is formulated from the full governing equations and boundary conditions. The O-S problem along

with low-dimensional models, namely, a long-wave and WIBL models are used to explore the linear stability of the gas-liquid system. It is found that for a fixed liquid Reynolds number, at low and high gas flow rates, the system is convectively unstable, and for a range of intermediate gas flow rates we have absolute instability. We supplemented our analysis by doing time-dependent computations of the linearised WIBL model subject to a localised initial condition which showed good agreement. The upper limit of the absolute instability regime predicted by our linear analysis is close to the flooding point obtained from the fully non-linear computations of the WIBL model.

Acknowledgements

First of all, I would like to thank my supervisor Prof. Serafim Kalliadasis for his patience, guidance and motivation at various stages of this work. I also wish to thank him for all his encouragement and support.

I have benefitted from a number of stimulating discussions with Nikos Savva and Dmitri Tseluiko. I am very much grateful to them for their invaluable inputs. I also wish to thank Dr. Krishnan for his much helpful advice, especially during the initial stages of my study.

I want to extend my thanks to David Sibley for proof-reading the thesis. Thanks are also due to present and former group members for their friendship, help and support.

I would like to gratefully acknowledge the Department of Chemical Engineering, Imperial College London for providing me an opportunity to pursue my doctoral degree.

I am indebted to the Marie Curie Initial Training Network – "MULTIFLOW" for their generous financial support through an Early Stage Research Fellowship during the initial three years of my doctoral study.

I would be ungrateful if I did not thank my friends here and in India for their affection and interesting discussions on various topics. And finally I want to thank my parents and brother for all their love and support.

Declaration of Originality

I herewith declare that the research reported in this thesis is original and the work of any other researcher is appropriately acknowledged.

Rajagopal Vellingiri

Contents

List of Figures

1. Introduction

The evolution of interfaces has been studied in a number of contexts, such as in air-water flows (Miles, 1957), tear films (Wong et al., 1996), solidification problems (Mullins and Sekerka, 1964), hydrocarbon transport in long distance pipelines (Joseph et al., 1997), lava flows (Huppert, 1982) and combustion dynamics (Matkowsky and Sivashinsky, 1978), to name a few. The characteristic length and time scales connected with these flow systems can be very different, ranging from a few micrometers and microseconds in microchannel flows to a few kilometers and hours in mantle flows. However, in all these settings, the conditions at the interface play a vital role in determining the overall dynamics of the system. For example, the presence of a temperature gradient along an otherwise stable interface induces flow in the bulk of the viscous liquid through surface tension gradients (Ehrhard and Davis, 1991), which is the well-known Marangoni effect. By nature, all interfacial flows are free-boundary problems, i.e., the location of the boundary is to be determined as a part of the solution to the full problem. This necessitates an accurate representation of the conditions prevailing at the interface. As a general practice, interfaces are either modeled as mathematical surfaces of zero thickness dividing the two phases, or as diffusive with a finite thickness. In the sharp boundary approach, which is one of most widely adopted techniques to model free surface flows, an exact specification of force balance conditions at the interface becomes essential.

1.1. Bounded systems

When the interface is confined in at least one of the flow directions, we refer to them as bounded systems (see figure 1.1a). Some of the most widely explored bounded interfacial systems are droplets (Cristini and Tan, 2004), bubbles (Plesset and Prosperetti, 1977) and antibubbles – that are characterised by a thin air film surrounded by the liquid (Kim and Stone, 2008). Among these, droplets are extensively encountered in nature and industrial applications. Even though droplets are analysed in various settings, their behaviour is found to be noticeably different depending on whether or not they are in contact with a solid wall. The influence of a solid wall on the spreading dynamics is influenced by

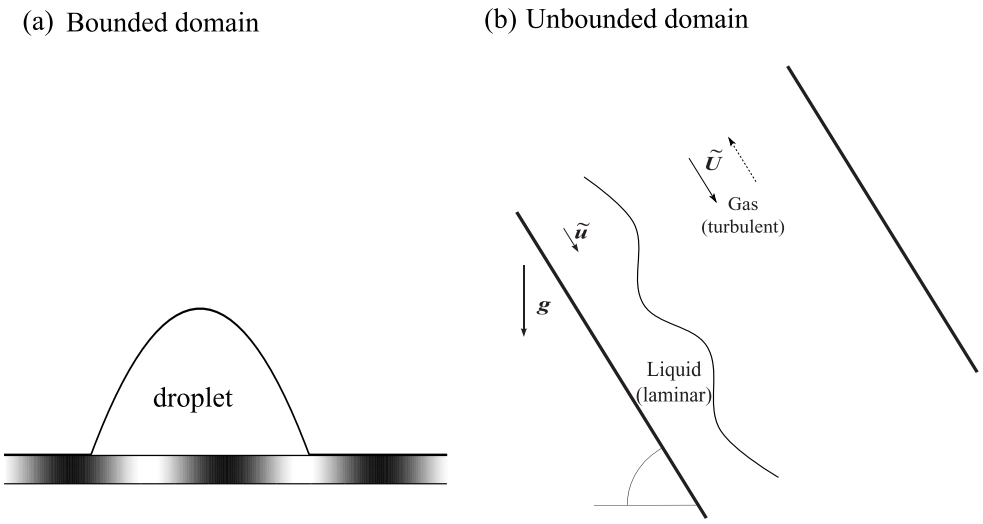

Figure 1.1.: Interface evolution in (a) Bounded setting: Spreading of a droplet on chemically heterogeneous substrate (b) Unbounded setting: Thin film dynamics in the presence of cocurrent (solid line with arrow) and countercurrent (dotted line with arrow) turbulent gas flow.

the phenomena occurring at the contact line, where the solid, liquid and gas come into contact. The wettability of the solid for any given liquid is prescribed by the Young equation (Young, 1805)

$$\sigma_{sg} - \sigma_{\ell s} = \sigma \cos\theta_C, \tag{1.1}$$

which comes from the projection of forces (acting at the contact line) in the direction parallel to the solid surface. Alternatively, equation (1.1), along with the Young-Laplace equation (for the pressure jump) could be derived by a minimisation of the interfacial energies (de Gennes et al., 2004). In equation (1.1), $\sigma_{\ell s}$, σ_{sg} and σ denote the interfacial tensions at the solid-liquid, solid-gas and liquid-gas interfaces respectively, whereas θ_C represents the equilibrium contact angle. A smaller contact angle implies that the system is favourable to wetting (called hydrophilic if the considered liquid phase is water), on the other hand, systems that resist wetting (called hydrophobic) possess large values of θ_C. More specifically, when $\theta_C = 0$, the system is said to be 'completely wetting', whereas $0 \leq \theta_C \leq \pi$ corresponds to 'partial wetting', and for a 'non-wetting' scenario we have $\theta_C = \pi$. Despite the fact that equilibrium droplet configurations could be easily determined for any given contact angle, the dynamics of spreading is yet to be fully understood. The root cause of this difficulty comes from the boundary conditions at the contact line. One of the most generally accepted boundary conditions at a solid liquid interface is that of no-slip,

and by extending it to the contact line for the case of a wedge on a polar coordinate system (r, θ), Huh and Scriven (1971) have shown that the stress at the three-phase contact line becomes infinite due to a $1/r$ singularity, which is clearly nonphysical as it would require an infinite force to submerge a dry solid object in a water bath. This demands an alternative boundary condition at the contact line under the continuum limit.

1.1.1. Models for contact line

Since then various models have been proposed to cure the contact line singularity, and describe the correct dynamical behaviour (de Gennes, 1985; Bonn et al., 2009; Snoeijer and Andreotti, 2013). However, as the physical mechanism at the contact line is not well understood, contact line motion and wetting phenomena remains one of the hotly debated topics (Velarde, 2011). Amongst the numerous approaches, Navier slip (Navier, 1823) is one of the most common. According to this condition, the slip velocity is proportional to the velocity gradient at the solid-liquid interface, with the proportionality constant being a characteristic of the solid surface. Though the contact line motion is allowed through a slip condition at the substrate, nevertheless this approach retains the stress singularity, but is only logarithmic yielding a finite force. There also exist more sophisticated slip models such as the nonlinear slip model of Thompson and Troian (1997) and the inverse slip model of Ruckenstein and Dunn (1977) which also cures the stress singularity in the long-wave limit. Although there are some shortcomings, the wide use and comparative ease of implementation were the key in deciding the use of the Navier slip model for the droplet spreading problem here in chapter 2.

Another conventional approach to model contact lines is to replace the actual contact line with an apparent one. This could be achieved either by manually introducing a thin, constant thickness microscopic film ahead of the spreading droplet (Spaid and Homsy, 1996; Bertozzi and Brenner, 1997) or through a disjoining pressure formalism. In the more sophisticated disjoining pressure approach (Sharma, 1993; Schwartz and Eley, 1998; Thiele et al., 2002; Popescu et al., 2012), molecular effects are incorporated into the disjoining pressure term of the governing equation. The balance of long-range van der Waals forces and short range electrostatic forces in this disjoining pressure term leads to a stable wetting film on the substrate. If we denote the surface potential by $V(h)$, the negative of its derivative with respect to the film thickness 'h', i.e., $\Pi(h)=-V'(h)$ is called the disjoining pressure. By these precursor film approaches, the actual contact line is avoided, hence the force singularity is circumvented.

Another approach that is employed to remove contact line singularity is the diffuse in-

terface approach (Seppecher, 1996; Jacqmin, 2000; Sibley et al., 2013), where the interface is considered to be of finite thickness with the density variation being smooth, and the contact line motion is attributed to the diffusional mass transfer occurring between the two phases. In fact, the interface is defined to be a locus of average densities of both the phases. A significant advantage with the diffuse interface approach is that the original problem no longer remains a free boundary problem, instead the interface is computed from the density contours thus making the numerical treatment convenient.

Some of the other approaches to allow contact line motion within the continuum framework are numerical slip (Renardy et al., 2001), interface formation (Shikhmurzaev, 1993) and evaporation/condensation (Wayner, 1993). Even though all these models postulate remarkably different mechanisms at the contact line, they introduce adhoc/phenomenological parameters that cannot be uniquely determined from existing theory or experiments (for e.g. slip). It was shown that some of these models, namely, slip and precursor film treatments show very similar macroscopic behaviour under appropriate selection of the parameters (Savva and Kalliadasis, 2011). There are more rigorous treatments of the contact line, such as density functional theory (Tarazona and Evans, 1984; Archer, 2009; Pereira and Kalliadasis, 2012) from statistical mechanics that could possibly provide the connecting link between microscopic and macroscopic phenomena.

Nevertheless, placing the complications in the contact line treatment aside for a moment, droplet dynamics are also scrutinised under complicated conditions (Bonn et al., 2009). For a liquid droplet comprising of a solute and a solvent placed on a solid substrate, in the presence of heat transfer, it was shown that the deposition of solids occur close to the contact line, usually known as the coffee-stain effect (Deegan et al., 1997). In another interesting setting, it was demonstrated that a chemical reaction (adsorption/desorption) at the solid-liquid interface results in the motion of the droplet along the substrate (Thiele et al., 2004; John et al., 2005). For wetting on heterogeneous substrates, Wenzel state is usually referred to as one in which the liquid completely fills the cavities, whereas in a Cassie configuration air pockets continue to exist between the droplet and the substrate features (see figure 1.2). Wetting on heterogeneous substrates can also be influenced by the application of an electric field. It was shown that the transition from Cassie to Wenzel state could be achieved by simply varying the applied voltage across the droplet (Mugele et al., 2005), thereby the droplet acting as a switch.

Other complications include topographical features in the substrate (Herminghaus, 2000; Queré, 2008; Savva and Kalliadasis, 2009; Savva et al., 2010), where it was shown that wetting enhancement/inhibition could be achieved by appropriately tuning the substrate microstructures. Variation in chemical composition along the substrate is another feature

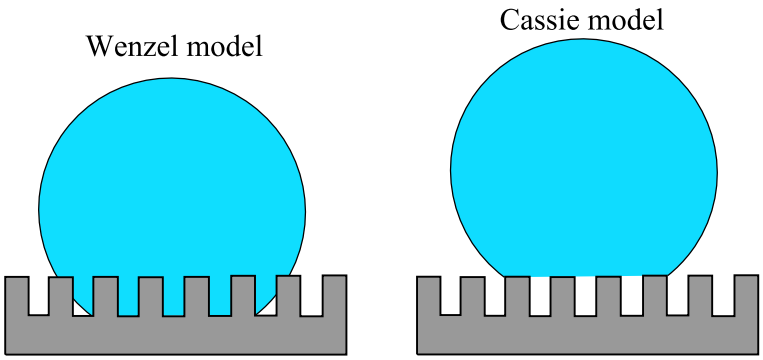

Figure 1.2.: States of a droplet on a solid substrate: Wenzel and Cassie configurations.

that results in interesting dynamics, such as a droplet climbing uphill against gravity (Chaudhury and Whitesides, 1992), non-circular droplet shapes (Heslot et al., 1990), in addition they also find application in polymerisation and bioengineering as microreactors. The behaviour of droplets spreading on chemically heterogeneous substrates is the focus of chapter 2.

1.2. Unbounded systems

An unbounded system is referred to one in which the interface is of infinite extent in the lateral direction (Gumerman and Homsy, 1975; Thiele et al., 2006) (see figure 1.1b). A thin film of liquid flowing along an inclined plate is an example of such a system. Thin liquid films have been extensively studied since the pioneering experiments of Kapitza (1965). In the gravity-driven liquid film, as the inclination angle of the plate is increased beyond a particular value, the film no longer remains flat due to an instability. On increasing the angle of inclination progressively, this simple system was found to exhibit complex dynamic features such as solitary wave solutions through a series of bifurcations (Chang and Demekhin, 2002; Kalliadasis et al., 2012).

1.2.1. Thin film models

The modeling of thin film flows can be traced back to the work of Reynolds (1886), who laid the basis for lubrication theory. Consequently, by making use of the long wavelength nature of the flow, Benney (1966) followed by Lin (1974) and Atherton and Homsy (1976) derived a single partial differential equation for the evolution of the free surface. However, this equation was found to be applicable only close to the point of instability onset, in addition it also suffered a finite-time blowup (Pumir et al., 1983). To cure this shortcoming,

Ooshida (1999) suggested a regularisation based on Padé approximants, but his model underpredicted the solitary wave speeds at moderate Reynolds numbers. Subsequently, to describe stationary waves at moderate Reynolds numbers, the integral boundary layer (IBL) model was proposed by Kapitza (1965) and was later extended to non-stationary settings by Shkadov (1967). The IBL model, which is a set of coupled equations for the film thickness and the local flow rate, combines the assumption of a semi-parabolic velocity profile with the Kármán-Pohlhausen averaging technique of boundary layer theory. Whilst the IBL model is successful in describing nonlinear waves, the deficiency with this model is that it does not correctly predict the instability onset except for the vertical configuration. This discrepancy was remedied by the weighted integral-boundary-layer (WIBL) model of Ruyer-Quil and Manneville (1998, 2000), who showed that the incorrect prediction in the neutral condition results from the assumption of the velocity profile. In the derivation of WIBL model, which is the same as the IBL model but with different coefficients for the inertial terms, they combined the gradient expansion with a weighted residuals technique using polynomial test functions for the velocity field. Further, they also arrived at more sophisticated models by taking into account effects such as viscous dispersion.

1.2.2. Thin films with complexities

As in droplets, thin film flows under complicated conditions such as heating (Kalliadasis et al., 2003; Thiele and Knobloch, 2004), topography (Kalliadasis et al., 2000; Vlachogiannis and Bontozoglou, 2002), electric field (Tseluiko and Papageorgiou, 2006, 2007) and chemical reactions (Trevelyan et al., 2002; Trevelyan and Kalliadasis, 2004) yield intriguing dynamics. By considering a liquid film flowing over a uniformly heated planar wall, Kalliadasis et al. (2000) derived the IBL model for the liquid film, and their computations revealed the existence of solitary waves for all Reynolds numbers. Thiele and Knobloch (2004) showed the presence of drop-like solutions when the substrate was horizontal with uniform heating, and these drops were found to slide when the plate was inclined, also demonstrating the relation existing between these two different states. For flow over a topographical feature, it was shown that a ridge formation occurs due to the capillary pressure gradient just before the liquid enters the trench (Kalliadasis et al., 2000). Vlachogiannis and Bontozoglou (2002) studied gravity-driven thin films over periodic rectangular corrugations by experiments, and reported flow stabilisation at large Reynolds numbers due to the development of complex three dimensional flow structures.

Tseluiko and Papageorgiou (2006, 2007) considered the effect of an applied electric field by developing a long-wave equation with a destabilising non-local contribution from the

electric field. Further, they demonstrated the presence of chaotic solutions even at small Reynolds numbers when the electric field is sufficiently strong. For a thin film flow with a first-order chemical reaction, Trevelyan et al. (2002) showed that an exothermic reaction leads to stabilisation of the free surface, whereas destabilisation was found to occur for an endothermic reaction. Also by constructing a higher-order IBL model, Trevelyan and Kalliadasis (2004) demonstrated the presence of solitary waves for all Reynolds numbers. For extensive reviews of such studies involving additional complexities, the reader is referred to Oron et al. (1997) and Craster and Matar (2009).

1.2.3. Multilayer films

A multilayer flow system comprises of two or more layers of superimposed immiscible liquids flowing down an inclined plane. They are also observed in a number of industrial settings such as slide coating. Such systems are known to display interesting dynamical behaviour through the coupling of one interfacial layer to the other (Pozrikidis, 2004). Tilley et al. (1994a) analysed the stability of a two-layer thin film flow in an inclined channel through a long-wave formulation. By considering air-water and oil-water as model systems, they found that the instability is caused by a shear mode in the water layer. Further, Tilley et al. (1994b) investigated the nonlinear stability of the two-layer system by deriving a Kuramoto-Sivashinsky equation, and tried to explain laminar flooding occurring in a channel. The non-linear stability was further analysed by Kliakhandler (1999) through coupled Kuramoto-Sivashinsky equations and demonstrated the existence of a variety of wave patterns.

1.2.4. Gas liquid flows

When the top liquid layer in a multi-layer setting is replaced by a gas, it results in one of the most widely observed configurations, both in nature and technological applications. One of the earliest works on gas-liquid flows was that of Miles (1957) to model the generation of waves in a water layer by air flow. During the same period, Hanratty and Engen (1957) presented the experimental findings of an air-water system, which showed the transition from a smooth interface to two-dimensional waves. For a co-current flow setting, when the gas velocity is increased beyond a particular value, it results in entrainment of droplets into the gas stream. Woodmansee and Hanratty (1969) tried to explain this phenomena with the appearance of roll waves, which is marked by a significant increase in the thickness of the liquid layer.

Moving on to the counter current setting, for e.g., in a distillation process carried out

on an industrial scale, a thin film of condensate liquid flows down the column exchanging mass with the upflowing vapour. An increase in the vapour flow rate beyond a particular value results in the liquid flow reversing direction. This is also known as flooding which is considered detrimental to the process operation. Although there are a number of empirical correlations connecting the liquid and gas velocities during this transition with the physical and geometrical parameters, the mechanism is not well understood. However, there are a few studies (McQuillan et al., 1985; Jayanti et al., 1996; Pantzali et al., 2008) that associate flooding with an increase in the amplitude of the interfacial waves. By adopting this definition for flooding, Tseluiko and Kalliadasis (2011) developed a theoretical framework to analyse this phenomena by solving the gas and liquid problems. The dynamics of a gravity-driven thin liquid film in the presence of a cocurrent turbulent gas is analysed in chapter 3, and the stability of the liquid film in a countercurrent setting is the focus of chapter 4.

1.3. Structure of the thesis

This thesis is organised into five chapters. In the current introduction chapter, we motivate the study of interfaces in bounded and unbounded settings. Subsequently, three problems are presented to analyse interfacial evolution, the first one on a bounded domain and the other two on unbounded domains.

In the second chapter, we study the spreading of two-dimensional droplets on chemically heterogeneous substrates. The work in this chapter is based on our published work (Vellingiri et al., 2011). We begin with the Navier-Stokes equation along with appropriate boundary conditions, and derive a single evolution equation for the droplet free surface. The chemical nature of the substrate is incorporated into the system dynamics through the boundary conditions at the contact lines. Subsequently, by taking the droplet motion to be surface-tension-dominated and assuming slip at the contact line, we arrive at a set of coupled ordinary differential equations (ODEs) for the contact points through a matched asymptotic analysis. The solutions of the ODEs are compared with the solution of the full governing equation by using a pseudo-spectral numerical scheme. Further, to extract generic features on the equilibrium and the dynamics, a phase plane analysis of the ODEs is presented. A number of examples are provided, such as pinning at localised heterogeneities, contact angle hysteresis, stick-slip motion of the contact lines and a unidirectional motion of the droplet.

Chapter three deals with the dynamics of a liquid film in the presence of co-current gas flow. This work being published in Vellingiri et al. (2013). First, the literature on thin

film studies and co-current gas liquid flows are reviewed. By considering the liquid film to be laminar and gas flow to be turbulent, followed by a few reasonable assumptions, the gas and liquid problems are decoupled and solved independently using an approach similar to that of Tseluiko and Kalliadasis (2011), which was on a countercurrent setting. The effect of gas flow on the liquid film dynamics enters through the boundary conditions at the gas-liquid interface. The dynamics of the liquid problem is analysed by developing a weighted integral-boundary-layer model which is a set of coupled equations for the evolution of film thickness and the local flow rate. In order to understand the stability of the flat liquid film subjected to a gas flow in the same direction as that of the liquid, a linear stability analysis is presented. Two types of solutions that the system exhibits, namely a solitary-wave and a periodic travelling wave are analysed through numerical continuation based on a pseudo arclength continuation algorithm. A comparison of the numerical continuation results with time-dependent computations is provided.

In chapter four, the linear stability analysis of a liquid film in the presence of a countercurrent turbulent gas is described. By assuming a parallel base flow in the liquid layer, the Orr–Sommerfeld (O-S) problem that is valid for all values of Reynolds number and wavenumber is formulated. Combining the O-S problem with low-dimensional models, namely a long-wave model and a weighted integral-boundary-layer-model proposed by Tseluiko and Kalliadasis (2011), a linear stability analysis of the flat film solution is presented. After providing an introduction to the concept of absolute and convective instabilities, a methodology to analyse such instabilities is developed (Fokas and Papageorgiou, 2005). This methodology is further applied to the O-S equation and the low-dimensional models, and the regimes of absolute and convective instabilities are computed using a continuation algorithm. The results from the analysis are compared with time-dependent computations of the linearised weighted integral-boundary-layer model subject to a localised initial condition. Chapter five comprises a summary of the work and some future directions.

We note finally that the chapters 2, 3 and 4 may be read independently of one another, with notational conventions defined in each chapter as they arise.

2. Droplet spreading on chemically heterogeneous substrates

The majority of this chapter is based on Vellingiri et al. (2011), which was co-authored with Nikos Savva and Serafim Kalliadasis. The derivation of the appropriate long-wave equations is also included here for the interested reader.

2.1. Introduction

Wetting phenomena find importance in many technological applications such as oil recovery, inkjet printing, cooling of industrial reactors, and microfluidic devices. They are also widely observed in nature, such as in the self-cleaning behaviour of lotus plant leaves (Blossey, 2003) and insects walking on water (Bush and Hu, 2006). As a consequence, wetting, and its particular utilisation to manipulate droplet behaviour, has been an active topic of both theoretical and experimental research for several decades (Dussan, 1979; de Gennes, 1985; Darhuber and Troian, 2005; Bonn et al., 2009).

One of the most extensively studied topics in wetting is the spreading of liquid droplets on ideally homogeneous solid substrates (Tanner, 1979; Voinov, 1976; Neogi and Miller, 1982; Cox, 1986; McHale et al., 1995; Ehrhard and Davis, 1991). But substrates are not generally homogeneous, instead they are characterised by topographical defects/variations which can cause substantial changes to the spreading dynamics, e.g. they can pin the contact points at localised features, induce stick-slip behaviour and hysteresis or cause the droplet to move in a preferred direction. Recent studies of spreading on topographical substrates, either structured or random, both theoretical (Savva and Kalliadasis, 2009; Savva et al., 2010, 2011a,b) and experimental (Chu et al., 2010; Malvadkar et al., 2010), demonstrated many of these effects. Noteworthy is that current technological advances allow control of topographical features down to microscopic scales (Queré, 2005; Nie and Kumacheva, 2008). The droplet spreading dynamics is also significantly influenced by the presence of additional effects and complexities, such as thermocapillarity (Ehrhard and Davis, 1991), evaporation (Sodtke et al., 2008) or electric fields (Decamps and Coninck,

2000).

Of equal importance are the effects of chemical heterogeneities on the spreading dynamics. One of the first studies that examined droplet equilibria on flat chemically heterogeneous substrates was that by Cassie (1948). By using energetic/thermodynamic arguments, he obtained an effective contact angle θ_C that accounts for the areas occupied by different substrate chemistries. For example, when the substrate consists of only two different materials, he showed that

$$\cos\theta_C = \beta\cos\alpha_{s,1} + (1-\beta)\cos\alpha_{s,2}, \tag{2.1}$$

where β is the area fraction of material 1 and $\alpha_{s,1}$, $\alpha_{s,2}$ are the equilibrium contact angles on substrates made of materials 1 and 2, respectively. The general applicability of equation (2.1) has been recently the subject of a vigorous debate (Gao and McCarthy, 2007; McHale, 2007; Nosonovsky, 2007; Panchagnula and Vedantam, 2007; Marmur and Bittoun, 2009; Gao and McCarthy, 2009). It is generally accepted that this expression holds in an "averaged sense" (Swain and Lipowsky, 1998) and cannot describe quantitatively all possible cases (it is solely based on thermodynamics without any fluid dynamics). Indeed, a number of studies (Crawford et al., 1987; Yamauchi et al., 1996; Woodward et al., 2000; Larsen and Taboryski, 2009) with chemically heterogeneous substrates has demonstrated that the agreement of equation (2.1) with experiments is only qualitative.

Experimental studies with chemically heterogeneous substrates also observe that the contact points of the droplet tend to pin on localised chemical defects – much like the topographical substrates case mentioned earlier – as shown for instance in the work of Cubaud and Fermigier (2004). Another commonly reported feature of chemically heterogeneous substrates is that of a preferential droplet motion in the presence of favourable wettability gradients (Chaudhury and Whitesides, 1992; Ichimura et al., 2000). If these are sufficiently strong, they can even move a droplet against gravity on an inclined plane (Chaudhury and Whitesides, 1992). More recent experimental studies examined spreading over striped chemical substrates (Gau et al., 1999; Lèopoldés and Bucknall, 2005; Bliznyuk et al., 2009). They reported preferential spreading along the substrate stripes and they also identified the possibility of pinning a sufficiently small droplet along a stripe as well as of stick-slip behaviour for strong wettability contrasts between the heterogeneities.

At the theoretical front, several studies have examined wetting of chemically heterogeneous substrates. The early study by Greenspan (1978) examined the effects of a wettability gradient on the motion of a three-dimensional viscous droplet by imposing a spatial variation on the equilibrium contact angle. The equation for the droplet motion was ob-

tained from the long-wave limit of the Stokes regime and a slip model was utilised to remove the stress singularity associated with a moving contact line (Huh and Scriven, 1971). Greenspan also prescribed an empirical law that relates the contact line speed with the apparent contact angle. Other studies resorted to thermodynamic/energetic arguments and/or postulated equations. For example, the study by Joanny and de Gennes (1984) considered weak, localised chemical defects, using force balance equations along the contact line (but the weak heterogeneity limit precludes the possibility of contact angle hysteresis). Brochard (1989) also employed force balance and energy arguments to deduce the wetting characteristics of a two-dimensional droplet in terms of the spreading coefficient along the substrate. Using energy minimisation techniques, Brandon and Marmur (1996) presented the contact angle hysteresis of a two-dimensional droplet on chemically patterned surfaces. The work of Moulinet et al. (2002) investigated the contact line dynamics on chemically heterogeneous substrates via postulated equations and under the assumption that it exhibits similar features with avalanche dynamics, but their theoretical results failed to agree with their experiments.

Schwartz and Eley (1998) examined the motion of a three-dimensional droplet on chemically heterogenous substrates by utilising the long-wave limit of the Stokes regime and by taking the equilibrium contact angle to be a prescribed function of position on the substrate as Greenspan did. However, instead of slip, a constant-thickness precursor film model was utilised to remove the stress singularity at the moving contact lines. The precursor film was obtained from the balance of the attractive and repulsive intermolecular forces of the disjoining pressure model these authors adopted. Thiele and Knobloch (2006a,b) used a similar precursor film model and focused on pinning and depinning of two-dimensional droplets on heterogeneous substrates. The wettability defects were modeled by introducing variations in the attractive part of the disjoining pressure. They demonstrated that it is possible for an advancing contact point to get pinned at less hydrophilic regions and for a receding contact point to get pinned at more hydrophilic ones, obtaining also the various depinning transitions in the presence of imposed driving forces, such as body forces or temperature gradients. By solving the Stokes equation using a boundary element technique, Herde et al. (2012) analysed the depinning behaviour of a two-dimensional droplet that makes large contact angles with the substrate. In their formulation, they employed a Navier slip condition, combining with a spatially varying microscopic contact angle at the contact line to account for the heterogeneous nature of the solid surface. Other studies utilised the Lattice-Boltzmann method to perform simulations of spreading of nanodroplets on specific wettability configurations. For example, Huang et al. (2008) investigated conditions under which alternating high and low wet-

tability regions can induce a unidirectional motion, whereas Kusamaataja and Yeomans (2007) performed computations on substrates with stripped regions of different equilibrium contact angles. In a recent study, Varagnolo et al. (2013), through a combination of experiments and numerical simulations, elucidated the characteristic stick-slip motion of a droplet sliding down a heterogeneous substrate comprising of alternating stripes of hydrophilic and hydrophobic regions.

In the present chapter we perform a detailed and systematic investigation of two-dimensional droplet spreading over flat but chemically heterogeneous substrates with the aim to elucidate qualitatively the effects of substrate chemistry on wetting. We begin with a long-wave expansion of the Navier-Stokes equations, and remove the stress singularity associated with a moving contact line using a slip model. We reduce the nonlinear free boundary value problem to a system of ordinary differential equations (ODEs) for the two contact points, which is a considerably simpler problem to solve numerically. One of the novel aspects of our study is that it facilitates the extraction of generic equilibrium and dynamic features via a phase plane analysis which would not have been possible by a direct numerical treatment of the long-wave model. There are a few studies (Pismen and Pomeau, 2004; Glasner and Witelski, 2003, 2005) which are based on the disjoining pressure approach that developed reduced order models dealing with droplet interaction (coarsening or separation) through the precursor film connecting them. However, consideration of such droplet interactions is not possible in our present study which is based on the slip model.

The analysis builds on the singular perturbation methodology developed by Hocking (1983) and by Savva and Kalliadasis (2009) for droplet spreading over ideally homogeneous and topographical substrates, respectively. The validity of the analysis is in the limit of very small capillary numbers. This is not only a realistic assumption as many spreading experiments fall within the low-capillary-number regime, but allows us to treat the droplet motion as a quasistatic one which in turn allows for analytical progress. Like Greenspan (1978), the quasistatic assumption has also been invoked by Glasner (2005), who obtained three-dimensional droplet profiles via a boundary integral formulation, but had nevertheless imposed the contact line velocity as a function of the apparent contact angle.

This chapter is divided into five sections. In section 2.2 we formulate the problem from the original governing equations and boundary conditions, followed by an asymptotic analysis of the system in 2.3. In section 2.4.1 we offer comparisons of the numerical solution of the full partial differential equation (PDE) and the equations obtained by asymptotic matching. In section 2.4.2, we present a detailed investigation of the phase portrait of the two contact lines. The last section 2.5 provides concluding remarks of the

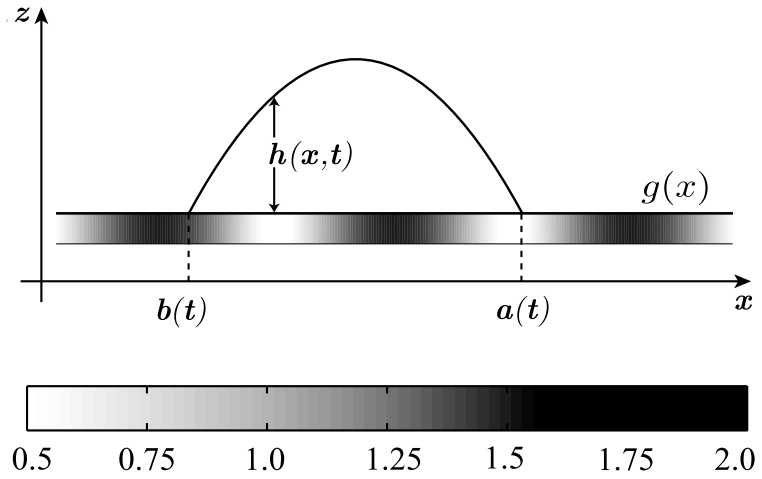

Figure 2.1.: Schematic of a two-dimensional droplet spreading on a chemically heterogeneous substrate.

current investigation.

2.2. Problem formulation

2.2.1. Governing equations

Consider a droplet spreading on a flat horizontal chemically heterogeneous substrate. The cross-section of the droplet lies in the x-z plane and is of infinite extent in the y-direction. This resembles a cylindrical droplet whose length is much larger than its radius. The effect of gravity can be neglected by taking the droplet to be smaller than the capillary length, $\sqrt{\sigma/\rho g}$, where σ is the surface tension of the liquid-gas interface. We will start from the Navier-Stokes equations for the velocity $\mathbf{u} = (u, v)$ and the pressure p:

$$\rho\left(\partial_t \mathbf{u} + \mathbf{u}\cdot\nabla\mathbf{u}\right) = -\nabla p + \mu\nabla^2\mathbf{u}, \tag{2.2}$$

$$\nabla\cdot\mathbf{u} = 0, \tag{2.3}$$

with the no-penetration condition at the bottom wall

$$v = 0 \quad \text{at} \quad z = 0. \tag{2.4}$$

For the tangential velocity at the solid surface, we choose to impose the Navier slip condition:

$$u = \lambda\partial_z u \quad \text{at} \quad z = 0, \tag{2.5}$$

where λ is the slip length. At the free surface of the droplet, the stress balance conditions are to be satisfied. For the tangential stress balance, we have

$$\hat{\mathbf{t}} \cdot (\mathbf{T} - \mathbf{T}_{\text{ext}}) \cdot \hat{\mathbf{n}} - \hat{\mathbf{t}} \cdot \sigma (\nabla \cdot \hat{\mathbf{n}}) \hat{\mathbf{n}} = 0 \quad \text{at} \quad z = h, \tag{2.6}$$

where $\mathbf{T}$ is the total stress tensor, $\hat{\mathbf{t}}$ and $\hat{\mathbf{n}}$ are the unit tangent and normal to the droplet free surface respectively. For a Newtonian fluid, the total stress tensor is given by $\mathbf{T} = -p\mathbf{I} + 2\mu\mathbf{E}$ with $\mathbf{E}$ being the rate of strain tensor. The unit tangent and normal vectors can be written as

$$\hat{\mathbf{t}} = \frac{(1, \partial_x h)}{\sqrt{1 + (\partial_x h)^2}}, \tag{2.7}$$

$$\hat{\mathbf{n}} = \frac{(-\partial_x h, 1)}{\sqrt{1 + (\partial_x h)^2}}. \tag{2.8}$$

By taking the viscosity of the gas (outer fluid) to be much smaller than that of the spreading droplet, $\mu_{\text{ext}} \ll \mu$, and making the substitutions, equations (2.7)–(2.8) in equation (2.6) implies

$$-4 (\partial_x u) (\partial_x h) + (\partial_z u + \partial_x v) \left[1 - (\partial_x h)^2\right] = 0 \quad \text{at} \quad z = h. \tag{2.9}$$

The normal stress balance condition is given by

$$\hat{\mathbf{n}} \cdot (\mathbf{T} - \mathbf{T}_{\text{ext}}) \cdot \hat{\mathbf{n}} - \hat{\mathbf{n}} \cdot \sigma (\nabla \cdot \hat{\mathbf{n}}) \hat{\mathbf{n}} = 0 \quad \text{at} \quad z = h, \tag{2.10}$$

which reduces to

$$p_{\text{ext}} - p - 2\mu \left[1 + (\partial_x h)^2\right]^{-1} \left[(\partial_x u) \left(1 - (\partial_x h)^2\right) + (\partial_z u + \partial_x v) \partial_x h\right] - \sigma \partial_{xx} h \left[1 + (\partial_x h)^2\right]^{-3/2} = 0, \tag{2.11}$$

where p_{ext} is the pressure of the surrounding gas that is assumed to be constant. This is followed by the kinematic condition

$$\partial_t h + u|_{z=h} \partial_x h = 0. \tag{2.12}$$

As we have introduced the free surface h in our analysis, we need additional conditions. Therefore, at the three-phase contact line (point in two dimensions), the height h vanishes:

$$h = 0 \quad \text{at} \quad x = a(t), b(t), \tag{2.13}$$

where $a(t)$ and $b(t)$ are the location of contact points that vary with time.

The chemical nature of the substrate enters into the problem through the contact angle boundary conditions. The microscopic (static) contact angle observed at lengthscales of the order of slip length is imposed to vary along x, can be represented as $G = \tan\alpha_s\, g(x/L)$. Here, α_s is some reference contact angle and L is the length scale associated with the cross-sectional area of the droplet. Therefore, the slope of the droplet free surface at the left contact point is given by

$$\partial_x h = G(b) \quad \text{at} \quad x = b(t), \tag{2.14}$$

and at the right contact point, we have

$$\partial_x h = -G(a) \quad \text{at} \quad x = a(t). \tag{2.15}$$

The case of a chemically homogeneous substrate can be recovered by setting $g = 1$. Finally, for the mass conservation we have

$$\int_{b(t)}^{a(t)} h\, dx = A. \tag{2.16}$$

2.2.2. Non-dimensionalisation

The above equations are made non-dimensional by rescaling

$$x \to Lx; \qquad z \to L\tan\alpha_s\, z; \qquad u \to U\, u \tag{2.17a}$$

$$v \to U\tan\alpha_s\, v; \qquad t \to \frac{3\mu L}{\sigma\tan^3\alpha_s} t; \qquad p \to \frac{\mu U}{L\tan^2\alpha_s} p, \tag{2.17b}$$

$$\lambda \to \frac{L\tan\alpha_s}{3}\lambda; \qquad h \to L\tan\alpha_s\, h \tag{2.17c}$$

where U is the characteristic velocity of the fluid in the x direction, which can also be taken as the average contact line velocity, and L is a measure of the base length of the droplet defined by the droplet cross-sectional area, A:

$$L = \sqrt{\frac{A}{2\tan\alpha_s}}. \tag{2.18}$$

This leads to the following dimensionless parameters:

$$Re_m = \frac{\rho U L}{\mu}; \qquad C = \frac{\mu U}{\sigma}; \qquad \epsilon = \tan\alpha_s. \tag{2.19}$$

The parameter Re_m is the modified Reynolds number that signifies the ratio of inertial to viscous forces, whereas C is the capillary number that compares viscous forces to surface tension.

The dimensionless form of the governing equations (2.2)–(2.3) are

$$\epsilon^2 Re_m \left(Ca^{-1}\partial_t u + u\partial_x u + v\partial_y u\right) = -\partial_x p + \partial_{zz} u + \epsilon^2 \partial_{xx} u, \tag{2.20}$$

$$\epsilon^3 Re_m \left(Ca^{-1}\partial_t v + u\partial_x v + v\partial_y v\right) = -\partial_z p + \epsilon^2 \partial_{zz} v + \epsilon^4 \partial_{xx} v, \tag{2.21}$$

$$\partial_x u + \partial_y v = 0. \tag{2.22}$$

This is supplemented by the interfacial boundary conditions, namely the tangential stress balance (2.9)

$$-4\epsilon^2 \left(\partial_x u\right)\left(\partial_x h\right) + \left(\partial_z u + \epsilon^2 \partial_x v\right)\left[1 - \epsilon^2 \left(\partial_x h\right)^2\right] = 0 \quad \text{at} \quad z = h, \tag{2.23}$$

and the normal stress balance (2.11),

$$p_{\text{ext}} - p - 2\epsilon^2 \left[1 + \epsilon^2 \left(\partial_x h\right)^2\right]^{-1} \left[\left(\partial_x u\right)\left(1 - \epsilon^2 \left(\partial_x h\right)^2\right) + \left(\partial_z u + \epsilon^2 \partial_x v\right)\partial_x h\right] - Ca^{-1}\partial_{xx} h \left[1 + \epsilon^2 \left(\partial_x h\right)^2\right]^{-3/2} = 0, \tag{2.24}$$

where $Ca = 3\epsilon^{-3} C$ is the rescaled capillary number such that $Ca \sim \mathcal{O}(1)$. The kinematic condition (2.12) becomes

$$Ca^{-1}\partial_t h + u|_{z=h}\partial_x h = 0, \tag{2.25}$$

along with the no penetration and Navier slip conditions at the solid surface. The contact angle condition (2.14)–(2.15) becomes

$$\partial_x h = g(b) \quad \text{at} \quad x = b(t), \tag{2.26a}$$

$$\partial_x h = -g(a) \quad \text{at} \quad x = a(t), \tag{2.26b}$$

along with the unchanged vanishing droplet thickness condition at the contact points.

Finally, for the mass conservation equation (2.16) we have

$$\int_{b(t)}^{a(t)} h\, dx = 2. \tag{2.27}$$

Long-wave expansion

By considering a partially wetting fluid, the contact angles can be taken to be very small. We exploit this property by taking $\epsilon \ll 1$, and do a long-wave expansion of the velocity and pressure fields u, v, p about this small parameter as

$$u = u^{(0)} + \epsilon\, u^{(1)} + \cdots \tag{2.28a}$$

$$v = v^{(0)} + \epsilon\, v^{(1)} + \cdots \tag{2.28b}$$

$$p = p^{(0)} + \epsilon\, p^{(1)} + \cdots \tag{2.28c}$$

We make the substitutions (2.28a)–(2.28c) in the dimensionless governing equations and the boundary conditions. Assuming that $\epsilon^2 Re_m \ll 1$, at the leading order we have

$$\partial_x u^{(0)} + \partial_z v^{(0)} = 0, \tag{2.29}$$

$$-\partial_x p^{(0)} + \partial_{zz} u = 0, \tag{2.30}$$

$$\partial_z p^{(0)} = 0. \tag{2.31}$$

The above set of equations (2.29)–(2.31) are the Stokes equations applicable for slow flows. Though we could have taken them as the starting point in our analysis, nevertheless we proceeded with their derivation here for completeness.

The leading order boundary conditions are:

$$v^{(0)} = 0 \quad \text{at} \quad z = 0, \tag{2.32a}$$

$$u^{(0)} - \lambda \partial_z u^{(0)} = 0 \quad \text{at} \quad z = 0, \tag{2.32b}$$

$$\partial_z u^{(0)} = 0 \quad \text{at} \quad z = h, \tag{2.32c}$$

$$p_{\text{ext}} - p^{(0)} = -Ca^{-1} \partial_{xx} h \quad \text{at} \quad z = h. \tag{2.32d}$$

Our immediate objective is to reduce the above set of equations to a single evolution equation for the droplet thickness. For convenience, we neglect the superscripts in the above equations. As a first step, using equation (2.30) in (2.32d), and on further integration

we get

$$u = -\frac{1}{Ca}\partial_{xxx}h\left[\frac{z^2}{2} - hz - \lambda h\right]. \tag{2.33}$$

Making use of Leibniz rule in equation (2.29), we get the height-averaged continuity equation

$$Ca^{-1}\partial_t h + \partial_x\left(\int_0^{h(x,t)} u\, dz\right) = 0, \tag{2.34}$$

which can be further simplified to obtain a single equation for the evolution of droplet thickness:

$$\partial_t h + \partial_x\left[h^2(h+\lambda)\partial_{xxx}h\right] = 0. \tag{2.35}$$

This is supplemented with the boundary conditions (2.13), (2.26a), (2.26b) and the integral condition (2.27). In general, there is no restriction on the form of the microscopic contact angle, $g(x)$, apart from requiring that it is $\mathcal{O}(1)$, its derivatives are continuous, and that its variations occur at lengthscales that are much longer than the slip length, λ.

Similar to other studies employing a slip condition (see e.g. Hocking (1983); Savva and Kalliadasis (2009)), we anticipate sharp boundary layers in the vicinity of the moving contact points, where the slope of the free surface changes abruptly from the microscopic contact angle to an apparent contact angle in the bulk. As a consequence, an asymptotic analysis may be appropriately employed to deduce equations for the two moving contact points.

2.3. Matched asymptotics

To proceed, we restrict our attention in the regime $Ca \ll 1$, which is equivalent to assuming that $|\dot{a}| = |da/dt| \ll 1$ and $|\dot{b}| = |db/dt| \ll 1$ in dimensionless units. In the bulk of the droplet, which we call the *outer region*, the motion is dominated by capillarity, whereas near the contact lines, in the *inner regions*, slip is predominant. By considering the dynamics in these disparate lengthscales and matching asymptotically their corresponding behaviours we shall obtain expressions for the spreading rates, $\dot{a}$ and $\dot{b}$.

2.3.1. Outer region

Away from the contact lines, slip is negligible. Hence, in the outer region, equation (2.35) simplifies to

$$\partial_t h + \partial_x\left[h^3\partial_{xxx}h\right] = 0. \tag{2.36}$$

Since the slope conditions depend on the details of the flow field in the vicinity of the contact lines, the solution to equation (2.36) in the outer region is to be determined subject to the conditions (2.13) and (2.27). Treating $\dot{a}$ and $\dot{b}$ as the small parameters of the problem, we introduce a quasistatic expansion of the form

$$h\left(x,t\right)=h_0\left(x,a,b\right)+\dot{a}h_1\left(x,a,b\right)+\dot{b}h_2\left(x,a,b\right)+\cdots, \tag{2.37}$$

where the time dependence of h comes from the contact line positions varying with time. Our next important task is to find the asymptotic behaviour of $h(x,t)$, as the contact points, $x=a(t)$ and $x=b(t)$, are approached. To $\mathcal{O}(\dot{a}^0,\dot{b}^0)$, we obtain the following equation for h_0:

$$\partial_{xxx}h_0=0. \tag{2.38}$$

Solving equation (2.38) subject to (2.13) and (2.27) results in the simple parabolic profile

$$h_0=\frac{\phi}{(a-b)}\left(a-x\right)\left(x-b\right), \tag{2.39}$$

where

$$\phi=\mp(\partial_x h_0)|_{x=a(t),\,b(t)}=12/(a-b)^2 \tag{2.40}$$

is the apparent contact angle, which, like $g(x)$, is $\mathcal{O}(1)$, as required by the chosen scales of our non-dimensionalisation. To consider the next-order terms, we take $\partial_t h_0=\dot{a}\,\partial_a h_0+\dot{b}\,\partial_a h_0$. From the $\mathcal{O}(\dot{a},\dot{b})$ terms, we obtain

$$\partial_{xxx}h_1=\frac{a-b}{\phi^2\left(a-x\right)^2\left(x-b\right)}, \tag{2.41a}$$

$$\partial_{xxx}h_2=\frac{a-b}{\phi^2\left(a-x\right)\left(b-x\right)^2}, \tag{2.41b}$$

for h_1 and h_2, respectively. Both differential equations are to be solved subject to homogeneous boundary conditions, namely

$$h_1=h_2=0\quad\text{at}\quad x=a\left(t\right),b\left(t\right), \tag{2.42a}$$

$$\int_b^a h_1\,dx=\int_b^a h_2\,dx=0. \tag{2.42b}$$

By successive integration of equations (2.41a) and (2.41b), and on applying the corresponding conditions in (2.42a) and (2.42b), h_1 and h_2 can simply be obtained. However, we are interested in the leading-order behaviour of their slopes as $x\to a$ and $x\to b$.

Hence, we have that

$$\partial_x h_1 \sim \begin{cases} -\dfrac{1}{\phi^2}\ln\left(\mathrm{e}^2\dfrac{a-x}{a-b}\right), & \text{as } x \to a(t), \\ \dfrac{1}{\phi^2}, & \text{as } x \to b(t), \end{cases} \tag{2.43a}$$

$$\partial_x h_2 \sim \begin{cases} \dfrac{1}{\phi^2}, & \text{as } x \to a(t), \\ -\dfrac{1}{\phi^2}\ln\left(\mathrm{e}^2\dfrac{x-b}{a-b}\right), & \text{as } x \to b(t), \end{cases} \tag{2.43b}$$

where $\mathrm{e} = \exp(1)$. The neglected terms are $\mathcal{O}(\eta \ln \eta)$, where $\eta = x - b$, when $x \to b(t)$ or $\eta = a - x$, when $x \to a(t)$. The idea is to match the slope of the outer solution with the inner one. By combining equation (2.39) with equations (2.43a) and (2.43b), we obtain the leading-order slope of the outer solution as the contact points are approached:

$$-\partial_x h \sim \phi + \frac{\dot{a}}{\phi^2}\ln\left(\mathrm{e}^2\frac{a-x}{a-b}\right) - \frac{\dot{b}}{\phi^2}, \qquad \text{as} \qquad x \to a\,(t)\,, \tag{2.44}$$

$$\partial_x h \sim \phi - \frac{\dot{b}}{\phi^2}\ln\left(\mathrm{e}^2\frac{x-b}{a-b}\right) + \frac{\dot{a}}{\phi^2}, \qquad \text{as} \qquad x \to b\,(t)\,. \tag{2.45}$$

These asymptotic expansions in the outer region are to be matched with their corresponding expansions in the inner region. The matching will be done within some overlap regions such that ϕ is the dominant term in equations (2.44) and (2.45), and the x-dependent logarithmic terms are the higher-order corrections in their asymptotic expansions.

2.3.2. Inner region

The details of the solution close to the contact lines cannot be captured by the outer solution we just determined. Therefore, we need to look into the dynamics of the inner region where the effect of slip is predominant. The width of these inner regions is $\mathcal{O}(\lambda)$. Hence, to examine the dynamics near the right contact point $x = a(t)$, we introduce the inner variables:

$$\Phi = \frac{h}{\lambda} \quad \text{and} \quad \xi = \frac{a-x}{\lambda}\,g(a). \tag{2.46}$$

By expressing equation (2.35) in terms of Φ and ξ we obtain

$$\dot{a}\partial_\xi \Phi + g^3(a)\partial_\xi\left[\Phi^2\left(\Phi+1\right)\partial_{\xi\xi\xi}\Phi\right] = 0 \tag{2.47}$$

to $\mathcal{O}\left(\lambda^0\right)$, where, again, the variations of $g(x)$ are assumed to occur at lengthscales that are much longer than λ. The boundary conditions, in terms of inner variables are given by

$$\Phi|_{\xi=0} = 0 \quad \text{and} \quad \partial_\xi \Phi|_{\xi=0} = 1, \tag{2.48}$$

which are supplemented with the requirement that as we move towards the droplet bulk the linear terms dominate, i.e.

$$\Phi/\xi^2 \to 0 \text{ as } \xi \to \infty. \tag{2.49}$$

As in the outer region, we assume that the droplet dynamics in the inner region is also quasistatic. This allows us to expand Φ in equation (2.47) as

$$\Phi = \Phi_0 + \dot{a}\Phi_1 + \cdots . \tag{2.50}$$

By taking the leading-order inner solution to be a wedge, i.e. $\Phi_0 = \xi$, the equation for Φ_1 becomes

$$\partial_{\xi\xi\xi}\Phi_1 = -\frac{1}{g^3(a)\xi(\xi+1)}, \tag{2.51}$$

to be solved subject to $\Phi_1|_{\xi=0} = \left(\partial_\xi \Phi_1\right)|_{\xi=0} = 0$ and $\Phi_1/\xi^2 \to 0$ as $\xi \to \infty$. With these conditions, the leading-order slope of Φ_1 as we move away from the contact line is given by

$$\partial_\xi \Phi_1 \sim \frac{1+\ln\xi}{g^3(a)}, \quad \text{as} \quad \xi \to \infty. \tag{2.52}$$

Hence, the asymptotic behaviour of $\partial_\xi \Phi$ as $\xi \to \infty$ becomes

$$\partial_\xi \Phi \sim 1 + \frac{\dot{a}}{g^3(a)}\left(1+\ln\xi\right), \quad \text{as} \quad \xi \to \infty. \tag{2.53}$$

Expressing equation (2.53) in terms of the outer variables implies

$$-\partial_x h \sim g(a) + \frac{\dot{a}}{g^2(a)} \ln\left(\mathrm{e} g(a)\frac{a-x}{\lambda}\right), \quad \text{as} \quad \frac{a-x}{\lambda} \to \infty. \tag{2.54}$$

Likewise, to obtain $\partial_x h$ as we move away from the other contact point at $x = b(t)$, we follow similar arguments to obtain

$$\partial_x h \sim g(b) - \frac{\dot{b}}{g^2(b)} \ln\left(\mathrm{e} g(b)\frac{x-b}{\lambda}\right), \quad \text{as} \quad \frac{x-b}{\lambda} \to \infty, \tag{2.55}$$

2.3.3. Matching

Our objective is to match the outer solution (2.44) and (2.45) with the corresponding inner solution (2.54) and (2.55) within some overlap region. But we can readily see that the coefficients in front of the x-dependent logarithmic terms do not match. This necessitates the presence of an intermediate region, where there is a bending of the interface due to viscous forces, to properly match the outer and inner regions. Alternatively, matching can be done by taking the cube of the slopes, i.e. $(\partial_x h)^3$ instead of $\partial_x h$. Therefore, the leading-order behaviour of $(\partial_x h)^3$ in the outer region near the contact line $x = a(t)$ becomes

$$-(\partial_x h)^3 \sim \phi^3 + 3\dot{a}\left[\ln\left(\mathrm{e}^2\frac{a-x}{a-b}\right) - \frac{\dot{b}}{\dot{a}}\right], \qquad \text{as} \qquad x \to a\,(t)\,. \tag{2.56}$$

Likewise, the leading-order behaviour of $(\partial_x h)^3$ in the inner region is

$$-(\partial_x h)^3 \sim g^3(a) + 3\dot{a}\left[1 + \ln\left(g(a)\frac{a-x}{\lambda}\right)\right], \quad \text{as} \quad \frac{a-x}{\lambda} \to \infty. \tag{2.57}$$

Matching the above two expressions (2.56) and (2.57) we obtain

$$\frac{\phi^3 - g^3(a)}{3} = \dot{a}\ln\left(g(a)\frac{a-b}{\mathrm{e}\lambda}\right) + \dot{b}. \tag{2.58}$$

By similar arguments, we match (2.45) and (2.55) to obtain

$$\frac{\phi^3 - g^3(b)}{3} = -\dot{b}\ln\left(g(b)\frac{a-b}{\mathrm{e}\lambda}\right) - \dot{a}. \tag{2.59}$$

Equations (2.58) and (2.59) constitute a system of linear equations for the contact line speeds $\dot{a}$ and $\dot{b}$, from which we obtain

$$\dot{a} = \frac{\delta_a \ln\left(g(b)\frac{a-b}{\mathrm{e}\lambda}\right) + \delta_b}{\ln\left(g(a)\frac{a-b}{\mathrm{e}\lambda}\right)\ln\left(g(b)\frac{a-b}{\mathrm{e}\lambda}\right) - 1}, \tag{2.60a}$$

$$\dot{b} = -\frac{\delta_b \ln\left(g(a)\frac{a-b}{\mathrm{e}\lambda}\right) + \delta_a}{\ln\left(g(a)\frac{a-b}{\mathrm{e}\lambda}\right)\ln\left(g(b)\frac{a-b}{\mathrm{e}\lambda}\right) - 1}, \tag{2.60b}$$

where,

$$\delta_a = \frac{\phi^3 - g^3(a)}{3}, \quad \delta_b = \frac{\phi^3 - g^3(b)}{3}, \tag{2.61}$$

and ϕ is the apparent contact angle given by equation (2.40). We can readily see from equations (2.60a)–(2.60b) that the droplet reaches equilibrium only when both δ_a and δ_b vanish, i.e. when the local contact angles become equal to the apparent contact angle. This also implies that in the absence of contact angle hysteresis due to other effects, equilibrium can only be attained if both angles at the contact points are equal to each other. Pismen and Thiele (2006) developed an asymptotic theory for the motion of a droplet driven by wettability gradients, that is incorporated into the system dynamics through a spatially varying disjoining pressure. They considered different asymptotic behaviours for the advancing and receding intermediate (mesoscopic) solutions that are to be matched to the inner (microscopic) region leading to asymmetric droplet shapes, but in the limit of weak driving the droplet shapes were found to be symmetric.

As a result of the asymptotic analysis employed, we were able to reduce a nonlinear fourth order PDE to a set of coupled ODEs for the leading-order contact line speeds. We also need to emphasise that the dimensionless slip length λ has to be sufficiently small to produce meaningful results. If λ is not sufficiently small, the asymptotic analysis would fail in describing the droplet dynamics. This can be demonstrated by considering the simple case of symmetric spreading, i.e. spreading when $g(x)$ is an even function, and the initial condition $a(0) = -b(0)$. Here we have $b(t) = -a(t)$, and $a(t)$ is found by solving the ODE

$$\frac{\phi^3 - g^3(a)}{3} = \dot{a} \ln\left(g(a)\frac{2a}{\mathrm{e}^2\lambda}\right). \tag{2.62}$$

If $\phi > g(a)$, physically we expect to have advancing contact points, i.e. $\dot{a} > 0$. For this to occur, the logarithmic term must be always positive and this happens for sufficiently small λ. If λ is not small, equation (2.62) may predict a receding contact point, which is clearly non-physical.

2.4. Results

2.4.1. Dynamics

Comparison with full solution

Before looking into the detailed dynamics of spreading for specific heterogeneous substrates, we first compare its solution with that of the full PDE, (2.35), obtained numeri-

cally. The solution to the full PDE is based on a numerical scheme that involves spectral differentiation (Trefethen, 2000) in space, and an adaptive, semi-implicit stepping along time. This follows along similar lines of the scheme outlined in Savva and Kalliadasis (2009). The details are also mentioned here in Appendix A for completeness.

For all cases presented in what follows, the slip length is fixed at $\lambda = 10^{-5}$, unless otherwise stated. The contact points of the droplet are initially located at $a(0) = -b(0) = 1$. In figure 2.2, we show the evolution of the contact points when $g(x) = 1 + 0.8 \sin 4x$, where we observe an excellent agreement between the solutions to the PDE and the system of ODEs. Initially, both contact points advance, but at later times the left contact point recedes before eventually reaching equilibrium. The minor difference between the two solutions at the onset may be attributed to the relatively higher initial contact point speeds, that lie beyond the regime of validity of the matched asymptotics. In fact, for the matching to be effective, it can be observed from equations (2.60a)–(2.60b) that the contact line speeds $\dot{a}, \dot{b}$ have to be $\mathcal{O}(1/|\ln \lambda|)$. However, it is evident that equations (2.60a)–(2.60b) are able to satisfactorily capture the leading-order dynamics of equation (2.35). For a weaker heterogeneity profile, e.g. for $g(x) = 1 + 0.05 \sin 4x$, there is an

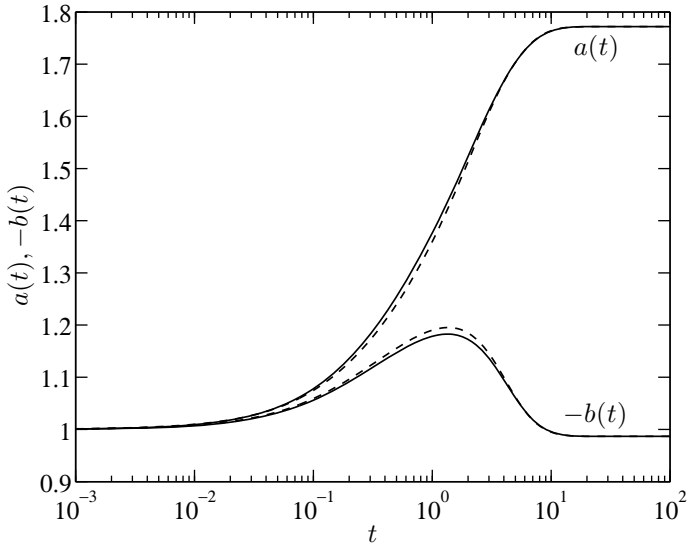

Figure 2.2.: Evolution of contact points when $\lambda = 10^{-5}$ and $a(0) = -b(0) = 1$ for $g(x) = 1 + 0.8 \sin 4x$. Solid curves correspond to the solution of the coupled system of ODEs, (2.60a)–(2.60b); dashed curves correspond to the solution of the PDE, (2.35).

improved agreement between the two solutions shown in figure 2.3, as they are nearly indistinguishable. Now we observe a different behaviour: the left contact point advances

towards equilibrium, whereas recession is observed for the right contact point.

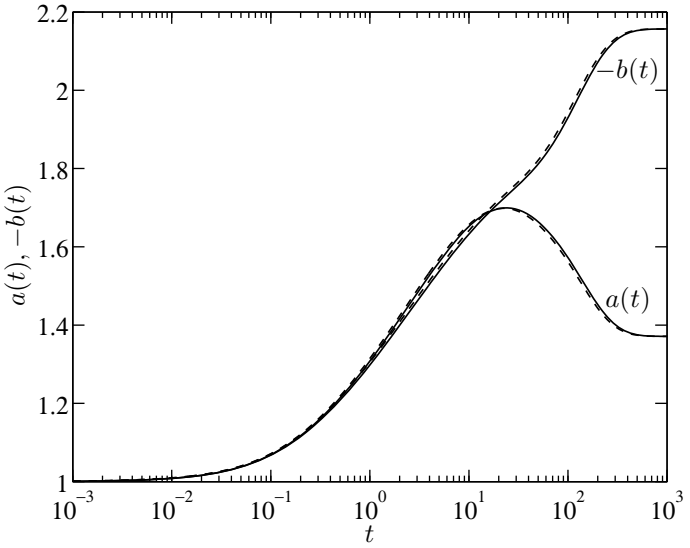

Figure 2.3.: Evolution of contact points when $\lambda = 10^{-5}$ and $a(0) = -b(0) = 1$ for $g(x) = 1 + 0.05 \sin 4x$. Solid curves correspond to the solution of the coupled system of ODEs, (2.60a)–(2.60b); dashed curves correspond to the solution of the PDE, (2.35).

In general, a droplet avoids the less hydrophilic regions and moves towards more hydrophilic ones, in agreement with the results of previous studies (Glasner, 2005; Thiele and Knobloch, 2006a). This effect is demonstrated with the heterogeneity profile $g(x) = 1.5 - 0.5 \tanh 50(x + 1)$, $a(0) = 1.5$ and $b(0) = -1$. Figure 2.4(a) shows the evolution curve for the contact points of the droplet based on equations (2.60a)–(2.60b), which also exhibit excellent agreement with the solution to the PDE (2.35). Figure 2.4(b) depicts the corresponding droplet shapes at different times. For initial times, the left contact point is nearly pinned where the substrate wettability changes abruptly, and the right contact point advances. It should be noted here that the droplet never reaches equilibrium, as the left contact point eventually depins, and the droplet is driven towards $+\infty$ keeping its radius nearly constant. However, the rate at which this occurs is exponentially small. Hence, in a more realistic setting, the droplet may be easily stopped by a tiny substrate defect, either chemical or topographical.

Despite the overall excellent agreement exhibited in figures 2.3 and 2.4 for the solutions to equations (2.60a)–(2.60b) and (2.35), it should be emphasised that there may also exist cases for which their solutions are markedly different. To understand why this occurs, one needs to investigate the phase-plane dynamics of equation (2.60) in detail, as done in a re-

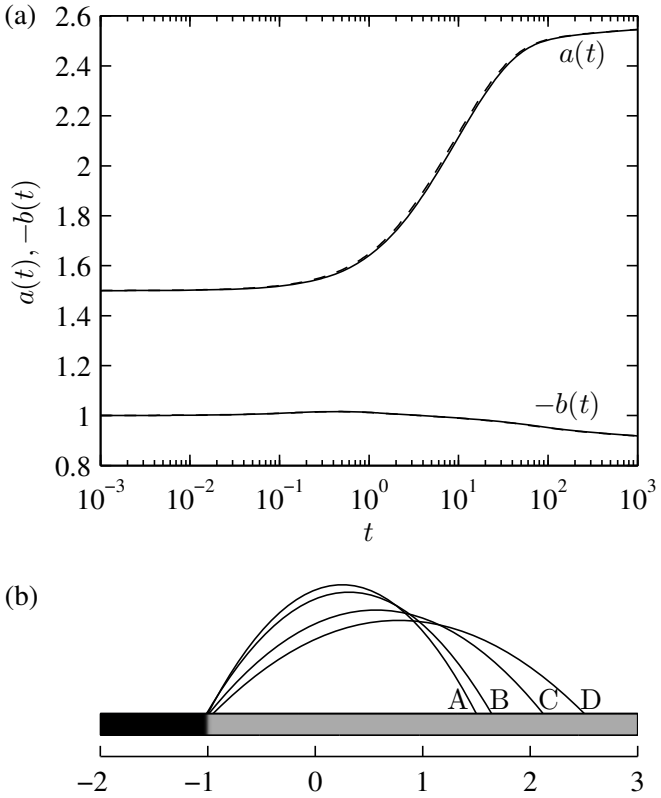

Figure 2.4.: (a) Evolution of contact points on the substrate $g(x)$=$1.5-0.5\tanh 50(x+1)$, $\lambda = 10^{-5}$. Solid curves correspond to the solution of the coupled equations (2.60a)-(2.60b) obtained from matching, dashed curves correspond to the solution of the full PDE, (2.35) (b) Evolution of the droplet free surface; curves A–D correspond to times $t = 0, 1, 10, 1000$, respectively.

cent study for topographical substrates (Savva and Kalliadasis, 2011), where it was found that solutions to the governing PDE may deviate significantly from the solutions to the equations obtained by matched asymptotics, when the contact points of the droplet are initially located close to the boundaries of the basins of attraction of different fixed points. This is due to the fact that even a small perturbation, that is inherent in an asymptotic analysis due to our neglecting of the higher-order terms, may drive the dynamics to an entirely different equilibrium. To illustrate this effect, we consider in figure 2.5 the case when $g(x) = 1 + 0.4 \sin 4x$. We readily see that the contact points obtained by solving the equations resulting from the matching and those obtained by the PDE, evolve in a different manner, eventually driving the droplet to different equilibria. We shall resume our discussion of the phase plane, when investigating the nature of the droplet equilibria in the following sections.

Effect of slip

Having established with numerical experiments the validity of the ODEs obtained by matching, we will now consider the effect of slip on the dynamics. Slip originates from processes occurring at molecular lengthscales and in our model we have assumed that it is constant everywhere. Even though a space-dependent λ might have been somewhat more realistic, we chose to keep it constant. This simplifies our analysis, after all our principal aim is to study the qualitative characteristics of the dynamics. Besides, slip does not affect the equilibria and their stability. Moreover, equations (2.60a)–(2.60b) indicate that the speed of contact points is only logarithmically dependent on λ and as a consequence the influence of λ on the approach to equilibrium is generally weak.

To show how precisely the dynamics depend on λ, we performed simulations using equations (2.60a)–(2.60b) for a substrate with $g(x) = 1 + 0.8 \sin 4x$ and two slip lengths differing by a factor of 100, namely $\lambda_1 = 2 \times 10^{-5}$ and $\lambda_2 = 2 \times 10^{-3}$. In figure 2.6(a) we show the evolution of the moving contact points when $a(0) = -b(0) = 1$ and observe that the overall qualitative behaviour is not affected by the different slip, despite the significantly faster speeds of the contact point for the larger slip length, λ_2 (see figure 2.6(b)). This qualitative agreement is generally expected, even if the disparity between the slip lengths is large. However, there can also exist cases, for which different slip lengths yield significantly different dynamics, for initial conditions located near the saddle point manifolds, as previously mentioned when comparing with solutions to the full PDE. To illustrate such effects, we show in figure 2.7(a) the evolution of $a(t)$ and $b(t)$ resulting

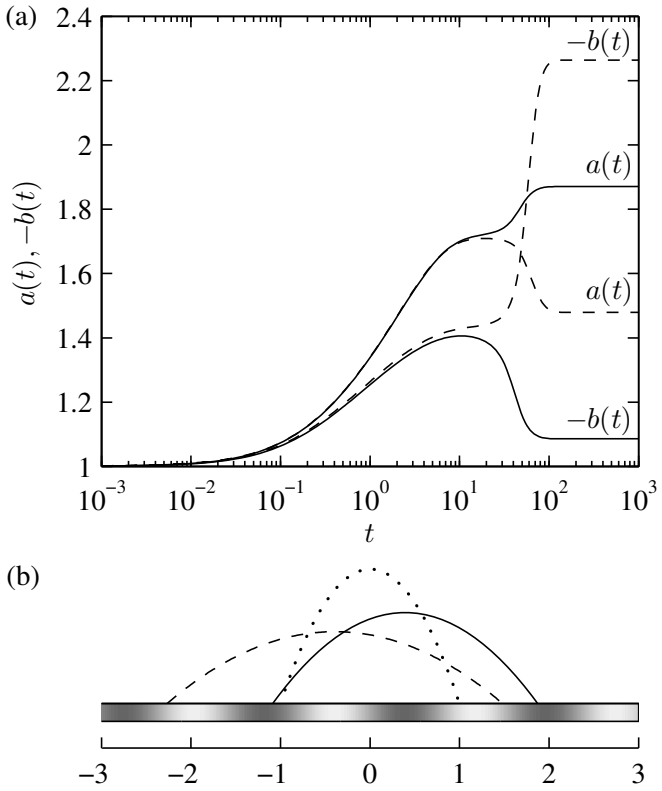

Figure 2.5.: Evolution of contact points of the droplet on the substrate $g(x) = 1+0.4\sin 4x$, $\lambda = 10^{-5}$ with $a(0) = -b(0) = 1$. (a) Solid curves correspond to the solution of the ODEs obtained by matching, (2.60a)–(2.60b); dashed curves are the solution of the PDE, (2.35). A comparison of the two solutions shows that the left contact point, $b(t)$, always advances for the PDE, whereas for the ODEs it exhibits recession at later times. At equilibrium, both contact points obtained from the PDE are shifted leftward compared to those obtained from the ODEs (higher $-b(t)$ and lower $a(t)$). (b) The corresponding equilibrium droplet profiles. The dotted curve shows the initial droplet position. The substrate is shaded according to the colorbar of figure 2.1

.

from equations (2.60a)–(2.60b) for a substrate with $g(x) = 1 + 0.3 \sin 8x$ and the same parameters as in figure 2.6. We now observe that the change in λ is sufficient to lead the droplet to a different equilibrium in the long-time limit (see figure 2.7(b)).

A significant difference in the slip lengths can also change the character of transition for a particular class of substrates (Herde et al., 2012). In figure 2.8 we plot the time evolution of the contact points by solving the full PDE for the heterogeneous substrate $g(x) = 1 + 0.3 \sin 10x$ when $a(0) = -b(0) = 1$, but with different slip lengths given by $\lambda_1 = 5 \times 10^{-5}$ and $\lambda_2 = 5 \times 10^{-2}$. It can be observed that the droplet equilibria for the considered slip lengths λ_1 and λ_2 are completely different.

Stick-slip and hysteresis-like effects

For the substrate $g(x) = 1 + 0.3 \sin 100x$, $a(0) = -b(0) = 1$, in which the variations in microscopic contact angle occur at shorter lengthscales, we observe from figure 2.9(a) that the speed of the contact points exhibit fluctuations in time, before eventually vanishing in the long-time limit. This behaviour is manifested as a brief sticking and slipping of the contact points, which may also be visualised in the evolution plot of the ratio of the apparent to microscopic contact angles (see figure 2.9(b)). Typically, the sticking and slipping of the contact points becomes more common when both the wavelength of the heterogeneities and their amplitude are small, i.e. when the number of equilibria accessible to the droplet increase. Even though hysteresis in the contact angle was not assumed in our model (i.e. the existence of both an advancing and a receding critical angle), it is still possible to observe a hysteresis-like effect induced by the chemical heterogeneities. This is due to the presence of multiple equilibria that are able to pin the droplet to different stable states. This effect is better demonstrated with a plot of the apparent contact angle as a function of the contact line speed, as shown in figure 2.10. Two curves are shown there: the first corresponds to initially advancing contact points ($a(0) = -b(0) = 1$) and the second to initially receding contact points ($a(0) = -b(0) = 3$). It is worth emphasising the disparity in the speeds of the receding and advancing contact points, which appears to be a common feature for both chemical heterogeneities and topographical substrates (Savva and Kalliadasis, 2009). In the end, we observe that two distinct equilibrium angles are attained, differing by $\Delta\phi \approx 0.51$. As with the stick-slip behaviour, this hysteresis-like effect is more likely as the possible stable states become more dense. We shall return to this and related effects in our discussion on the phase-plane dynamics that follows.

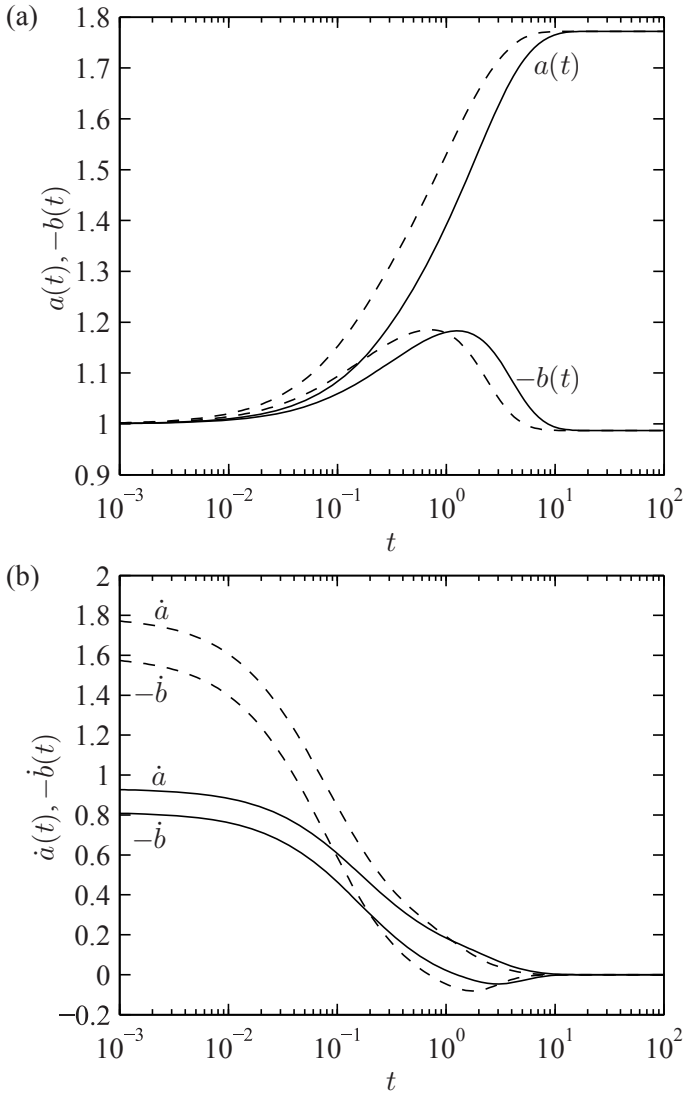

Figure 2.6.: Effect of λ: spreading on a substrate with $g(x)=1+0.8\sin 4x$ when $\lambda_1 = 2\times 10^{-5}$ (solid curves) and $\lambda_2 = 2\times 10^{-3}$ (dashed curves). (a) The evolution of the contact points of the droplet when $a(0) = -b(0) = 1$. (b) The corresponding velocities of the contact points.

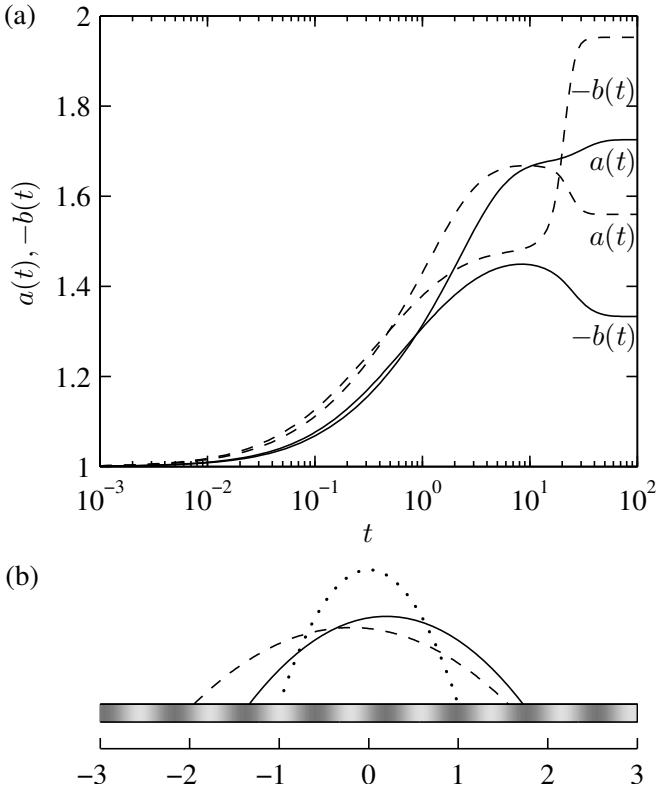

Figure 2.7.: Effect of λ: spreading on a substrate with $g(x)=1+0.3\sin 8x$, when $\lambda_1 = 2\times 10^{-5}$ (solid curves) and $\lambda_2 = 2\times 10^{-3}$ (dashed curves). (a) The evolution of the contact points of the droplet when $a(0) = -b(0) = 1$. (b) The corresponding equilibrium droplet profiles; the dotted curve refers to the initial droplet shape. The substrate is shaded according to the color bar of figure 2.1.

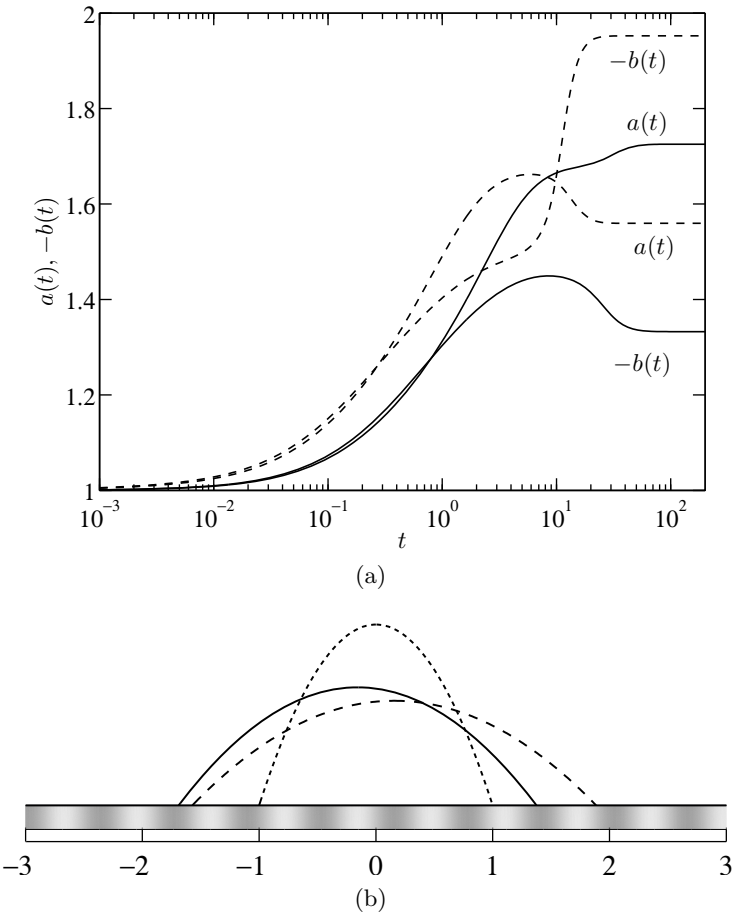

Figure 2.8.: Effect of λ: spreading on a substrate with $g(x)=1+0.3\sin 10x$, when $\lambda_1 = 5\times 10^{-5}$ (solid curves) and $\lambda_2 = 5\times 10^{-2}$ (dashed curves). (a) The evolution of the contact points of the droplet when $a(0) = -b(0) = 1$. (b) The corresponding equilibrium droplet profiles; the dotted curve refers to the initial droplet shape. The substrate is shaded according to the color bar of figure 2.1.

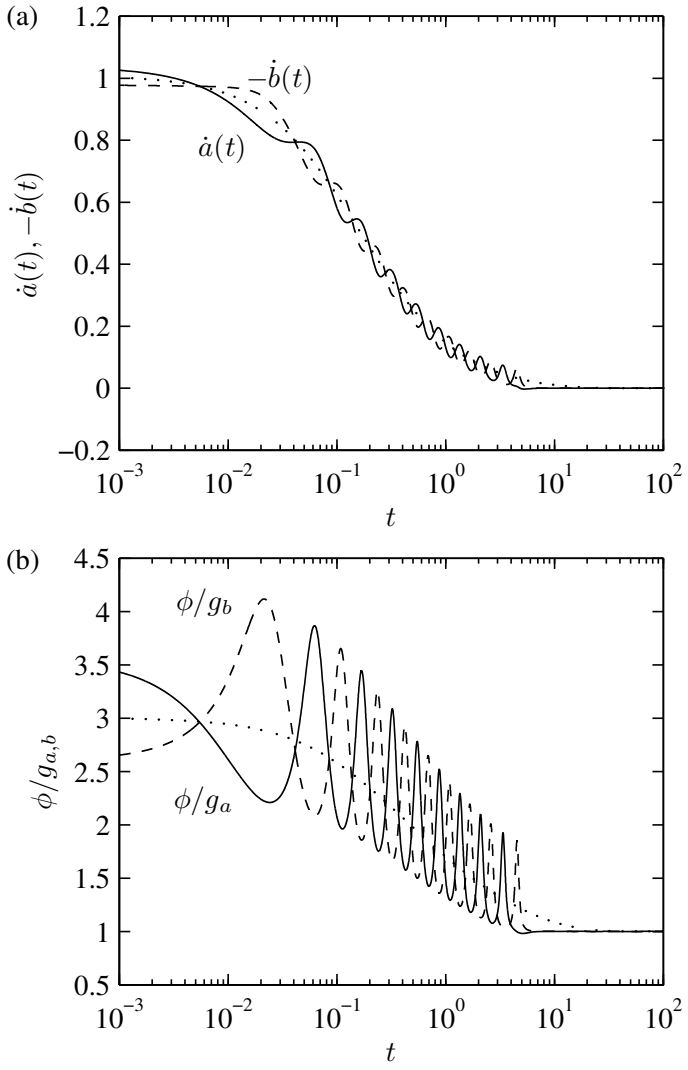

Figure 2.9.: Spreading on a substrate $g(x)$=1+0.3 sin 100x. (a) Time evolution of velocity of contact lines showing stick-slip type behaviour. (b) Evolution of the ratio of contact angles $\phi/g_{a,b}$.

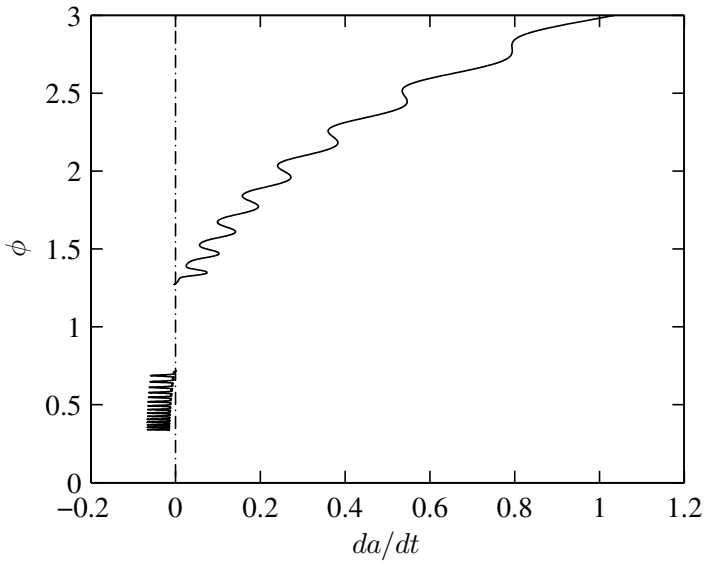

Figure 2.10.: Plot of apparent contact angle as a function of the velocity of a moving contact point for the substrate $g(x)$=1+0.3 sin 100x.

2.4.2. Phase-plane analysis

Capturing the spreading dynamics of the full nonlinear PDE with a set of two coupled ODEs also allows us to investigate the dynamics on the phase plane. By doing so, we aim to extract generic dynamic features, that would otherwise have been difficult to identify, by e.g. integrating at random the governing equations for different initial conditions. Figure 2.11(a) depicts the $a - b$ phase plane of equations (2.60a)–(2.60b) together with its direction field, for the substrate $g(x) = 1 + 0.8 \sin 4x$. We observe three types of equilibria, namely stable and unstable nodes and saddle points. Due to the assumed periodicity in the chemical heterogeneities, the equilibria also exhibit a periodic structure. Taking into account this structure, we can identify in figure 2.11(a) two equilibria for which there is wetting enhancement (points q_1 and q_2), and one for which there is wetting inhibition (point q_3). It is important to emphasise that assessments on wetting are made with respect to the homogeneous substrate, for which we defined the reference angle and $g(x) = 1$. Consequently, when we have $\phi > 1$ ($\phi < 1$) at equilibrium, we refer to these equilibria as wetting inhibiting (enhancing). Thiele et al. (2003) considered dewetting of thin films on chemically heterogeneous substrates using a space-dependent disjoining pressure formalism, and obtained bifurcation diagrams for the pinning and coarsening modes. The pinning modes correspond to droplets getting stuck at the heterogeneities whereas the coarsening modes correspond to formation of a large drop either by mass exchange be-

tween individual droplets through the precursor film or by droplet collisions. The branch corresponding to the pinning mode in their bifurcation diagram closely corresponds to the stable fixed points computed in our analysis.

Naturally, these equilibria must correspond to the stationary points of the total interfacial energy of the system, which in dimensional form is given by

$$\mathcal{E} = \int_b^a \left[\sigma \sqrt{1 + (\partial_x h)^2} + \sigma_{ls}(x) - \sigma_{sg}(x) \right] dx, \tag{2.63}$$

where, $\sigma_{ls}(x)$ and $\sigma_{sg}(x)$ are the spatially-varying surface tensions of liquid-solid and solid-gas interfaces respectively. By making use of the expression for the local contact angle predicted by Young's equation, $\sigma \cos\alpha(x) = \sigma_{sg}(x) - \sigma_{ls}(x)$, the long-wave form of $\mathcal{E}$, E, becomes

$$E = \int_b^a \left[(\partial_x h_0)^2 + g^2(x) \right] dx, \tag{2.64}$$

in nondimensional units, where $h_0(x)$ is the leading-order outer solution, (2.39).

For a given $g(x)$, E is a function of the position of contact points of the droplet, a and b. As an example, we show in figure 2.11(b) a plot of the interfacial energy, $E(a, b)$, corresponding to $g(x) = 1 + 0.8 \sin 4x$, together with some representative contours projected on the $E = 0$ plane. The plot, as well as our calculation, shows that, indeed, the stationary points of E correspond to the fixed points of equations (2.60a)–(2.60b) shown on the a-b phase plane of figure 2.11(a). It is clear, however that energy considerations alone cannot predict the dynamic droplet behaviour, which is highly dependent on the initial conditions. On the contrary, a phase plane analysis facilitates such assessments and the extraction of generic dynamic features.

In order to investigate whether other types of equilibria can exist apart from the ones observed in figure 2.11(a) (e.g. spiral fixed points or centers), we need to consider a linearisation of the system (2.60a)–(2.60b) about its equilibria. From equations (2.60a)–(2.60b) we find

$$a_\infty = b_\infty + 2\sqrt{3}/\sqrt{\phi_\infty}, \tag{2.65}$$

where a_∞ and b_∞ correspond to the equilibrium positions of the contact lines and ϕ_∞ is the equilibrium contact angle, which satisfies $\phi_\infty = g(a_\infty) = g(b_\infty)$. For chemically homogeneous substrates, equation (2.65) predicts a continuum of stable equilibria, shown as dotted lines in the phase-plane plot (figure 2.11(a)). Naturally, these equilibria are translationally invariant, but this invariance is broken with the introduction of a chemical structure, for which we can have at most countably infinite equilibria.

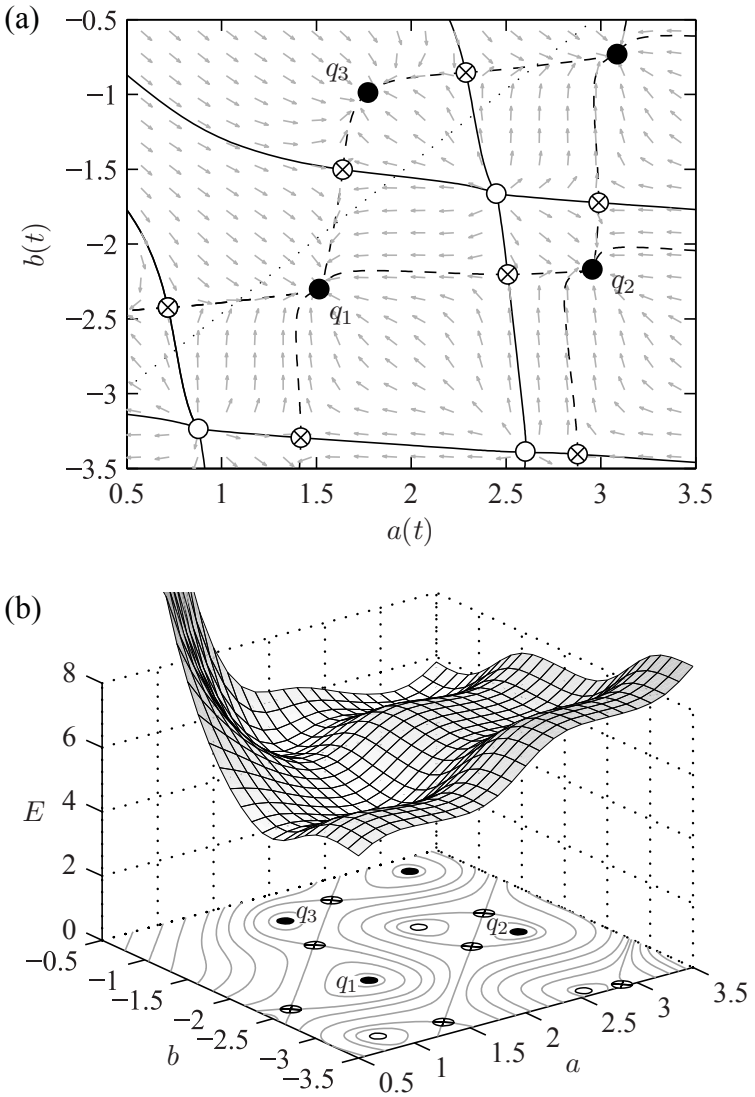

Figure 2.11.: (a) The a-b phase plane for $g(x) = 1 + 0.8 \sin 4x$. Solid and open circles represent the stable and unstable nodes, respectively, and the crossed circles represent the saddle points. Solid and dashed lines refer to the stable and unstable manifolds for the saddle nodes, respectively, whereas the dotted line shows the line of equilibria when $g(x) = 1$, (b) Plot of interfacial energy as a function of position of the contact points of the droplet for $g(x) = 1+0.8 \sin 4x$, along with some representative contours projected on the $E = 0$ plane (gray curves). The stationary points of E correspond to the fixed points of the phase plane in (a).

Next, consider the linearised system (2.60a)–(2.60b) about a fixed point to obtain

$$\begin{pmatrix} \dot{a} \\ \dot{b} \end{pmatrix} = \mathbf{J} \begin{pmatrix} a - a_\infty \\ b - b_\infty \end{pmatrix}, \tag{2.66}$$

where $\mathbf{J}$ corresponds to the Jacobian matrix evaluated at the fixed point (a_∞, b_∞). In order to have either spiral fixed points or centers, the Jacobian matrix must have complex eigenvalues. For this to happen, the discriminant of the characteristic polynomial of $\mathbf{J}$, D, must be negative. After some algebra, D evaluated at (a_∞, b_∞) is written as

$$D = \frac{\phi_\infty^4}{3A^2(A-2)^2} \left\{ 3A(A-2)\left(g'(a_\infty) + g'(b_\infty)\right)^2 + \left[2\phi_\infty^{3/2} A + \sqrt{3}\left(g'(a_\infty) - g'(b_\infty)\right) \right]^2 \right\},$$

where $A = \ln\left(2\sqrt{3\phi_\infty}/\lambda\right)$. Since the second term in the curly brackets is always positive, it is clear that the only way for D to become negative, is that $0 < A < 2$. This, however, can only occur for unrealistically large λ, in a regime where our matched asymptotics are expected to fail, as we have already pointed out in section 2.3.3. Consequently, at least for realistically small λ, no matter how $g(x)$ is chosen, it is impossible to excite any type of oscillatory behaviour. But for the relatively simpler case of a fixed point that is symmetric about the vertical axis, the Jacobian matrix $\mathbf{J}$ is also symmetric permitting only real eigenvalues, thus ruling out any oscillations in the droplet motion. Exploratory numerical experiments with the full PDE (2.35) suggest that this behaviour persists for larger λ as well.

Localised defects

Chemical heterogeneities may be utilised as a means to control droplet behaviour, by e.g. trapping the droplet between two localised defects. For the sake of illustration, consider a chemical profile of the form

$$g(x) = 1 + \epsilon\left[\operatorname{sech} 20(x + s/2) + \operatorname{sech} 20(x - s/2)\right],$$

which consists of two sufficiently isolated 'bumps' separated by a distance s. Here we take $s \geq 1$ so that the effects of one bump do not affect the other and $g(\pm s/2) \approx 1 + \epsilon$. We are interested in determining under what conditions the localised defects are able to trap a droplet that is initially located somewhere between them. In a more general setting, one could have allowed for different amplitudes in the two bumps, but this simpler problem allows us to capture the essential qualitative features as we change the 'strength' of the

isolated chemical defects, ϵ. The case of a single defect appears to be less interesting, as the velocities towards equilibrium are exponentially small; for a profile with a chemical 'bump' the droplet moves towards infinity, whereas for a chemical 'dimple' the droplet has a single stable equilibrium centered about the defect. The effects of a single defect on a far away droplet are extremely small and the droplet motion is virtually unaffected by it.

For our analysis we fix $s = 3$. Instead of considering the typical $a - b$ phase plane, we consider the $\ell - d$ phase plane, where ℓ is defined as the location of the droplet midpoint along the $x-$axis and d is the droplet 'radius':

$$\ell = (a + b)/2 \quad \text{and} \quad d = (a - b)/2.$$

This transformation is introduced to facilitate the visualisation of the different regimes we observe as ϵ varies. For sufficiently small ϵ, there are no stable fixed points, and the droplet eventually escapes from the defects. For initial conditions that are initially located symmetrically about the origin, i.e. when $\ell(0) = 0$, the droplet eventually attains an equilibrium radius that roughly corresponds to the equilibrium radius on the reference substrate, i.e. $d(\infty) \approx \sqrt{3} > 3/2$. In figure 2.12a we show a snapshot of the phase plane when $\epsilon = 0.2$, which illustrates this behaviour.

The absence of stable equilibria persists until we reach a critical ϵ, ϵ_c, beyond which a stable node appears, which lies symmetrically about $\ell = 0$. When $s = 3$, we readily observe that $\epsilon_c \approx 1/3$. In figure 2.12b, we show a snapshot of the phase plane for $\epsilon = 0.4 > \epsilon_c$, where we clearly see the newly emerged equilibria. To get a measure of the admissible initial conditions that may be used to trap the droplet between the chemical defects, we record the locations of the basin boundaries when $d(0) = 1$, which also allows us to determine the width of the basin of attraction, $\Delta\ell$ (see figure 2.12b). As ϵ is increased further, the basin of attraction of the fixed point enlarges, which in turn implies that given $d(0) = 1$, the range of $\ell(0)$ that eventually traps the droplet becomes larger, too. This is conveniently depicted on the regime diagram of figure 2.12c, where we plot $\ell(0)$ as a function of ϵ, with the shaded region corresponding to initial conditions for trapped droplets. This regime diagram is to be taken as an estimate of the actual diagram for the full PDE, since as we have noted earlier, in the vicinity of the boundaries of the basins of attraction our theory may potentially fail. It should also be noted that the actual 'basin of attraction' of the full PDE is infinite-dimensional, but nevertheless the information we can infer from figure 2.12c is sufficient to describe the trapping of a droplet between two defects, at least in qualitative terms.

At the critical ϵ, one eigenvalue of the Jacobian of the linearised system vanishes. At

this fixed point, the contact points are located at the maxima of $g(x)$, $x \approx \pm s/2$. Using equation (2.65), we find the radius at equilibrium, $d_\infty = \sqrt{3/(1+\epsilon_c)}$, from which we approximately deduce that

$$\epsilon_c \approx \frac{12}{s^2} - 1 \tag{2.67}$$

with exponentially small corrections. As a consequence, for $s < 2\sqrt{3}$ and when $\epsilon > \epsilon_c > 0$ a stable node appears that can potentially trap a droplet with advancing contact points, whereas for $s > 2\sqrt{3}$ and when $\epsilon < \epsilon_c < 0$, the stable node can potentially trap a droplet with receding contact points. This result is consistent with the observation by Thiele and Knobloch, where the less hydrophilic regions can trap advancing contact points and the more hydrophilic ones can trap receding contact points (Thiele and Knobloch, 2006a).

Patterned substrates

Chemically patterned substrates are specially treated substrates that composed of periodically alternating regions of different wettability. As in the preceding section, we employ a phase-plane analysis to extract qualitative features of the hysteresis-like effect induced by the varying substrate chemistry. We chose to model such substrates using a heterogeneity function of the form

$$g(x) = 1 + \varepsilon \tanh(m \cos kx), \tag{2.68}$$

which consists of a periodic array of plateau regions that have different wettability characteristics (see figure 2.13). Here ε is a measure of the wettability contrast between the two regions and k is the wavenumber of the profile. The parameter m controls how abruptly the transition between the two regions occurs; as m increases, $g(x)$ approaches a square waveform and as it decreases, it approaches a pure harmonic. We have fixed $m = 3$ so that we have relatively sharper transitions than having a pure harmonic and, at the same time, the phase-plane snapshots are sufficiently smooth for the clarity of presentation. Since our principal aim is to assess the chemically induced hysteresis, we consider the phase plane for a different set of variables, the apparent contact angle, ϕ, and the displacement of the droplet midpoint, ℓ.

We first take a substrate with $\varepsilon = 0.05$ and $k = 20$, a snapshot of which is shown in figure 2.13(a). Accounting for the substrate periodicity, we only observe three distinct equilibria: one saddle point and two stable nodes lying above and below $\phi = 1$, the reference contact angle (see figure 2.14(a)). More importantly, we observe that these stable equilibria are readily accessible for both initially advancing and initially receding contact points. For example, when we have $\ell(0) = 0$ and $\phi(0) = 3$ at the onset, the equilibrium attained at

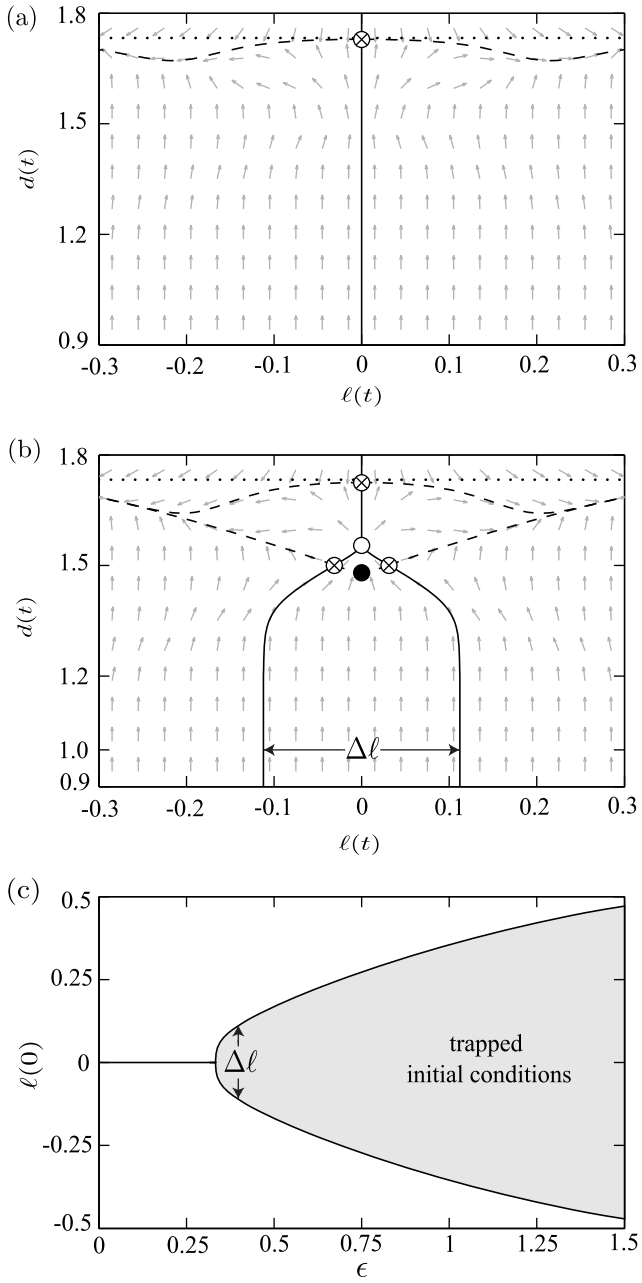

Figure 2.12.: (a),(b): The $\ell - d$ phase plane for the localised substrate $g(x)$=1.0 + $\epsilon\,[\mathrm{sech}\,20(x+1.5) + \mathrm{sech}\,20(x-1.5)]$ for (a) $\epsilon = 0.2$ and (b) $\epsilon = 0.4$. For the different lines and symbols refer to figure 2.11. (c) Regime diagram showing the initial droplet locations for which we have trapped contact points as a function of ϵ.

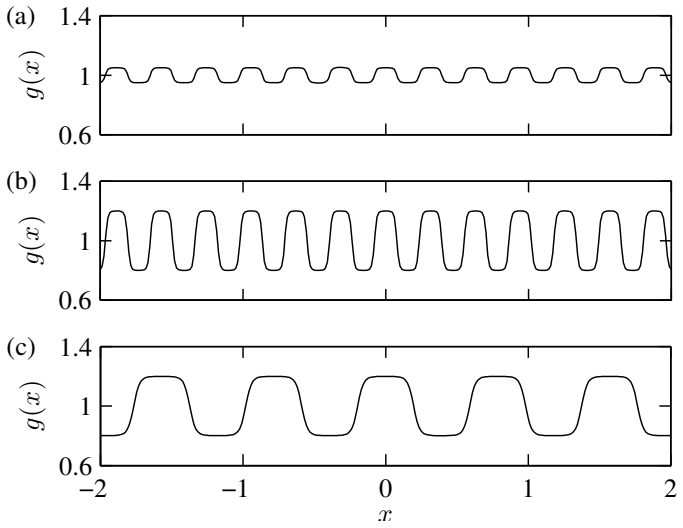

Figure 2.13.: Plots of the heterogeneity function $g(x) = 1.0 + \varepsilon \tanh(3 \cos kx)$. (a) $\varepsilon = 0.05, k = 20$, (b) $\varepsilon = 0.2, k = 20$ and (c) $\varepsilon = 0.2, k = 8$.

the end is wetting enhancing, whereas the equilibrium corresponding to $\ell(0) = -0.2$ and $\phi(0) = 3$ is wetting inhibiting. Nevertheless, the difference between the two equilibrium angles is small because the wettability contrast is fairly low.

As the wettability contrast increases, e.g. for $\varepsilon = 0.2$ and $k = 20$ (see figure 2.13(b)), the phase plane becomes richer due to emergence of new stable and unstable states. In this particular example, we now have 8 distinct equilibria, only 3 of which correspond to stable states (see nodes p_1, p_2 and p_3 in figure 2.14(b)). Since in a typical spreading experiment we initially have that $\phi(0) > 1 + \varepsilon$, we readily see that the only equilibrium that is accessible to advancing contact points is p_1. On the other hand, initially receding contact points, for which $\phi(0) < 1 - \varepsilon$, have access to the stable nodes p_2 and p_3 only. Given that the notion of wetting enhancement and inhibition is introduced with respect to advancing contact points, we may infer from the phase-plane plot of figure 2.14(b) that the substrate is wetting inhibiting with respect to the reference angle. However, it is important to emphasise that we now have two possible values for contact angle hysteresis between advancing and receding contact points, with the difference in the contact angle between the fixed points p_1 and p_3 being more appreciable compared to that of points p_1 and p_2. As generally expected, a further increase in the wettability contrast would amplify the observed hysteresis effect. On the other hand, the wettability contrast is not the only factor that influences wetting, but also the wavelength/wavenumber of the chemical heterogeneities. For example, if we keep the wettability contrast at $\varepsilon = 0.2$ and,

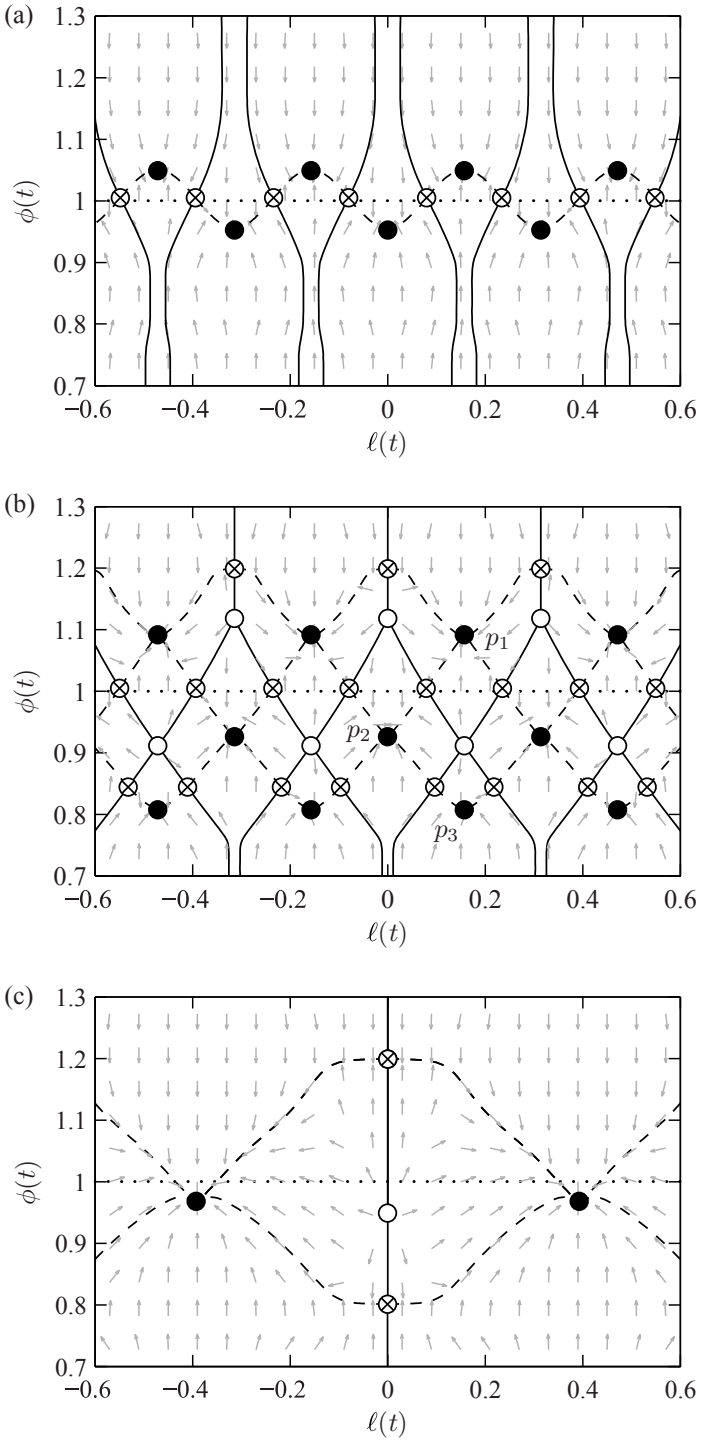

Figure 2.14.: The ℓ-ϕ phase plane for $g(x) = 1.0 + \varepsilon \tanh(3 \cos kx)$. (a) $\varepsilon = 0.05$, $k = 20$, (b) $\varepsilon = 0.2$, $k = 20$ and (c) $\varepsilon = 0.2$, $k = 8$. For the different lines and symbols refer to figure 2.11.

at the same time, reduce the wavenumber to $k = 8$ (see figure 2.13(c)), we now have a single stable configuration, which enhances wetting relative to the reference angle, $\phi = 1$ (see figure 2.14(c)).

To further investigate the effect of k, we consider the droplet equilibria for a wetting profile of the form prescribed by equation (2.68), which must satisfy $\cos(ka_\infty) = \cos(kb_\infty)$. From this relation, we can easily extract two different possibilities, namely $\ell_\infty = \pi n/k$ and $\phi_\infty = 3k^2/(n^2\pi^2)$, where n is an integer. Hence, the distinct droplet equilibria can either be located at $\ell_\infty = 0, \ell_\infty = \pi/k$ or the corresponding ℓ_∞ for which

$$\phi_\infty = 3k^2/(n^2\pi^2). \tag{2.69}$$

For equation (2.69), k must lie between $n\pi\sqrt{(1-\varepsilon)/3}$ and $n\pi\sqrt{(1+\varepsilon)/3}$ so that $1-\varepsilon < \phi_\infty < 1+\varepsilon$. To get a better picture for the variation of ϕ_∞ and its stability as k varies, numerical continuation techniques were used to trace the bifurcation curves of all droplet equilibria when $\ell_\infty = 0$ and $\ell_\infty = \pi/k$. The results of this calculation are depicted in figure 2.15, where ϕ_∞ is plotted as a function of k. They reveal intricate bifurcation events during which new equilibria appear or change stability characteristics due to coalescence with nearby equilibria. From such a plot one can identify all possible values of ϕ_∞, as for example in figure 2.15(b) where we clearly mark the stable equilibria corresponding to $k = 20$ (see also figure 2.14(b)).

From the above discussion, we may conclude that making quantitative statements as to how the contact angle is affected by heterogeneities in this geometry is a formidable task, apart from the observation that as the wavenumber increases, it is more likely for the equilibrium contact angle for a spreading droplet to be close to the maximum, $\phi_\infty = 1+\varepsilon$. To demonstrate the inability of equation (2.1) to describe the configurations we just described, we consider a substrate composed of two different materials with equilibrium contact angles, $1+\varepsilon$ and $1-\varepsilon$. These angles correspond roughly to the maximum and minimum microscopic contact angles for $g(x)$ in equation (2.68). Assuming equal area fractions, equation (2.1) becomes

$$\phi_C = \sqrt{1+\varepsilon^2}, \tag{2.70}$$

which, in the limit $\varepsilon \ll 1$, predicts wetting inhibition with hysteresis of $\mathcal{O}(\varepsilon^2)$ with respect to the reference angle. Clearly, equation (2.70) is independent of k, and as a result completely fails to capture any of the observations that were made above. Thus, it is not surprising that none of the test cases presented in figure 2.14 agrees with the prediction

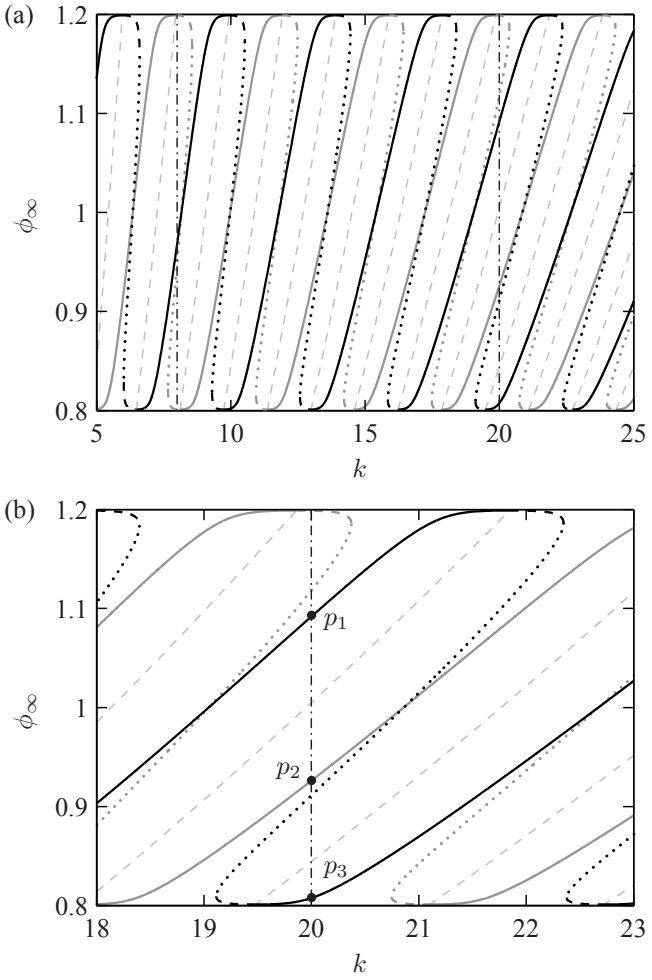

Figure 2.15.: (a) Evolution of equilibrium contact angles along with their stability, ϕ_∞, as k varies for $g(x) = 1+0.2\tanh(3\cos kx)$. Solid lines correspond to stable nodes, dashed lines to saddle points and the dotted lines to unstable nodes. The dashed-dotted line demarcates the cases when $k = 8$ and $k = 20$, whose phase planes appear in figures 2.14(b) and 2.14(c), respectively. The gray dashed curves which are nearly diagonal and linear correspond to the curves of (2.69) for different n. The black and gray curves correspond to the bifurcation curves for the equilibria located at $\ell_\infty = \pi/k$ and $\ell_\infty = 0$, respectively. As k increases, these curves become sheared towards the right, thus allowing for more equilibria for any given k. (b) Detail of (a) near $k = 20$ marking the equilibria that correspond to those exhibited in figure 2.14(b).

of equation (2.70). Even when we take $\varepsilon = 0.2$ and $k = 20$ (figure 2.14(b)) for which there is indeed wetting inhibition, the observed effect is $\mathcal{O}(\varepsilon)$, which is higher compared to the prediction of equation (2.70). Such significant deviations could be due to the anisotropy of the chemical features (Swain and Lipowsky, 1998).

2.5. Conclusion

We have considered the surface-tension-dominated motion of a partially wetting droplet on a chemically heterogeneous substrate. We utilised a single evolution equation for the droplet thickness obtained from a long-wave expansion of the Navier-Stokes equations. The stress singularity at the contact line was alleviated with the Navier slip condition, wherein the slip length was taken to be constant along the heterogeneous substrate due to its generally weak influence on the dynamics. We thus introduced the chemical heterogeneities by assuming spatial variations in the microscopic contact angle, which naturally enter the problem as boundary conditions. In the limit of small capillary numbers, the droplet motion can be treated quasistatically, with the time dependence entering the problem through the contact line locations. These modeling assumptions allowed us to analyse the dynamics using singular perturbation theory, by considering separately the free surface in the vicinity of the contact lines and the fluid bulk. By asymptotically matching the solutions in the contact line regions and bulk, we obtained a set of coupled ODEs for the velocity of the moving contact points.

The solutions to the set of ODEs obtained from matching was verified by direct comparisons with the governing PDE. In general, there is excellent agreement between the two. However, we found that it is possible for the two solutions to exhibit discordant evolution characteristics whenever the initial location of the two contact points of the droplet is sufficiently close to saddle point manifolds. These cases are commonly manifested as evolutions to different stable equilibria. The existence of multiple equilibria suggested that there can exist a hysteresis-like effect induced by the chemical heterogeneities, which was demonstrated by our simulations. This subsequently prompted our investigation of the phase plane of the two contact points, which facilitated the extraction of more general spreading characteristics. In particular, we investigated the effect of localised defects and found that a droplet can be trapped between them, depending on the initial location of the contact points and provided that the strength of the heterogeneities exceed some threshold. Finally, we have considered the effects of substrates composed of periodic regions that have different wetting characteristics and we demonstrated that the Cassie relation cannot explain the observed behaviours.

3. Liquid film sheared by a co-flowing turbulent gas

In this chapter, the dynamics of a thin liquid film flowing along an inclined plane in the presence of a co-current turbulent gas is presented. The majority of this chapter is based on Vellingiri et al. (2013), which was co-authored with Dmitri Tseluiko, Nikos Savva and Serafim Kalliadasis. My specific contribution in this work is to extend the analysis of Tseluiko and Kalliadasis (2011) performed for the countercurrent case, to the co-current one. More specifically, I have re-derived the weighted integral-boundary-layer (WIBL) model for the liquid problem to account for small changes necessary as compared to the work of Tseluiko and Kalliadasis (2011), performed a linear stability analysis of the flat film solution, and developed a pseudo-arclength continuation code to compute solitary waves and periodic travelling waves. The results of numerical continuation are compared with time-dependent computations of the WIBL model.

3.1. Introduction

Gas-liquid flows are ubiquitous in nature, such as the shearing of the sea-and lake-water by the air flowing over it. They are also central in a wide spectrum of engineering applications. For instance, in chemical engineering, gas-liquid flows are commonly observed in the transport of hydrocarbons through long distance pipelines, absorption and distillation processes, and in a wide spectrum of processes and devices. The associated rate of heat and mass transport is significantly influenced by the hydrodynamic and physico-chemical phenomena occurring on the interfaces, hence the study of interfacial effects becomes crucial for practical applications. An accurate description of the gas-liquid interface, that in turn depends on the liquid and gas flow structure, is also essential from the fundamental point of view to e.g. understand the various transitions occurring in the wave formation process associated with the destabilisation of the interface.

The flow of a thin liquid film on an inclined plate has been the subject of many studies for a long time since the pioneering experiments of Kapitza (1965). This seemingly

simple physical system can exhibit a rich dynamical behaviour starting from a laminar initial film, a sequence of wave families on the surface of the film, such as periodic traveling waves and solitary waves, and eventually spatiotemporal chaos through a series of bifurcations between the different wave families. For small to moderate values of the Reynolds number, the free surface is essentially two-dimensional, comprising of solitary waves which are formed as a result of the primary wave field undergoing a secondary instability. These solitary waves have been observed in many experimental (Liu and Gollub, 1994; Vlachogiannis and Bontozoglou, 2001) and theoretical studies (Chang et al., 1995; Malamataris and Balakotaiah, 2008). Extensive reviews of falling liquid film studies can be found in the monographs by Alekseenko et al. (1994), Chang and Demekhin (2002) and Kalliadasis et al. (2012).

One of the earliest works on co-current gas-liquid film flows was that of Hanratty and Engen (1957), where the interaction between a co-flowing turbulent air stream and a thin water film was investigated experimentally. These authors reported the transition from a smooth surface to two-dimensional waves, and further to "pebbled" surfaces. Craik (1966) studied experimentally thin water films of thickness 0.13-1.6 mm in a horizontal rectangular channel, and reported the presence of fast and slow waves, that traveled faster and slower than the interface, respectively. Cohen and Hanratty (1965), through a combination of theory and experiments, analysed a co-flowing glycerine-water solution with air in a horizontal channel. They had made use of the model of Miles (1957) and Benjamin (1959) to calculate the shear stress and pressure variations from their experimental data, and reported that the interfacial waves tend to decay, when the rate of energy transfer from the gas to the liquid is smaller than the viscous dissipation taking place within the liquid. In the co-current setting, it is observed that small droplets from the liquid film start to enter into the gas stream for sufficiently large values of liquid and gas flow rates. This phenomena is usually called entrainment or atomisation. Woodmansee and Hanratty (1969) attempted to connect the droplet entrainment from a liquid film in a horizontal co-current setting with the appearance of roll waves, which is typically marked by a sudden increase in the thickness of the liquid layer. Moreover, according to these authors, it is the imbalance in the pressure variations in the gas phase flowing over the wavelets, and the stabilising effect of gravity and surface tension that leads to the entrainment of droplets from the liquid film.

Lioumbas et al. (2005) investigated the stratified co-current gas-liquid film flow in an inclined channel by experiments. The experiments were conducted at high liquid Reynolds numbers and for small inclination angles. They observed that for a given gas flow rate, small amplitude waves that exist at relatively low liquid Reynolds numbers transform to

solitary waves as the Reynolds number is increased beyond a critical value. However, for large gas and liquid velocities, roll waves having a large amplitude and moving at high speed, start to appear. In their subsequent studies, Lioumbas et al. (2006, 2009) analysed the influence of surfactants on the wave characteristics of both the upflow and downflow configurations in inclined channels. In a recent experimental study, Alekseenko et al. (2009) investigated both the entrainment and no-entrainment regimes of gas-liquid annular flows, and attempted to link the occurrence of entrainment phenomena, with the disappearance of ripples that were previously formed on the backward slope of disturbance waves.

Theoretical studies of co-current gas-liquid film flows are limited. Jurman and McCready (1989) investigated theoretically and experimentally waves on thin liquid films sheared by a turbulent gas in a horizontal setting. In their analysis on glycerine-water solution system, they reported the existence of solitary waves that travel faster than the periodic waves, when the gas Reynolds number is sufficiently large till a critical liquid Reynolds number is reached. They supplemented their experimental analysis by deriving a weakly nonlinear model using boundary-layer-type approximations, and examined the influence of dynamic and kinematic processes on the wave behaviour. In their predominantly experimental study on a co-current gas sheared liquid flow problem in a horizontal setting, Peng et al. (1991) looked at the wave field both for low liquid Reynolds numbers, where solitary waves exist, and high Reynolds numbers, where solitary waves are absent. They conjectured that solitary waves originate from waves that have sufficiently large amplitude to substrate depth ratios, through a secondary transition. More recently, Frank (2006) demonstrated numerically by using the method of particles, the existence of solitary waves in a shear driven thin film flow in a horizontal channel in the presence of laminar gas flow.

The present study builds on the methodology developed by Tseluiko and Kalliadasis (2011) to analyse flooding (which corresponds to the appearance of large amplitude standing waves) in a countercurrent gas-liquid film flow. We concentrate here on the influence of gas shear on the structure and speed of solitary waves with a gas co-flowing over a thin liquid film in a vertical channel. As part of the analysis presented here parallels the work of Tseluiko and Kalliadasis (2011), when necessary the reader will be referred to this study for further details. For the co-current problem considered here, we solve the gas and liquid problems separately by making appropriate assumptions as in the study of Tseluiko and Kalliadasis (2011).

The gas problem in particular, is analyzed with an improved version of the quasi-laminar approach of Miles (1957) and Benjamin (1959), which is also used by Demekhin (1981) and Trifonov (2010) but on a Cartesian coordinate system. Like in Tseluiko and Kalli-

adasis (2011), we work on curvilinear boundary layer coordinates, and find perturbations to pressure and tangential stresses at the interface due to the turbulent gas flow, which are used as boundary conditions in the solution to the liquid flow problem. Instead of solving the full Navier-Stokes equation for the liquid problem, as done by Trifonov (2010), we develop a weighted integral-boundary-layer (WIBL) model, that has the advantage of being amenable to mathematical and numerical analysis for moderate Reynolds numbers. In particular, the weighted integral-boundary-layer model of Ruyer-Quil and Manneville (1998, 2000) for free-falling liquid films, obtained by combining the long-wave approximation with a polynomial expansion for the velocity field, with the integral-boundary-layer approximation and the method of weighted residuals, is known to describe nonlinear waves sufficiently far from criticality. This approach was further extended to falling film problems with additional complexities like thermocapillary Marangoni effects (Kalliadasis et al., 2003; Scheid et al., 2005a,b), solutocapillary Marangoni effects induced by chemical reactions (Trevelyan and Kalliadasis, 2004; Trevelyan et al., 2012) and insoluble surfactants (Pereira and Kalliadasis, 2008).

3.2. Problem setting

We consider a thin liquid film flowing down a smooth solid plate under the action of gravity as shown in figure 3.1. Let θ denote the inclination angle of the solid plate with respect to the horizontal, and ρ_ℓ and μ_ℓ the density and viscosity of the liquid, respectively. A gas of density ρ_g and viscosity μ_g, confined between the gas-liquid interface below and a planar solid wall at the top, flows in the downward direction (say, as a result of being pumped from the top). We take the width of the channel occupied by the gas to be much larger than the liquid film thickness, assuming also that the gas flows much faster than the liquid, hence the gas is taken to be turbulent whereas the liquid is taken to be laminar. Let the velocity and pressure in the liquid side be $\tilde{\mathbf{u}}$ and $\tilde{p}$, respectively, and the mean velocity and pressure in the gas side be $\widetilde{\mathbf{U}}$ and $\tilde{P}$, respectively. We assume that both the liquid and the mean gas flow are two-dimensional so that there are no variations in the transverse direction. Let $(\tilde{x}, \tilde{y})$ be a Cartesian coordinate system with the $\tilde{x}$-axis pointing downwards along the wall. Let the gas-liquid interface be located at $\tilde{y} = \tilde{h}(\tilde{x}, \tilde{t})$, and let the thickness of the liquid film when the interface is undisturbed be $\tilde{h}_0$. The distance between the undisturbed interface and the upper solid wall is taken to be $2\tilde{L}$.

Solving this coupled gas-liquid system is difficult, if not prohibitive. However, the problem becomes relatively simpler and analytical progress can be made by making use of the fact that the viscosity of the gas is much smaller than that of the liquid ($\mu_g \ll \mu_\ell$),

followed by a series of additional reasonable assumptions, namely that the velocity in the liquid layer is much smaller than the mean velocity in the gas layer and that the turbulent fluctuations in the gas flowing over the liquid film decay in the same way as those in the gas flowing over a rigid wall. Under these assumptions, the gas and liquid problems can be solved independently, as in Tseluiko and Kalliadasis (2011). In fact, the analysis in sections 3.3-3.4 follows closely to that in Tseluiko and Kalliadasis (2011) for the counter-current case, but for clarity and ease of presentation we reiterate the main steps here.

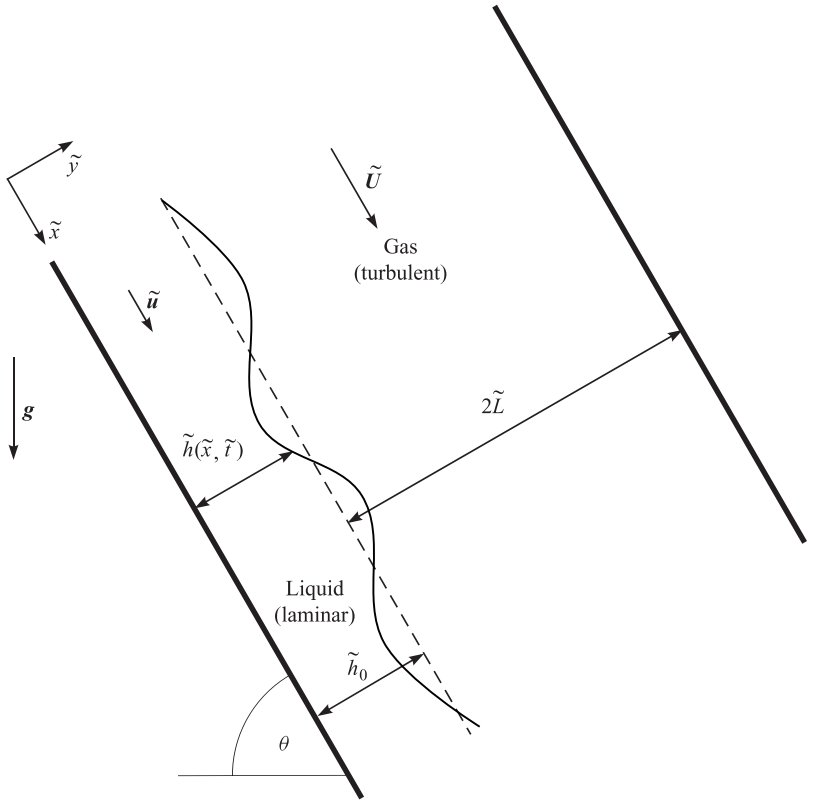

Figure 3.1.: Schematic of the co-current gas liquid flow problem in an inclined channel.

3.3. Gas problem

3.3.1. Governing equations

We model the turbulent nature of the gas flow by assuming the flow to be quasi-steady, and applying appropriate averaging. We then obtain the following incompressible Reynolds-

averaged Navier-Stokes (RANS) equation together with the equation for mass conservation (Schlichting, 2000):

$$\rho_g \widetilde{\mathbf{U}} \cdot \boldsymbol{\nabla} \widetilde{\mathbf{U}} = -\boldsymbol{\nabla} \widetilde{P} + \mu_g \boldsymbol{\nabla}^2 \widetilde{\mathbf{U}} + \boldsymbol{\nabla} \cdot \widetilde{\boldsymbol{\sigma}}, \qquad \boldsymbol{\nabla} \cdot \widetilde{\mathbf{U}} = 0, \tag{3.1}$$

where $\widetilde{\mathbf{U}} = (\widetilde{U}, \widetilde{V})$ and $\widetilde{P}$ are the mean velocity and pressure fields in the gas phase, respectively, $\boldsymbol{\nabla} = (\partial/\partial\tilde{x}, \partial/\partial\tilde{y})$, $\widetilde{\boldsymbol{\sigma}}$ is the Reynolds stress tensor coming from the contribution of turbulent fluctuations, whereas $\mu_g \boldsymbol{\nabla}^2 \widetilde{\mathbf{U}}$ originates from the viscous stress tensor.

The boundary conditions supplementing equation (3.1) are the no-slip and no-penetration conditions at the upper planar wall and the lower wavy wall that corresponds to the liquid-gas interface:

$$\widetilde{\mathbf{U}} = \mathbf{0} \quad \text{at} \quad \tilde{y} = \tilde{h}_0 + 2\tilde{L} \quad \text{and} \quad \tilde{y} = \tilde{h}_0 + \tilde{s}(\tilde{x}), \tag{3.2}$$

where $\tilde{s}(\tilde{x}) = \tilde{\epsilon} e^{\mathrm{i}\tilde{\alpha}\tilde{x}}$, and $\tilde{\epsilon}$ and $\tilde{\alpha}$ correspond to the amplitude and wavenumber of the undulating wall (the liquid-gas interface), respectively. We also note here that the real part of $\tilde{s}(\tilde{x})$ represents the actual physical wall.

3.3.2. Non-dimensionalisation

In order to make the equations dimensionless, we choose, respectively, the following velocity, length and pressure scales:

$$U_f^* = \sqrt{\frac{T_w}{\rho_g}}, \quad L_c = \frac{\mu_g}{\rho_g U_f^*}, \quad P_c = \rho_g U_f^{*2}, \tag{3.3}$$

where T_w is the shear stress at the lower wall when the wall is flat, and U_f^* is the friction velocity. Furthermore, we define the normal coordinate y to be $y = (\tilde{y} - \tilde{h}_0)/L_c$, such that $y = 0$ corresponds to the undisturbed wall.

The resulting equations and boundary conditions in non-dimensional form are given by

$$UU_x + VU_y = -P_x + U_{xx} + U_{yy} + \tau_{11x} + \tau_{12y}, \tag{3.4a}$$

$$UV_x + VV_y = -P_y + V_{xx} + V_{yy} + \tau_{21x} + \tau_{22y}, \tag{3.4b}$$

$$U_x + V_y = 0, \tag{3.4c}$$

$$U = V = 0 \quad \text{at} \quad y = s(x) \quad \text{and} \quad y = 2L, \tag{3.5}$$

where the components of the dimensionless Reynolds stress tensor is given by $\tau_{ij} = \overline{U_i' U_j'}$ with $(U_1', U_2') = (U', V')$ with the primes denoting fluctuations from the time-averaged

velocity field. The gas-liquid interface is prescribed in dimensionless form by $y = s(x) \equiv \epsilon e^{i\alpha x}$, where $\epsilon (= \tilde{\epsilon}/L_c) \ll 1$, and $\alpha = \tilde{\alpha}/L_c$. To proceed further, we look for a unidirectional velocity profile when the lower wall is assumed to be undisturbed. The turbulent stress are modeled by invoking the mixing-length theory, setting $\tau_{0\,11} = \tau_{0\,22} = 0$ and $\tau_{0\,12} = \tau_{0\,21} = \ell^2 |U_{0y}| U_{0y}$ (here subscripts 0 indicate the base solution for the flat interface), where ℓ is the mixing-length that corresponds to the distance over which the fluid element keeps its original characteristics. In the log-law (turbulent-core) region, the mixing-length is given by $\ell = \kappa y$. However, if the same specification has to be applied in the viscous sublayer, then the mixing-length (ℓ) has to be damped near the wall. Such a damping was introduced by Van Driest (1956), with the mixing-length equation given by $\ell = \kappa y \left[1 - e^{-y/A}\right]$, where $\kappa = 0.41$ is the von Kármán constant and $A = 25$ is the damping friction. Under these conditions, it was shown that

$$U_0 = \int_0^y \frac{2(L-z)/L}{1 + \sqrt{1 + 4\kappa^2 z^2 [1 - e^{-z/A}]^2 (L-z)/L}} dz. \tag{3.6}$$

The velocity profile U_0 for $L = 200$ is shown in figure 3.2. The gas flow has a layered

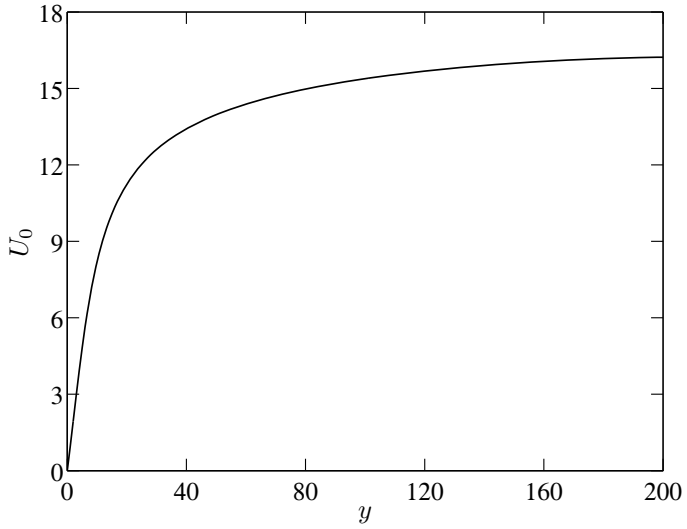

Figure 3.2.: Base-state velocity profile symmetric about $y = 200$.

structure. In the core layer, where $\ell \gg 1$, the turbulent momentum transfer dominates. Sufficiently close to the wall (about 20% of the height of the flow), the velocity profile is logarithmic (known as the universal law of the wall). In the thin wall layer, where $\ell \sim 1$, both molecular and turbulent momentum transport act. There is also a very thin viscous sublayer near the wall, where $\ell \ll 1$, in which turbulent momentum transport can be

neglected and the velocity profile is linear (Schlichting, 2000).

3.3.3. Flow over an undulated wall

This base-state solution obtained by considering the interface to be flat in the Cartesian system will be utilised in our subsequent treatment of the problem in the curvilinear coordinates. We recall that the lower wall of the channel is wavy, whereas the top wall is planar. The solution to the fluid flow problem in such a geometry would become relatively simpler, if we choose to work in a coordinate system that would naturally represent these changing boundaries. This calls for a treatment in the curvilinear coordinate system like the one followed by Benjamin (1959). The curvilinear coordinates ξ_1 and ξ_2 can be written in terms of the cartesian coordinates (x, y) as $\xi_1 = \xi_1(x, y)$ and $\xi_2 = \xi_2(x, y)$. As we move away from the lower wavy wall, we want the coordinate lines ξ_1 and ξ_2 to approach that of the Cartesian system. Benjamin (1959) introduced the following coordinates:

$$\xi_1 = x - \mathrm{i}\epsilon \mathrm{e}^{-\alpha y}\mathrm{e}^{\mathrm{i}\alpha x}, \tag{3.7a}$$

$$\xi_2 = y - \epsilon \mathrm{e}^{-\alpha y}\mathrm{e}^{\mathrm{i}\alpha x}. \tag{3.7b}$$

We could infer from equation (3.7) that $\xi_2 = 0$ represents the lower wavy wall to first order in ϵ. It is to be noted that the real parts of equations (3.7a)-(3.7b) represent meaningful coordinates, and complex number notations are used only for convenience in calculations.

We proceed by using a stream function formulation for the incompressible RANS equation. Let ψ denote the stream function. Making use of the fact that the wall amplitude is small and writing the expansions

$$\psi = \psi_0(\xi_2) + \epsilon\psi_1(\xi_2)\mathrm{e}^{\mathrm{i}\alpha\xi_1} + \cdots, \tag{3.8}$$

$$P = P_0 + \epsilon P_1(\xi_2)\mathrm{e}^{\mathrm{i}\alpha\xi_1} + \cdots, \tag{3.9}$$

$$\bar{\tau}_{ij} = \bar{\tau}_{0ij} + \epsilon\bar{\tau}_{1ij}(\xi_2)\mathrm{e}^{\mathrm{i}\alpha\xi_1} + \cdots, \tag{3.10}$$

where ψ_0, P_0 and $\bar{\tau}_{0ij}$ denote the stream function, the pressure and the turbulent Reynolds stresses corresponding to the base solution, we obtain the following equation for ψ_1:

$$\psi_1'''' - 2\alpha^2\psi_1'' + 4\alpha\mathrm{e}^{-\alpha\xi_2}\left(\psi_0'''' - \alpha\psi_0'''\right) = -\mathrm{i}\alpha\left[\psi_1\psi_0''' - \psi_0'\left(\psi_1'' - \alpha^2\psi_1 + 2\alpha\psi_0''\mathrm{e}^{-\alpha\xi_2}\right)\right] - \mathscr{R}_1 \tag{3.11}$$

where,

$$\mathscr{R}_1 = \mathrm{i}\alpha\bar{\tau}_{1_{11}}' - \mathrm{i}\alpha\bar{\tau}_{1_{22}}' + \alpha^2\bar{\tau}_{1_{12}} + \bar{\tau}_{1_{12}}'' + \mathrm{e}^{-\alpha\xi_2}\left[2\mathrm{i}\alpha^3\bar{\tau}_{0_{11}} - \mathrm{i}\alpha^2\bar{\tau}_{0_{11}}' - 2\mathrm{i}\alpha^3\bar{\tau}_{0_{22}} + \mathrm{i}\alpha^2\bar{\tau}_{0_{22}}' - 4\alpha^3\bar{\tau}_{0_{12}} + 2\alpha^2\bar{\tau}_{0_{12}}' + 2\alpha\bar{\tau}_{0_{12}}''\right]. \quad (3.12)$$

To solve equation (3.11), we make the assumption that the Reynolds stresses induced by the waviness of the interfacial wall and the normal stresses are zero (Thorsness et al., 1978), i.e., $\bar{\tau}_{1_{11}} = \bar{\tau}_{1_{12}} = \bar{\tau}_{1_{21}} = \bar{\tau}_{1_{22}} = 0$ and $\bar{\tau}_{0_{11}} = \bar{\tau}_{0_{22}} = 0$. This implies,

$$\psi_1'''' - 2\alpha^2\psi_1'' + 4\alpha\mathrm{e}^{-\alpha\xi_2}\left(\psi_0'''' - \alpha\psi_0'''\right) = -\mathrm{i}\alpha\left[\psi_1\psi_0''' - \psi_0'\left(\psi_1'' - \alpha^2\psi_1 + 2\alpha\psi_0''\mathrm{e}^{-\alpha\xi_2}\right)\right] + \mathrm{e}^{-\alpha\xi_2}\left[2\alpha\bar{\tau}_{0_{12}}'' + 2\alpha^2\bar{\tau}_{0_{12}}' - 4\alpha^3\bar{\tau}_{0_{12}}\right]. \quad (3.13)$$

The boundary conditions supplementing the above fourth-order differential equation are the no-slip and no-penetration conditions at the wall, given by

$$\psi_1 = 0, \quad \psi_1' = 0, \quad \text{at} \quad \xi_2 = 0. \quad (3.14)$$

Even when the gas-liquid interface is treated as a solid wall (for the gas problem) as per our assumptions, imposing no slip at the interface would lead to imposing a finite tangential velocity as the liquid is in motion. However, for a steadily propagating wave, rewriting the equations for the gas layer in a moving frame allows us to imposing a zero velocity at the interface. Given that as we move away from the wall the flow approaches the base flow for a sufficiently wide channel, we can impose the conditions

$$\psi_1 = 0, \quad \psi_1' = 0, \quad \text{at} \quad \xi_2 = L. \quad (3.15)$$

We note that ψ_0 and $\bar{\tau}_{0_{12}}$ come from the base-state solution. Once we know the stream function, we can compute the shear stress at the gas-liquid interface, τ_w, and the pressure at the interface, P_w:

$$\tau_w = 1 + \epsilon\tau_{w1}(\alpha)\mathrm{e}^{\mathrm{i}\alpha\xi_1} + \cdots, \quad (3.16)$$

$$P_w = P_0 + \epsilon P_{w1}(\alpha)\mathrm{e}^{\mathrm{i}\alpha\xi_1} + \cdots, \quad (3.17)$$

where

$$\tau_{w1}(\alpha) = \psi_1''(0) + 2\alpha, \tag{3.18}$$

$$P_{w1}(\alpha) = \frac{\mathrm{i}}{\alpha}\left[\frac{2\alpha}{L} + 2\alpha^2 - \psi_1'''(0)\right]. \tag{3.19}$$

It can be easily shown that there exists a relation between shear stresses and pressures for the co-current and counter-current flows. Indeed, let $\bar{\tau}_w$ and $\bar{P}_w$ denote the shear stress and the pressure for the counter-current flow over a wavy wall of small amplitude, i.e.

$$\bar{\tau}_w = -1 + \epsilon\bar{\tau}_{w1}(\alpha)\mathrm{e}^{\mathrm{i}\alpha\xi_1} + \cdots, \tag{3.20}$$

$$\bar{P}_w = P_0 + \epsilon\bar{P}_{w1}(\alpha)\mathrm{e}^{\mathrm{i}\alpha\xi_1} + \cdots. \tag{3.21}$$

Keeping in mind that actually real parts represent physical quantities, we must have

$$[P_w(\xi_1)]_R = [\bar{P}_w(-\xi_1)]_R, \tag{3.22}$$

$$[\tau_w(\xi_1)]_R = -[\bar{\tau}_w(-\xi_1)]_R, \tag{3.23}$$

which implies that

$$\bar{P}_{w1}(\alpha) = [P_{w1}(\alpha)]^*, \quad \bar{\tau}_{w1}(\alpha) = -[\tau_{w1}(\alpha)]^*, \tag{3.24}$$

where R in the subscript denotes real part of the complex quantity and '$*$' denotes complex conjugation. These relations allow us to map the counter-current problem, to the co-current one.

We also note also that for the counter-current case, Tseluiko and Kalliadasis (2011) compared their theoretical predictions for the shear stress and the pressure imposed by a turbulent gas flowing over a wavy wall with the experimental results of Zilker et al. (1977) and Thorsness et al. (1978) and found good agreement. Moreover, it was found that the analysis in curvilinear boundary layer coordinates gives significantly better agreement with experiments than the analysis in Cartesian coordinates.

As a next step, we consider the lower wall (corresponding to the interface) to be a periodic function with zero mean and period λ given by

$$s(x) = \sum_{\substack{n=-\infty \\ n\neq 0}}^{\infty} s_n \mathrm{e}^{\mathrm{i}\alpha_n x}, \tag{3.25}$$

where the wavenumber $\alpha_n = 2\pi n/\lambda$, and s_n are the Fourier coefficients. To obtain expressions for the shear stress and the pressure imposed on such a wall, we make the assumption that these quantities depend linearly on the interface shape. Therefore, the wall shear stress and pressure, are, respectively

$$\tau_w[s] = 1 + \sum_{\substack{n=-\infty \\ n\neq 0}}^{\infty} s_n \tau_{w1}(\alpha_n) \mathrm{e}^{\mathrm{i}\alpha_n x} \tag{3.26}$$

and

$$P_w[s] = P_0 + \sum_{\substack{n=-\infty \\ n\neq 0}}^{\infty} s_n P_{w1}(\alpha_n) \mathrm{e}^{\mathrm{i}\alpha_n x}. \tag{3.27}$$

Here, for a negative α_n, we define $\tau_{w1}(\alpha_n) = [\tau_{w1}(-\alpha_n)]^*$ and $P_{w1}(\alpha_n) = [P_{w1}(-\alpha_n)]^*$. For a given $s(x)$, by making use of equation (3.18), we can compute the shear stress τ_w and the pressure P_w acting on the wall.

3.4. Liquid problem

3.4.1. Governing equations

The governing equations for the liquid film are the Navier-Stokes and the continuity equations, which we non-dimensionalise using the following velocity, time, pressure and length scales:

$$u_c = \frac{\rho_\ell g \tilde{h}_0^2 \sin\theta}{2\mu_\ell}, \quad t_c = \frac{\tilde{h}_0}{u_c}, \quad p_c = \frac{\mu_\ell u_c}{\tilde{h}_0}, \quad \ell_c = \tilde{h}_0, \tag{3.28}$$

where the characteristic velocity, u_c, is the Nusselt free-surface speed for the case when there is no gas flow above the film. The governing equation take the form

$$Re\,(u_t + uu_x + vu_y) = -p_x + u_{xx} + u_{yy} + 2, \tag{3.29a}$$

$$Re\,(v_t + uv_x + vv_y) = -p_y + v_{xx} + v_{yy} - 2\cot\theta, \tag{3.29b}$$

$$u_x + v_y = 0, \tag{3.29c}$$

where Re is the Reynolds number defined as

$$Re = \frac{\rho_\ell u_c \tilde{h}_0}{\mu_\ell}. \tag{3.30}$$

At the wall, $y = 0$, no-slip and no-penetration conditions are satisfied: $u = v = 0$. The kinematic condition and the tangential and normal stress balance conditions at the interface, $y = h(x,t) = 1 + \sum_{\substack{n=-\infty \\ n\neq 0}}^{\infty} h_n(t) e^{\mathrm{i}\alpha_n x}$, require

$$h_t + u h_x = v, \quad \text{at} \quad y = h(x,t), \tag{3.31a}$$

$$-\frac{1}{1+h_x^2}\left[2(u_x - v_y)h_x - (u_y + v_x)(1-h_x^2)\right] = \hat{\tau}_w[h], \tag{3.31b}$$

$$p = \hat{P}_w[h] + \frac{2}{1+h_x^2}\left[u_x h_x^2 - (u_y + v_x)h_x + v_y\right] - \frac{Re\ We\ h_{xx}}{(1+h_x^2)^{3/2}}. \tag{3.31c}$$

In equation (3.31b) $\hat{\tau}_w[h]$ is the shear stress exerted by the gas on the interface given by

$$\hat{\tau}_w[h] = \frac{\tilde{h}_0}{\mu_l \tilde{u}_0}\tilde{\tau}_w[\tilde{h}] = \hat{\tau}_{w0} + \hat{\tau}_{w0}\nu\,\hat{\tau}_{w1}[h], \tag{3.32}$$

where

$$\hat{\tau}_{w0} = \frac{\tilde{h}_0 T_w \tau_{w0}}{\mu_l \tilde{u}_0}, \qquad \nu = \frac{\tilde{h}_0 \rho_g U_f^*}{\mu_g}, \qquad \hat{\tau}_{w1}[h] \equiv \sum_{\substack{n=-\infty \\ n\neq 0}}^{\infty} h_n \tau_{w1}(\alpha_n/\nu)\mathrm{e}^{\mathrm{i}\alpha_n x}. \tag{3.33}$$

We note that ν is the ratio of the length scales used to non-dimensionalise the liquid and the gas problems, respectively. In equation (3.31c) $\hat{P}_w[h]$ is the normal stress exerted by the gas on the interface that is given by

$$\widehat{P}_w[h] = \frac{h_0}{\mu_l \tilde{u}_0}\widetilde{P}_w[\tilde{h}] = \widehat{P}_0 + \hat{\tau}_{w0}\nu\widehat{P}_1[h], \tag{3.34}$$

with

$$\widehat{P}_0 = \hat{\tau}_{w0} P_0, \qquad \widehat{P}_1[h] \equiv \sum_{\substack{n=-\infty \\ n\neq 0}}^{\infty} h_n P_{w1}(\alpha_n/\nu)\mathrm{e}^{\mathrm{i}\alpha_n x}. \tag{3.35}$$

It is important to emphasise that the instantaneous interfacial shear stress, (3.32), and pressure, (3.34), are computed through equations (3.26) and (3.27), by setting $s_n = \nu h_n$. The dimensionless parameter *We* is the Weber number that signifies the ratio of surface tension forces to the inertial forces, and is defined as

$$We = \frac{\sigma}{\rho_\ell u_c^2 \sin\theta}. \tag{3.36}$$

Note that the Weber number, We, can further be expressed in terms of the Kapitza number, Ka, and the Reynolds number, Re, as follows

$$We = \frac{4Ka}{Re_0^{5/3}\sin^2\theta}, \tag{3.37}$$

where, $Ka = \sigma\rho_\ell^{1/3}/(g^{1/3}\mu_\ell^{4/3})$ depends on the properties of the liquid only, and $Re_0 = \rho_\ell^2 g\tilde{h}_0^3/\mu_\ell^2$ with $Re = (Re_0\sin\theta)/2$. For convenience we can write

$$\hat{\tau}_{w0} = \frac{2}{Re_0^{1/3}\sin\theta}\Theta\tau_{w0}, \qquad \nu = NRe_0^{1/3}\Theta^{1/2}, \tag{3.38}$$

where

$$\Theta = \frac{T_w}{\rho_l^{1/3}\mathrm{g}^{2/3}\mu_l^{2/3}}, \qquad N = \frac{\mu_l\rho_g^{1/2}}{\mu_g\rho_l^{1/2}}. \tag{3.39}$$

The parameter Θ controls the gas shear-stress strength, whilst the parameter N depends only on the densities and viscosities of the liquid and the gas.

3.4.2. Weighted integral boundary layer model

To develop a simplified model that captures the essential physics of the gas-liquid system considered here, we make use of the methodology developed by Ruyer-Quil and Manneville (1998, 2000) to model free-liquid films on an inclined plane. The starting point of this is the derivation of the first-order boundary layer approximation. As in many thin-film settings, the problem can be substantially simplified, however, by utilising the long-wave approximation, letting

$$\xi = x\epsilon; \quad \tau = t\epsilon; \quad v = w\epsilon, \tag{3.40}$$

where ϵ is the thin-film or long-wave parameter. Neglecting the higher-order inertia terms in the y-momentum equation, we have

$$p_y = -2\cot\theta + \mathcal{O}(\epsilon, \epsilon^2 Re). \tag{3.41}$$

Considering only the leading-order contribution from the surface tension and gas flow in the normal stress balance equation, we obtain the pressure distribution from equation (3.41), which when substituted into the streamwise momentum equation results in

$$\epsilon Re\left[u_\tau + uu_\xi + wu_y\right] = -\epsilon\left(2\cot\theta h_\xi - \epsilon^2 Re\ We\, h_{\xi\xi\xi}\right) + u_{yy} + 2, \tag{3.42}$$

where $We = \mathcal{O}(\epsilon^{-2})$, and terms of $\mathcal{O}(\epsilon^2)$ and $\mathcal{O}(\epsilon^3 Re)$ are neglected. Equation (3.42) is accompanied by the no-slip condition at the bottom wall and the kinematic condition at the free surface:

$$h_\tau + q_\xi = 0, \tag{3.43}$$

where $q = \int_0^h u\, dy$ is the local flow rate. Finally, we have the tangential stress balance

$$u_y = \hat{\tau}_{w0} + \epsilon\bar{\nu}\hat{\tau}_{w1}[h] \quad \text{at} \quad y = h(\xi, \tau). \tag{3.44}$$

Equations (3.42)-(3.44) are the first-order boundary-layer equations for the gas-liquid problem. The approach now is to project the velocity field onto the polynomial test function, which is a function of the similarity variable $\eta\,(= y/h)$, given by

$$u = \sum_{i=1}^{N} a_i(\xi, \tau)\eta^i. \tag{3.45}$$

Expressing the stream-wise flow rate q in terms of η, we get

$$q = \int_0^h \sum_{i=1}^{N} a_i(\xi, \tau)\frac{y^i}{h^i}\, dy = \sum_{i=1}^{N} \frac{a_i}{i+1}h, \tag{3.46}$$

which can further be written as

$$\frac{a_1}{2} + \frac{a_2}{3} = \frac{q}{h} - \sum_{i=3}^{N} \frac{a_i}{i+1}. \tag{3.47}$$

Further, we require that the chosen velocity field (3.45) has to satisfy the boundary conditions. Requiring that (3.45) satisfies the tangential stress condition (3.44) at the interface implies,

$$a_1 + a_2 = h\hat{\tau}_w[h] - \sum_{i=3}^{N} i a_i. \tag{3.48}$$

Solving equations (3.47)-(3.48) for a_1 and a_2, we get

$$a_1 = \frac{3q}{h} - \frac{1}{2}h\hat{\tau}_w[h] + \sum_{i=3}^{N}\left(\frac{i}{2} - \frac{3}{i+1}\right)a_i, \tag{3.49a}$$

$$a_2 = -\frac{3q}{2h} + \frac{3}{4}h\hat{\tau}_w[h] + \sum_{i=3}^{N}\left(\frac{3}{2(i+1)} - \frac{3i}{4}\right)a_i. \tag{3.49b}$$

Therefore, the x-component velocity u can be written as

$$u = \frac{3q}{h}\left(\eta - \frac{\eta^2}{2}\right) - \frac{1}{2}h\hat{\tau}_w[h]\left(\eta - \frac{3\eta^2}{2}\right) + \sum_{i=3}^{N}\left[\left(\frac{i}{2} - \frac{3}{i+1}\right)\eta + \left(\frac{3}{2(i+1)} - \frac{3i}{4}\right)\eta^2 + \eta^i\right]a_i, \quad (3.50)$$

which can further be written in a compact form as

$$u = u^{(0)} + u^{(1)} + \sum_{i=2}^{N-1} a_{i+1}\phi_i(\eta), \quad (3.51)$$

where,

$$u^{(0)} = \frac{3q}{h}\left(\eta - \frac{\eta^2}{2}\right), \quad (3.52a)$$

$$u^{(1)} = -\frac{1}{2}h\hat{\tau}_w[h]\left(\eta - \frac{3\eta^2}{2}\right), \quad (3.52b)$$

$$\phi_i(\eta) = \left(\frac{i+1}{2} - \frac{3}{i+2}\right)\eta + \frac{3}{4}\left(\frac{2}{i+2} - i - 1\right)\eta^2 + \eta^{i+1}. \quad (3.52c)$$

Equation (3.51) can also be expressed as

$$u = u^{(1)} + \sum_{i=1}^{N-1} b_i\phi_i(\eta), \quad (3.53)$$

where, $b_1 = 3q/h$, $\phi_1(\eta) = \eta - \eta^2/2$ and $b_i = a_{i+1}$, for $i = 2, \ldots, N-1$. Considering only the first two terms in the expansion, equation (3.53) implies

$$u = \frac{3q}{h}\left(\eta - \frac{\eta^2}{2}\right) - \frac{1}{2}h\hat{\tau}_w[h]\left(\eta - \frac{3\eta^2}{2}\right). \quad (3.54)$$

We obtain the residual $\mathscr{R}$ by substituting the assumed velocity field, $u = u^{(0)} + u_a^{(1)} + u_b^{(1)}$ in the x-momentum equation (3.29a)

$$\mathscr{R} = \epsilon\, Re\left[u_\tau^{(0)} + u_{a\,\tau}^{(1)} + (u^{(0)} + u_a^{(1)})(u_\xi^{(0)} + u_{a\,\xi}^{(1)}) + w^{(0)}(u_y^{(0)} + u_{a\,y}^{(1)})\right] + \epsilon\left(2\cot\theta h_\xi - \epsilon^2 Re\, We\, h_{\xi\xi\xi}\right) - u_{yy}^{(0)} - u_{a\,yy}^{(1)} - u_{b\,yy}^{(1)} - 2 + \mathcal{O}(\epsilon^2\, Re), \quad (3.55)$$

where,

$$u_a^{(1)} = -\frac{1}{2}\hat{\tau}_{w0} h \left(\eta - \frac{3}{2}\eta^2\right), \tag{3.56a}$$

$$u_b^{(1)} = -\frac{1}{2}\epsilon\bar{\nu}\hat{\tau}_{w0} h \hat{\tau}_{w1}[h] \left(\eta - \frac{3}{2}\eta^2\right), \tag{3.56b}$$

$$w = -\int_0^y \left(u_\xi^{(0)}(\xi, \bar{y}, \tau) + u_{a\xi}^{(1)}(\xi, \bar{y}, \tau)\right) d\bar{y}. \tag{3.56c}$$

In order to make the residual averaged over the domain to zero, we choose the weight function ω_1 appropriately, and make them orthogonal to the residual error. In the Galerkin approach, the test function itself is the weight function, $\phi_1 = \omega_1$. Therefore,

$$\langle \mathscr{R}, \omega_1 \rangle \equiv \int_0^h \mathscr{R}\, \omega_1 \, dy = 0. \tag{3.57}$$

This yields the following set of coupled partial differential equations for the interface thickness, and the local flow rate, which is written in the following form using variables t and x:

$$\begin{aligned} q_t = &-\frac{17}{7}\frac{q\, q_x}{h} + \frac{9}{7}\frac{q^2\, h_x}{h^2} - \frac{5}{2\,Re}\frac{q}{h^2} + \frac{5}{3\,Re}h - \frac{5\cot\theta}{3Re}hh_x + \frac{5\,We}{6}hh_{xxx} \\ &+ \hat{\tau}_{w0}\left(\frac{5}{4\,Re} - \frac{19\hat{\tau}_{w0}}{672}h^2 h_x - \frac{19}{336}hq_x - \frac{5}{112}qh_x + \frac{5\,\nu}{4Re}\hat{\tau}_{w1}[h]\right), \end{aligned} \tag{3.58}$$

$$h_t + q_x = 0. \tag{3.59}$$

The terms in parentheses multiplying $\hat{\tau}_{w0}$ in equation (3.58) correspond to the influence of the turbulent gas flow. By setting $\hat{\tau}_{w0}$ to zero, we recover the first-order WIBL approximation for a free-falling liquid film developed by Ruyer-Quil and Manneville (2000).

3.5. Results

3.5.1. Linear stability analysis

A flat liquid film ($h = 1$) is a solution to the system of equations (3.58)-(3.59). To understand the stability of this solution to infinitesimal disturbances, we substitute $h = 1 + f$, $q = \frac{2}{3} + \frac{\hat{\tau}_{w0}}{2} + g$, where $|f| \ll 1$ and $|g| \ll 1$ in equations (3.58)-(3.59), and retaining only the first-order terms results in the following set of equations,

$$f_t + g_x = 0, \tag{3.60}$$

$$g_t = -\frac{17}{7}\left(\frac{2}{3}+\frac{\hat{\tau}_{w0}}{2}\right)g_x + \frac{9}{7}\left(\frac{2}{3}+\frac{\hat{\tau}_{w0}}{2}\right)^2 f_x - \frac{5}{2Re}\left(g - \frac{4}{3}f - \hat{\tau}_{w0}f\right) + \frac{5}{3Re}f - \frac{5\cot\theta}{3Re}f_x + \frac{5We}{6}f_{xxx} + \hat{\tau}_{w0}\left(-\frac{19}{672}\hat{\tau}_{w0}f_x - \frac{19}{336}g_x - \frac{5}{112}\left(\frac{2}{3}+\frac{\hat{\tau}_{w0}}{2}\right)f_x + \frac{5\,\nu}{4Re}\hat{\tau}_{w1}[f]\right). \quad (3.61)$$

Looking for solutions in the form of normal modes, i.e., $(f, g) = (\bar{f}, \bar{g})\,\mathrm{e}^{s(k)t+\mathrm{i}kx}$, where $s(k)$ is the frequency and k is the wavenumber, from equations (3.60) and (3.61), we have the following dispersion relation

$$s^2(k) + \frac{1}{336Re}\Big(840 + \mathrm{i}Re(544 + 427\hat{\tau}_{w0})k\Big)s(k) + \frac{5We}{6}k^4 + \frac{1}{336Re}\Big(-Re(192 + 91\hat{\tau}_{w0}^2 + 278\hat{\tau}_{w0}) + 560\cot\theta\Big)k^2 + \mathrm{i}\frac{5}{4Re}\left(4 + 2\hat{\tau}_{w0} + \nu\hat{\tau}_{w0}\tau_{w1}\left(\frac{k}{\nu}\right)\right)k = 0. \quad (3.62)$$

When there is no gas flow, the flat film solution is stable for $Re < Re_c \equiv 5\cot\theta/4$, which is consistent with previous results (Benjamin, 1957; Yih, 1963). But for $Re > Re_c$, we have a band of wavenumbers k for which the solution is unstable. For the vertical setting ($\theta = \pi/2$) considered here in the computations that follow, the flat film solution becomes unstable when $Re = 0$. Figure 3.3 shows the growth rate as a function of wavenumber for the most unstable eigenvalue and for the vertical configuration.

We can observe that the cocurrent turbulent gas flow is destabilising in nature, as the growth rate is amplified (solid curve) when compared to the 'no-gas' situation (dashed curve). From figure 3.4, where we plot the phase velocity of the most amplified disturbance as a function of wavenumber, we see that the cocurrent gas flow increases the wave speed as expected.

3.5.2. Non-linear waves

Travelling waves are known to exist for free-falling liquid films, and we expect to find such solutions in the presence of gas flow. To analyze such waves, we rewrite the equations obtained from the WIBL model ((3.58)-(3.59)) in a frame of reference moving with speed c, and for simplicity we consider a vertical setting ($\cot\theta = 0$). We then have

$$-ch_x + q_x = 0, \quad (3.63a)$$

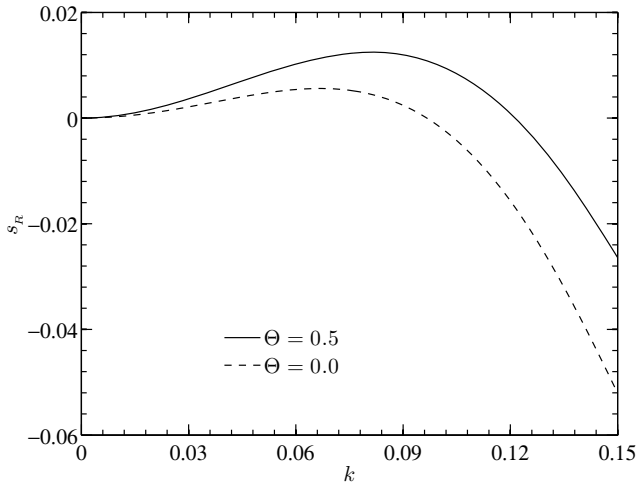

Figure 3.3.: Dependence of the growth rate on the wavenumber for $Re = 5.0$, $\theta = \pi/2$, $Ka = 1988.5$, $N = 0.4$, $\Theta = 0$ (dashed curve) and $\Theta = 0.5$ (solid curve).

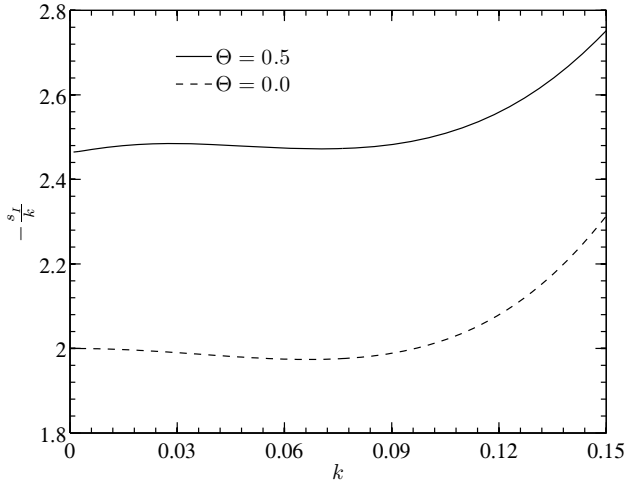

Figure 3.4.: Dependence of the phase velocity on the wavenumber for $Re = 5.0$, $\theta = \pi/2$, $Ka = 1988.5$, $N = 0.4$, $\Theta = 0$ (dashed curve) and $\Theta = 0.5$ (solid curve).

$$-cq_x = -\frac{17}{7}\frac{q\,q_x}{h} + \frac{9}{7}\frac{q^2\,h_x}{h^2} - \frac{5}{2\,Re}\frac{q}{h^2} + \frac{5}{3\,Re}h + \frac{5\,We}{6}hh_{xxx} + \hat{\tau}_{w0}\left(\frac{5}{4\,Re} - \frac{19\hat{\tau}_{w0}}{672}h^2h_x - \frac{19}{336}hq_x - \frac{5}{112}qh_x + \frac{5\nu}{4Re}\hat{\tau}_{w1}[h]\right). \quad (3.63b)$$

We have retained the same independent variable 'x' for the moving coordinate for convenience. Here, we focus only on fast waves (traveling faster than infinitesimally small waves), in particular on the γ_2 family of periodic solutions for free-falling films, in terms of

the classification of permanent waves given by Chang and Demekhin (2002). The solitary-wave limit of such waves corresponds to a single-hump solitary wave and is represented by a homoclinic orbit in the phase space of the corresponding dynamical system (Balmforth, 1995; Chang and Demekhin, 2002; Kalliadasis et al., 2012). Single-hump solitary waves, are characterised by a single-hump/elevation followed by rapidly decaying capillary ripples at the wavefront, and travel faster than the small-amplitude waves. We consider waves in two different settings – in one, the film thickness is fixed to unity at infinity, i.e., $h \to 1$ as $x \to \pm\infty$ (this corresponds to solitary waves), and in another one, we fix the mass flow rate under a wave to a constant, which is accomplished by taking $1/(2\mathrm{W})\int_{-W}^{W} h\,dx = 1$, where W is taken to be the half-length of the domain of integration (this corresponds to periodic travelling waves). As a first step, we integrate equation (3.63a) once to obtain

$$-ch + q = C_0, \tag{3.64}$$

where, C_0 is the constant of integration that corresponds to the deviation in the liquid flow rate from that of the waveless flat film solution.

Solitary waves ($h = 1$, as $x \to \pm\infty$)

When $h \to 1$ as $x \to \pm\infty$, we have $q \to 2/3 + \hat{\tau}_{w0}/2$. Therefore, in equation (3.64) $C_0 = -c + 2/3 + \hat{\tau}_{w0}/2$, and we can eliminate q in equation (3.63b) by substituting $q = c(h-1) + 2/3 + \hat{\tau}_{w0}/2$ to obtain

$$\begin{aligned} h^3 h_{xxx} + \frac{1}{35\,We}\Big(-6c^2h(h+1) + 4ch + 6(3c-2)^2\Big)h_x \\ + \frac{\hat{\tau}_{w0}}{280\,We}\Big(24ch - 432c + 288 - 34ch^3 + 15ch^2 - 10h^2\Big)h_x \\ + \frac{\hat{\tau}_{w0}^2}{560\,We}\left(216 - 19h^4 - 15h^2\right)h_x - \frac{3}{WeRe}\left(c(h-1) + \frac{2}{3}\right) \\ + \frac{3\hat{\tau}_{w0}}{2\,WeRe}\Big(h^2\left(1 + \nu\hat{\tau}_{w1}[h]\right) - 1\Big) + \frac{2}{WeRe}h^3 = 0. \end{aligned} \tag{3.65}$$

To solve for the additional variable in the form of the wave velocity c, we take the derivative of the interface h to be vanishing at the midpoint of the domain, $h_x|_{x=0} = 0$. This system of equations is solved numerically on a periodic domain with spectral discretisation along the spatial direction. We adopt helium(g)-methanol(l) as working fluids in our study, which were considered by Zapke and Kröger (2000a,b) in their counter-current gas-liquid

flow experiments. The physical properties of the fluids are as follows:

$$\rho_g = 0.165\,\mathrm{kg/m^3}, \quad \mu_g = 2 \times 10^{-5}\,\mathrm{Pa\ s}, \tag{3.66a}$$

$$\rho_\ell = 791\,\mathrm{kg/m^3}, \quad \mu_\ell = 5.75 \times 10^{-4}\,\mathrm{Pa\ s}, \quad \sigma = 22 \times 10^{-3}\,\mathrm{N/m}, \tag{3.66b}$$

which in terms of dimensionless numbers are given by

$$Ka = 1988.5, \quad N = 0.4. \tag{3.67}$$

To analyse the dependence of the wave velocity c on the liquid Reynolds number Re, we solve equation (3.65) along with the first-derivative condition mentioned above implementing Keller's pseudo-arclength continuation algorithm (Keller, 1977). The details of the algorithm are provided in Appendix B.

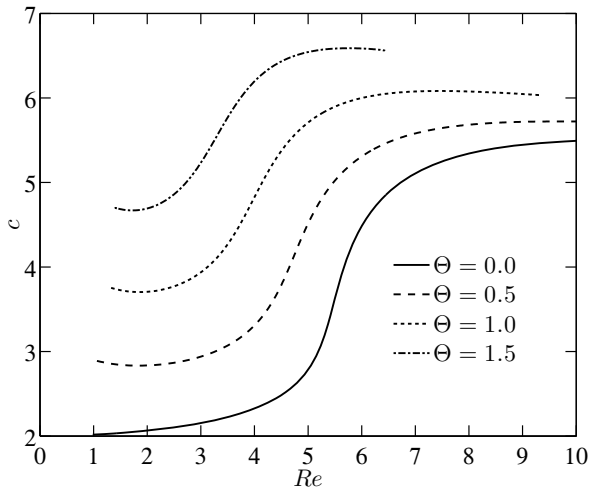

Figure 3.5.: Dependence of the solitary-wave speed c on the Reynolds number Re for various values of gas shear parameter Θ, with $\theta = \pi/2$, $Ka = 1988.5$ and $N = 0.4$ for a domain size of 900 dimensionless units.

Continuation along *Re* Figure 3.5 shows the dependence of the wave speed c on the liquid Reynolds number Re for various values of the gas shear parameter Θ. The solitary waves are computed on a sufficiently long periodic domain with a period of 900 dimensionless units. For a given Θ, it can be observed that the wave speed c increases with Re before coming to a near saturation or exhibiting turning point (figure 3.6) at higher Re. We note that the curve obtained for $\Theta = 0$ is qualitatively similar to that obtained by Demekhin et al. (2010) for water-air as working fluids in a falling film problem. For

smaller Re, where the flow is governed by viscous drag and gravity, c increases rapidly, and for larger Re where inertia becomes important, we have a plateau-like region for c.

As we increase Θ, the wave speed increases for a given Re. This is only to be expected as the gas flowing in the same direction as the liquid would only increase the speed of the wave further. At higher speeds of the solitary wave, there is a rise in the amplitude of the hump followed by more pronounced capillary ripples at the wave front. In this regime, the shear force due to the co-flowing gas flow becomes important in addition to the viscous drag, gravity, inertia and surface tension. It is important to note that the solitary wave attains a higher speed for larger Θ, even for moderately small values of the liquid Reynolds number Re. As Re increases further, the capillary waves become appreciably large and a large domain is required is compute the solitary waves. Thus, the presence of the turning points shown in figure 3.6 may be attributed, at least partly, to the domain size. This unphysical behaviour could also be a signature of the high degree nonlinearities present in equation (3.65), similar to that observed with the Benney's equation (leading to a blowup) and the full second-order model for the falling film (Scheid et al., 2006). However, the single-hump solutions of the top branch are expected to be more stable as such waves are observed in falling film experiments.

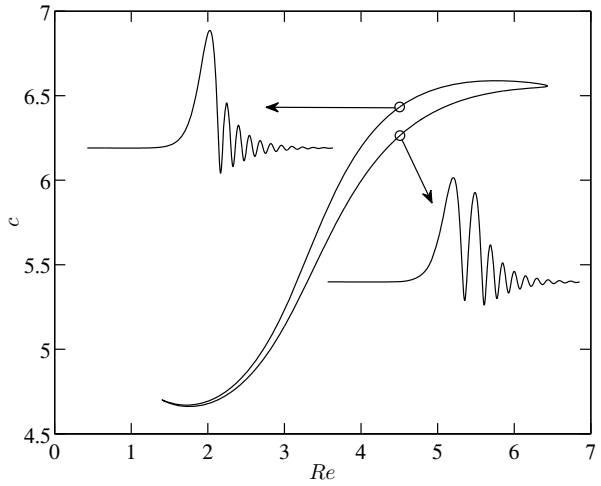

Figure 3.6.: Dependence of the solitary-wave speed c on the Reynolds number Re, showing turning points for $\Theta = 1.5$, $\theta = \pi/2$, $Ka = 1988.5$ and $N = 0.4$ for a domain size of 900 dimensionless units.

Some of the other characteristics of the solitary waves, namely the maximum and minimum of the free surface, $\max(h)$ and $\min(h)$, are plotted as functions of Re for various values of Θ in figures 3.7 and 3.8, respectively. In the absence of turbulent gas flow ($\Theta = 0$),

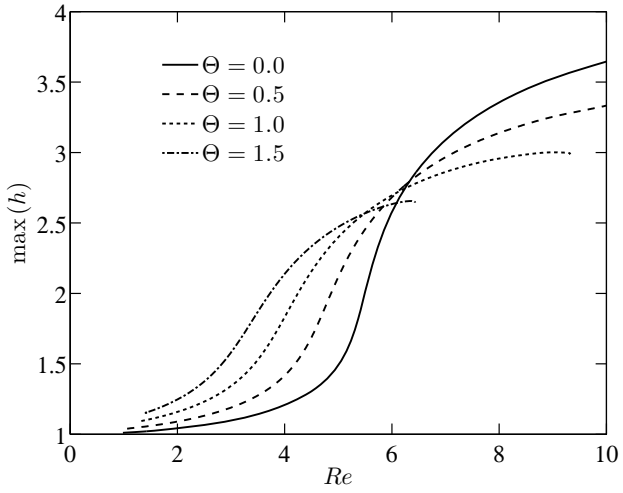

Figure 3.7.: Dependence of the maximum height of the solitary wave on the Reynolds number Re for various values of gas shear parameter Θ, with $\theta = \pi/2$, $Ka = 1988.5$ and $N = 0.4$ for a domain size of 900 dimensionless units.

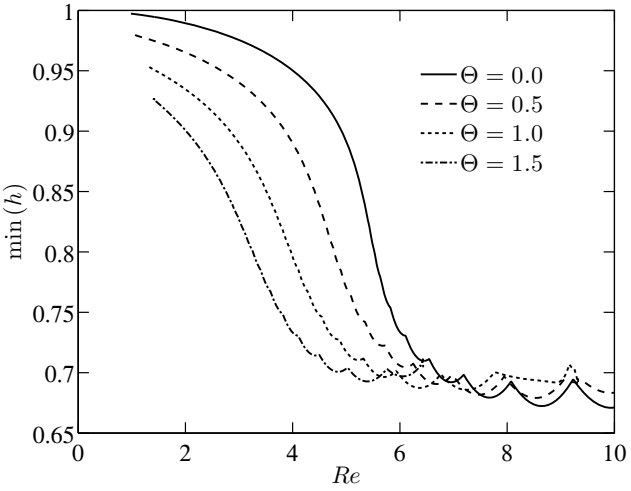

Figure 3.8.: Dependence of the minimum height of the solitary wave on the Reynolds number Re for various values of gas shear parameter Θ, with $\theta = \pi/2$, $Ka = 1988.5$ and $N = 0.4$ for a domain size of 900 dimensionless units.

both the maximum and the minimum of the wave height tend to unity, as we approach $Re = 0$ implying that h approaches unity. For nonzero Θ, the maximum increases with increasing Re (implying the increase in the height of the hump) whereas the minimum decreases with increase in Re. The number of capillary ripples increases significantly at high Re, which requires sufficiently large number of collocation points to resolve them

accurately (especially the dimples and bumps). The small spikes observed at high Re in figure 3.8 is a numerical effect as the number of collocation points used were not sufficient to precisely capture the dimples and bumps.

From the solitary-wave profiles shown in figure 3.9 for various values of the gas shear parameter Θ at $Re = 5$, we can observe the increase in the wave height for increasing Θ, and the capillary ripples become more pronounced.

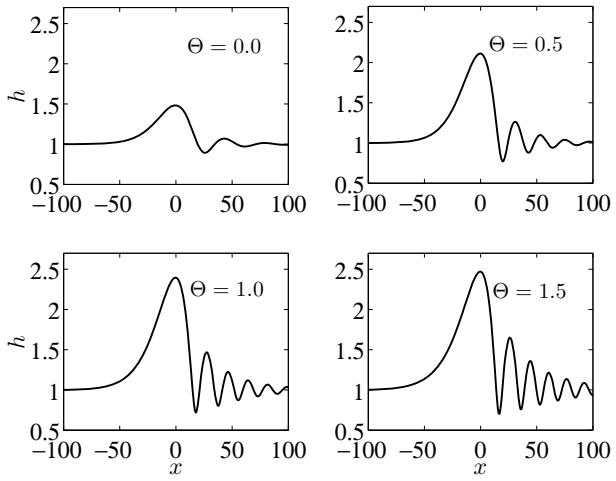

Figure 3.9.: Solitary-wave profiles for various values of the gas shear parameter Θ at $Re = 5.0$, $\theta = \pi/2$, $Ka = 1988.5$ and $N = 0.4$ for a domain size of 900 dimensionless units. Only a part of the domain is shown for the sake of clarity.

Continuation along Θ We have also performed numerical continuation along the gas shear parameter Θ for two values of the liquid Reynolds number, $Re = 3, 5$. The continuation results shown in figure 3.10 indicate that c indeed increases with Θ, which is again consistent with our previous observations. The numerical values for the wave speed obtained from both continuation approaches show excellent agreement.

Travelling waves

Instead of fixing the thickness of the flat film to unity, we now fix the volume under the wave to a constant value which is equivalent to keeping the mean film thickness constant. In this fixed-volume setting, we eliminate q in equation (3.63b) by substituting $q = C_0 + ch$

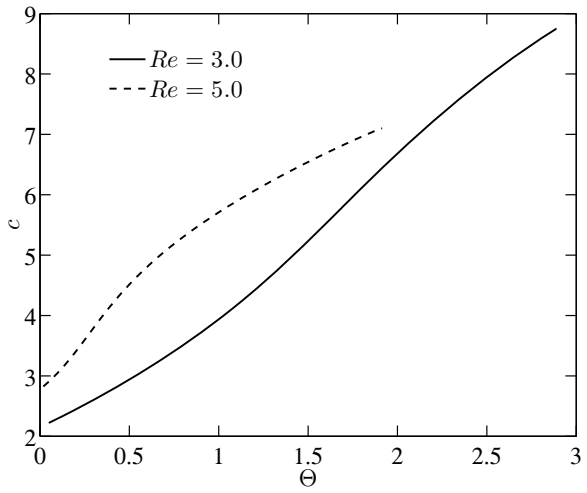

Figure 3.10.: Dependence of the solitary-wave speed c on the gas shear parameter Θ for $Re = 3.0$ and $Re = 5.0$, with $\theta = \pi/2$, $Ka = 1988.5$ and $N = 0.4$ for a domain size of 900 dimensionless units.

to obtain

$$h^3 h_{xxx} + \frac{6}{5\,We}\Bigg(c^2h^2 - \frac{17}{7}\,(C_0 + ch)\,ch + \frac{9}{7}\,(C_0 + ch)^2 - \frac{19}{672}\hat{\tau}_{w0}^2 h^4 - \frac{19}{336}\hat{\tau}_{w0} c h^3 - \frac{5}{112}\hat{\tau}_{w0} h^2\,(C_0 + ch)\Bigg) h_x + \frac{2}{WeRe}h^3 - \frac{3}{WeRe}\left(C_0 + ch - \frac{\hat{\tau}_{w0}}{2}h^2\Big(1 + \nu\hat{\tau}_{w1}[h]\Big)\right) = 0. \tag{3.68}$$

As before, we impose the condition $h_x|_{x=0} = 0$. Also, since the additional unknown C_0 is introduced, we impose an additional integral condition which is the equation for the constant mass under the wave, i.e., $1/(2\mathrm{W})\int_{-W}^{W} h\,dx = 1$. Here, the period of integration is taken to be 600 dimensionless units. We solve equation (3.68) together with the derivative and integral conditions using a spectral method.

Continuation along *Re* As in the previous section, we carry out continuation along Re by fixing Θ. Figure 3.11 shows the variation of c as a function of Re, obtained from numerical continuation. Though there is a general trend of c increasing as Re increases, we can identify a number of differences compared to the case with the constant film thickness in the far field. In comparison, the increase of c with Re appears to be slower, but there is also a slow and steady decrease in c beyond some Re (for $\Theta = 1.5$). This is due to the

fact that fixing the volume under a wave results in a decrease in the height of the flat film region as Re increases (hence a more constrained increase in the wave amplitude), and as the wave speed is proportional to its amplitude, the speed has to decrease. In other words, solitary waves travel faster than periodic travelling waves.

In figure 3.14, we plot the profiles of the free surface which also reveal the decrease in the thickness of the flat film sufficiently far from the hump. Furthermore, the maximum and the minimum of the wave profiles, plotted respectively in figures 3.12 and 3.13, indicate that the amplitude is smaller when compared with the case in which the flat film thickness is fixed to unity in the far field.

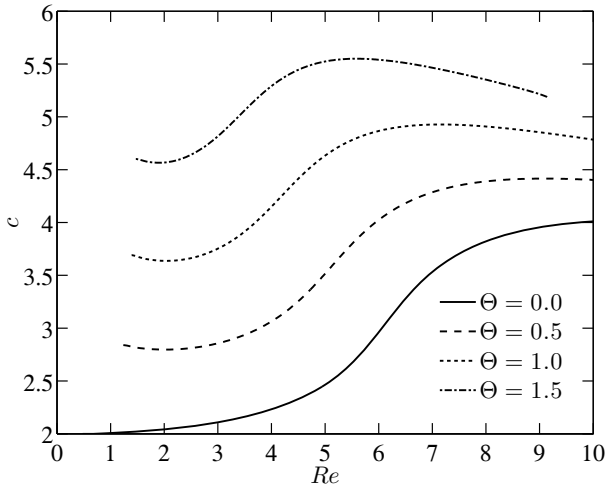

Figure 3.11.: Dependence of the travelling-wave speed c on the Reynolds number Re for various values of gas shear parameter Θ (fixed volume condition), with $\theta = \pi/2$, $Ka = 1988.5$, $N = 0.4$ and $W = 300$.

The variation of the wave velocity c with the gas flow parameter Θ shown in figure 3.15, indicates that c increases as Θ increases but at a slightly slower rate.

It should be noted that our time-dependent computations of the WIBL model on a periodic domain of dimensionless length 600 show that the number of single-hump waves arising in the computational domain depends on the chosen initial conditions. For instance, in section 3.5.3 we discuss the case when the initial conditions are small-amplitude sinusoidal disturbances of the flat-film solution, and the interface evolves into a superposition of four single-hump waves of approximately the same shape. Therefore, to make a comparison with our time-dependent computations presented in section 3.5.3, it turns out it is more appropriate to compute travelling waves on a smaller domain of length 150 dimensionless units. The dependence of c on Re shown in figure 3.16 reveals a non-

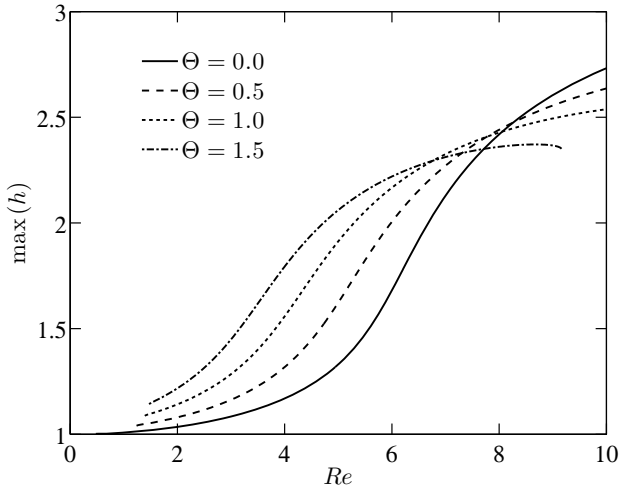

Figure 3.12.: Dependence of the maximum height of the travelling wave on the Reynolds number Re for various values of gas shear parameter Θ (fixed volume condition), with $\theta = \pi/2$, $Ka = 1988.5$, $N = 0.4$ and $W = 300$.

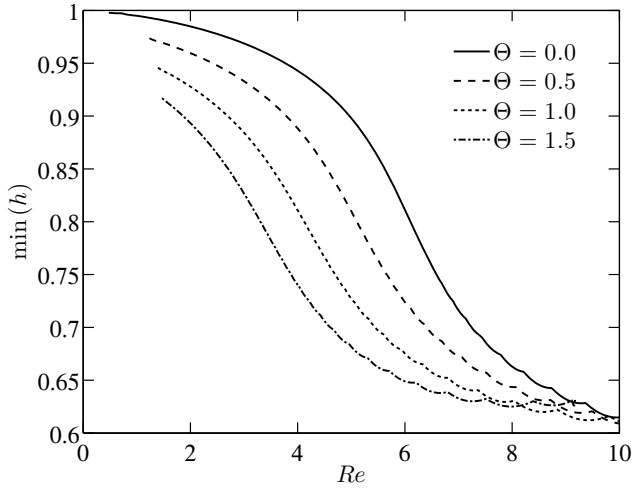

Figure 3.13.: Dependence of the minimum height of the travelling wave on the Reynolds number Re for various values of the gas shear parameter Θ (fixed volume condition), with $\theta = \pi/2$, $Ka = 1988.5$, $N = 0.4$ and $W = 300$.

monotonic behaviour, particularly with increasing gas shear ($\Theta = 1.5$), also exhibiting multiple solutions. As our domain is not sufficiently long, the interface at the far field is no longer flat, instead it reveals a wiggly structure corresponding to interacting waves present in a longer domain. However, the wave profiles on various branches show a similar structure (see figure 3.17), as the wave interaction is expected to be only weak in the

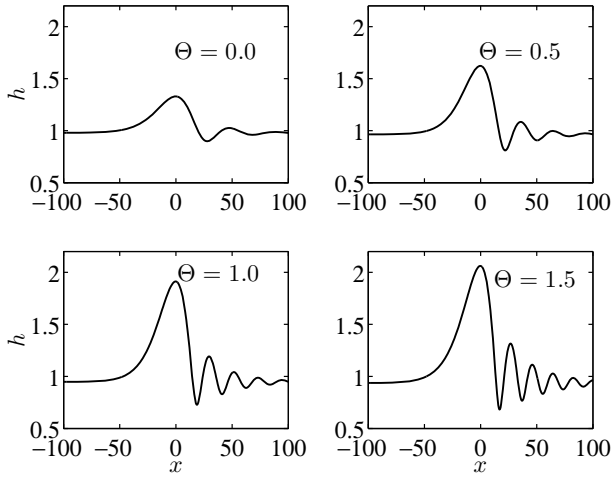

Figure 3.14.: Travelling-wave profiles for various values of the gas shear parameter Θ at $Re = 5.0$ (fixed volume condition), with $\theta = \pi/2$, $Ka = 1988.5$, $N = 0.4$ and $W = 300$. Only a part of the domain is shown for the sake of clarity.

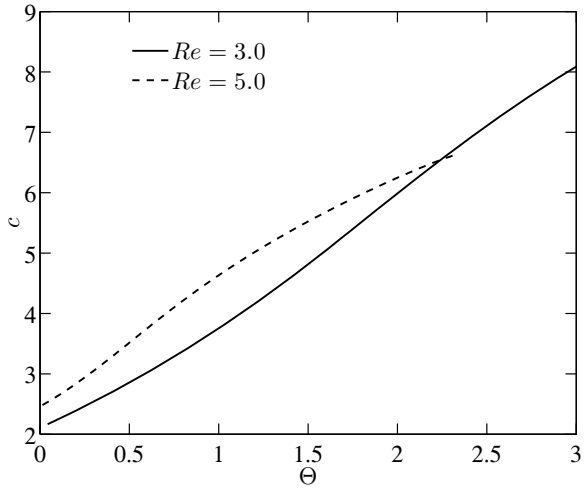

Figure 3.15.: Dependence of the travelling-wave speed c on the gas shear parameter (Θ) for $Re = 3.0, 5.0$, with $\theta = \pi/2$, $Ka = 1988.5$, $N = 0.4$ and $W = 300$.

regime considered. The comparison between the steady travelling-wave profiles and the profiles obtained in the time-dependent computations is discussed in section 3.5.3.

3.5.3. Time-dependent computation

To understand the spatiotemporal evolution of the gas-liquid interface under the influence of turbulent gas flow, we need to solve equations (3.58)-(3.59) as an initial value problem.

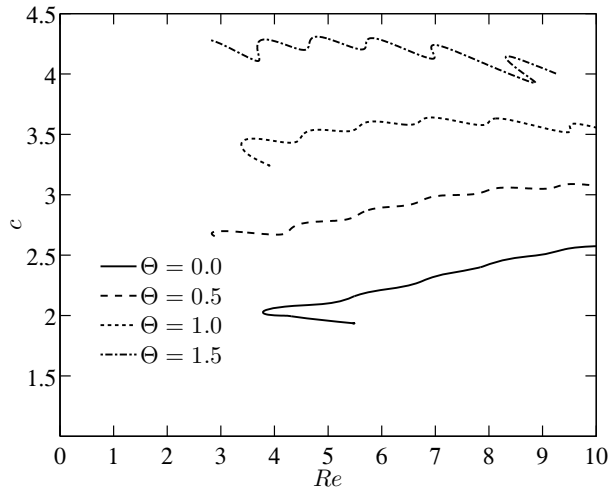

Figure 3.16.: Dependence of the travelling-wave speed c on the Reynolds number Re for various values of gas shear parameter Θ (fixed volume condition) on a smaller domain ($W = 75$), with $\theta = \pi/2$, $Ka = 1988.5$ and $N = 0.4$.

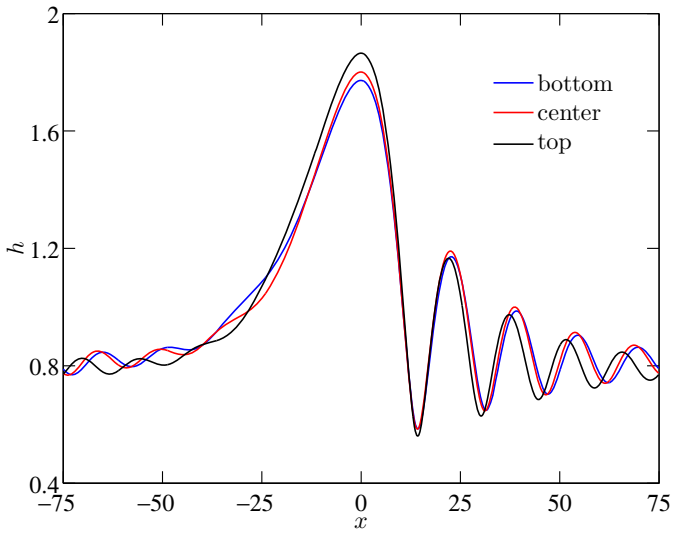

Figure 3.17.: Travelling-wave profiles for the bottom, center and top branches at $Re = 8.5$ and $\Theta = 1.5$ (fixed volume condition) on a smaller domain ($W = 75$), with $\theta = \pi/2$, $Ka = 1988.5$ and $N = 0.4$.

This is carried out numerically using a Fourier pseudo-spectral representation of the spatial derivatives and an adaptive stepping in time. The details of the numerical scheme are provided in Appendix C. To investigate the influence of gas flow on the dynamics of the liquid film, we increase Θ in steps of 0.5 starting from 0, for every 1000 dimensionless time

units, during which we track the spatiotemporal evolution of h and q by solving equations (3.58)-(3.59). We choose the initial condition of the interface to be a flat film ($h = 1$), superimposed with a sinusoidal disturbance of amplitude 0.05 in the absence of turbulent gas. The liquid Reynolds number is fixed to be $Re = 5$. The equations are integrated on a periodic domain $[-300, 300]$ for sufficiently long time, say till $t \approx 10000$. The interface attains a nearly steady traveling-wave state, whereby the unsteadiness is attributed to the interaction between individual waves. The corresponding spatiotemporal profile for a free-falling liquid film when the wave profile attains such a state is shown as a space-time plot in figure 3.18 (for $t = 9000 - 10000$). The darker regions correspond to larger h, whereas the brighter regions correspond to smaller h, with the shading done following the color bar in figure 3.18. A snapshot of the actual profile is shown in figure 3.19a. The lines in the space-time plot show the trace of peaks/humps of the traveling waves, and their inverse slopes correspond to the wave speed. The solution for the film thickness h and the flow rate q at $t = 10000$ is used as the initial condition, when we introduce the gas flow that is turbulent in nature.

To introduce the gas flow, we set $\Theta = 0.5$ corresponding to the friction velocity $U_f^* = 0.94\,\mathrm{m/s}$. From the space-time plot shown in figure 3.18 (for $t = 10000 - 11000$), we observe that the lines become more horizontal than for the free-falling case, implying that the waves travel faster with higher amplitudes. This is further confirmed by the interface profiles shown in figure 3.19b. We use the solution (h, q) at $t = 11000$ as an initial condition when we further increase the gas shear to $\Theta = 1.0$ with the corresponding friction velocity $U_f^* = 1.33\,\mathrm{m/s}$. We can observe the increase in the wave velocity and the height by noting that the lines become more horizontal (figure 3.18 (for $t = 11000 - 12000$)), and darker. The interfacial wave profiles shown in figure 3.19c clearly indicate that their amplitudes are larger when compared with the previous cases, $\Theta = 0, 0.5$. The increase of the speed and amplitude of the waves is again observed as we increase Θ further to 1.5 corresponding to $U_f^* = 1.63\,\mathrm{m/s}$ (shown in figure 3.18 for $t = 12000 - 13000$ and the interface profiles in figure 3.19d). This trend is expected to continue until a point where the slope of the travelling-wave hump becomes infinitely large, which is also a signature of droplet entrainment into the gas stream. At this stage, the full Navier-Stokes equations for the gas and the liquid need to be used to describe the flow behaviour.

It can be observed that there are four waves in the computational domain of size 600 dimensionless units, chosen for the time-dependent computations. So it turns out more appropriate to compare the results of the time-dependent computations with the numerical-continuation results for the fixed-volume case on the domain of length 150 dimensionless units. This comparison can be justified by the fact that the amplitude and

speed of the travelling wave is significantly influenced by the domain size in the constant volume (constant mean height) condition. A comparison of the wave velocities obtained from both computations shows very good agreement, with the difference being smaller than 1%. This difference could be attributed to the presence of interactions (attractions–repulsions) between the waves in the entire domain in the time-dependent computations. Such interactions are not taken into account in our numerical-continuation computations. The wave profiles obtained from both the time-dependent simulations and the numerical-continuation computations ($W = 75$) also show very good agreement, as can be seen in figure 3.20.

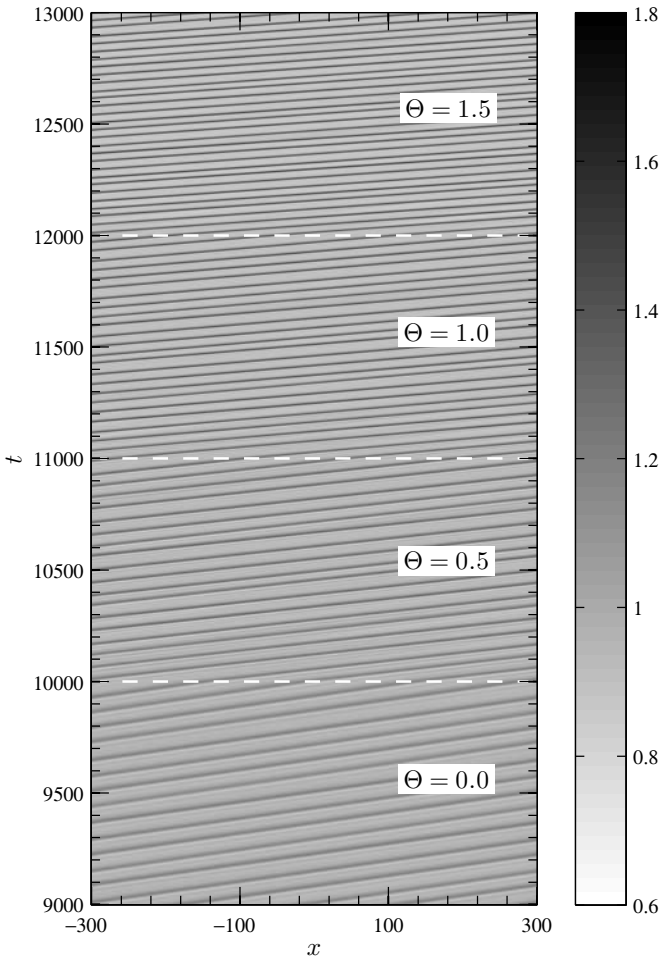

Figure 3.18.: Space-time plot of the gas-liquid interface at $Re = 5$ for various strengths of the gas shear, with $\theta = \pi/2$, $Ka = 1988.5$ and $N = 0.4$. Brighter regions correspond to small amplitudes, and darker regions correspond to large amplitudes. Ripples can be seen clearly when the figure is zoomed in.

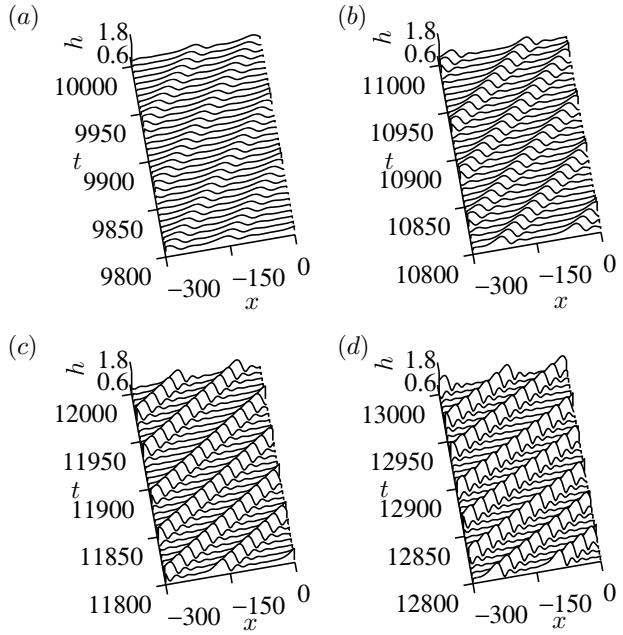

Figure 3.19.: Time evolution of the gas-liquid interface, for $\Theta = 0, 0.5, 1.0$ and 1.5, or, equivalently, U_f^*=0, 0.94, 1.33 and 1.63 m/s, with $\theta = \pi/2$, $Ka = 1988.5$ and $N = 0.4$.

3.6. Conclusion

We have analysed the dynamics of a thin liquid layer flowing under gravity down a planar vertical substrate in the presence of a co-flowing turbulent gas. The gas and liquid problems were solved separately by combining the fact that the viscosity of the gas is much smaller than that of the liquid and the following assumptions: the velocity in the liquid layer is much smaller than the mean velocity in the gas layer and that the turbulent fluctuations in the gas flowing over the liquid film decay in the same way as those in the gas flowing over a rigid wall.

The perturbations to the interfacial shear stress computed by solving the gas problem are used in the interfacial boundary conditions to solve the liquid problem. To describe the dynamics of the liquid layer, we have derived a weighted integral-boundary-layer (WIBL) model. We used this model to analyse the effect of the gas flow on single-hump solitary and travelling waves (γ_2 type), which are commonly observed in the falling film setting. For solitary waves we require that the film thickness approaches a given constant value in the far field, while for periodic travelling waves we require that the volume is kept fixed

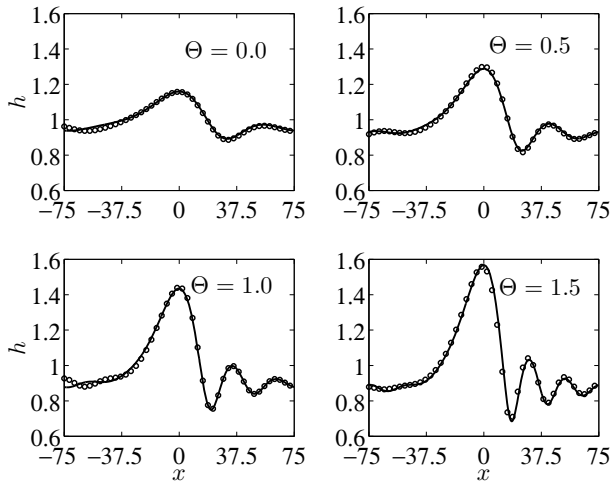

Figure 3.20.: Comparison of the wave profiles obtained by time-dependent computations on the periodic domain of dimensionless length 600 with the profiles of steady travelling waves obtained by continuation on the domain of dimensionless length 150, for various values of the gas shear parameter Θ at $Re = 5.0$, with $\theta = \pi/2$, $Ka = 1988.5$ and $N = 0.4$. The solid curves correspond to steady travelling waves obtained from continuation, whereas the open circles correspond to time-dependent simulations. Note that for the time-dependent simulations there are four waves in the domain and just one of them is selected and shown in each of the panels.

in one period. By taking helium and methanol as working fluids, we have computed such waves using Keller's pseudo-arclength continuation algorithm.

The dependence of the wave velocity on the liquid Reynolds number and the gas flow is analysed. It is found that the wave velocity increases with the liquid Reynolds number as well as the gas shear. This is markedly different from the counter-current setting, where, for a given liquid Reynolds number, the wave velocity decreases with increasing gas shear before changing direction at the flooding point. We have also compared our numerical continuation results with time-dependent computations of the WIBL model, showing very good agreement, with just a small mismatch in the wave velocity which can be attributed to the interaction (attraction and repulsion) between neighbouring waves in the computational domain.

It is noteworthy that in the existing literature, experimental studies were conducted at high liquid Reynolds numbers (e.g. Lioumbas et al. (2005, 2006, 2009)) and hence no direct comparisons between these studies and the present one valid for low liquid Reynolds number can be made. However, it is hoped that our study can motivate experimental

studies on this subject as well as additional theoretical studies in other settings where gas-liquid flows are pertinent. For instance, co-current gas-liquid flows also find applicability in the generation of droplets (Lasheras and Hopfinger, 2000), wherein the shearing action of a co-flowing high-speed gas stream over a slow-flowing liquid jet results in the formation of droplets of different sizes.

4. Stability analysis of countercurrent gas-liquid film flows

4.1. Introduction

As we have seen from the last chapter, the addition of a gas layer to the liquid film makes the system dynamics more complex and interesting. Demekhin (1981) and Trifonov (2010) analysed the gas-liquid problem by following the quasi-laminar approach of Miles (1957) and Benjamin (1957). Also Trifonov (2010) solved the full Navier-Stokes equation for the liquid problem whereas Demekhin (1981) developed an integral-boundary-layer model. Recently, Ó Náraigh et al. (2011) considered turbulent flow over a liquid layer by developing a single equation model for the turbulent part, further by solving the full problem they concluded that the waviness induced Reynolds stresses do not play a significant role in determining the stability of the interface. Tseluiko and Kalliadasis (2011) solved the countercurrent gas-liquid problem by using an improved version of the quasi-laminar approach of Miles (1957) and Benjamin (1957), in particular their solution to the gas problem was on a curvilinear boundary layer coordinate system, and developed long-wave and weighted-integral-boundary-layer models for the liquid problem.

Miesen and Boersma (1995) analysed the stability of a thin liquid film sheared by a co-flowing turbulent gas. By considering the dynamic effects of the gas, they found two modes of instability, namely the interfacial mode and the internal mode. The interfacial mode has a phase speed larger than the maximum velocity in the liquid layer, whereas the phase speed of the internal mode is smaller than the maximum velocity in the liquid film. They also compared their model calculations with experiments, further they tried to link the generation of roll waves with droplet entrainment. In another study, Boomkamp and Miesen (1996) provided a general classification of instabilities in parallel two-phase flows based on the energy transfer from the primary to the disturbed flow. They broadly grouped the existing studies on such instabilities under five different mechanisms, which depend on the properties of the flow system, viz, density stratification and orientation, curvature of the velocity profile, viscosity stratification, shear effects or a combination of

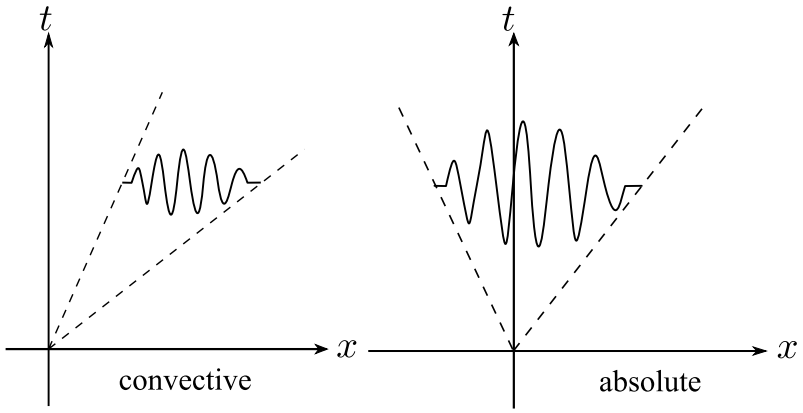

Figure 4.1.: Schematic representation of absolute and convective instabilities.

the last two. In a recent study, Dietze and Ruyer-Quil (2013) considered a thin liquid film in the presence of a confined laminar gas. By making use of the laminar nature of the flow, they developed a model based on the weighted-integral-boundary-layer approach for both the phases, also taking into account the viscous diffusion effects.

The theory of absolute and convective instabilities was first introduced in the field of plasma physics by Briggs (1964), and was later developed in fluid dynamics (Huerre and Monkewitz, 1990; Huerre, 2000). Absolute and convective instabilities are found in a variety of fluid flow settings such as liquid sheets and jets (Lin, 2003), combustion (Juniper, 2006) and many other flow processes. These instabilities are also analysed from a more general dynamical systems perspective, such as in the complex Ginzburg–Landau equation (Chaté and Manneville, 1996; Tobias et al., 1998), which is used as a model system for a variety of physical systems.

In general, the nature of the instability is determined by examining the response of the linear system to a localised disturbance. If the growing disturbance gets advected and moves away from the point of initiation, then the instability is convective. In other words, if the long-time behaviour of the system decays along the ray $x/t = 0$, then the system is said to be convectively unstable (see figure 4.1). On the other hand, if the disturbance grows at every point in space, then the instability is absolute. Convectively unstable flows are also referred to as 'spatial amplifiers', whereas absolutely unstable flows act like an 'oscillator' (Huerre, 2000).

The approach of Briggs (1964) was to determine the long-time asymptotic behaviour of the perturbation of the form $\mathrm{e}^{\mathrm{i}kx+s(k)t}$ by solving the linear system of equations using Laplace and Fourier transforms. According to Briggs criterion for the onset of absolute instability, the solution of the dispersion relation is not only a saddle point where the two

spatial branches on the complex k plane coalesce, but also a pinch point with $Re[s(k)] > 0$. At this point, the group velocity of the wave packets vanishes. Brevdo et al. (1999) were one of the first to analyse absolute and convective instabilities in a falling film setting by solving the Orr–Sommerfeld problem. These authors considered two different techniques to analyse absolute-convective instabilities, one based on the exact Briggs collision criterion, and the other based on the tracking of the saddle point. They developed an algorithm to numerically continue the position of the saddle point which provides the leading-order contribution to the inverse Fourier Laplace transforms. However they found only a convective instability from their numerical studies as expected. Suslov (2006) developed a more complicated algorithm that calculates the absolute-convective stability boundary in the given parameter space. Joo and Davis (1992) analysed instabilities in three-dimensional falling films over vertical plates by studying Benney's long-wave evolution equation, and demonstrated that the instability exhibited in such configurations is of convective type. Lin and Kondic (2010) also considered absolute-convective instabilities in their study on thin film flows on inverted substrates. In a very recent study, Ó Náraigh et al. (2013) analysed absolute and convective instabilities of a thin liquid film sheared by a fully developed gas flow that could be laminar or turbulent. By combining linear modal and ray analyses, they calculated the regimes of such instabilities, further they also found that absolute instability exists for large values of density and viscosity ratios at high Reynolds numbers. Much earlier, Gaster (1962) demonstrated that the spatial growth rate could be obtained from the temporal one through an appropriate transformation, but such a transformation is only applicable for near-critical conditions.

In the present study, we begin with the formulation of a modified Orr–Sommerfeld (O-S) equation for the liquid problem incorporating the effects of counter-current gas flow. In a recent study, Tseluiko and Kalliadasis (2011) have developed a hierarchy of low-dimensional models, namely a long-wave model and a weighted-integral-boundary-layer (WIBL) model to analyse flooding in counter-current gas-liquid flows mainly focussing on single-hump solitary waves and periodic travelling waves. Their WIBL model is based on the methodology of Ruyer-Quil and Manneville (1998, 2000) for free-falling liquid films, obtained by combining a long-wave expansion with a polynomial representation of the velocity field, with the integral-boundary-layer approximation and the method of weighted residuals. The advantage with the WIBL model is that it could be applied for up to moderate Reynolds numbers. Making use of these two models, which are valid for a limited region in the parameter space, and the O-S equation that is valid for all values of Reynolds number and the wavenumber, we analyse the local stability of this flow system for the vertical configuration.

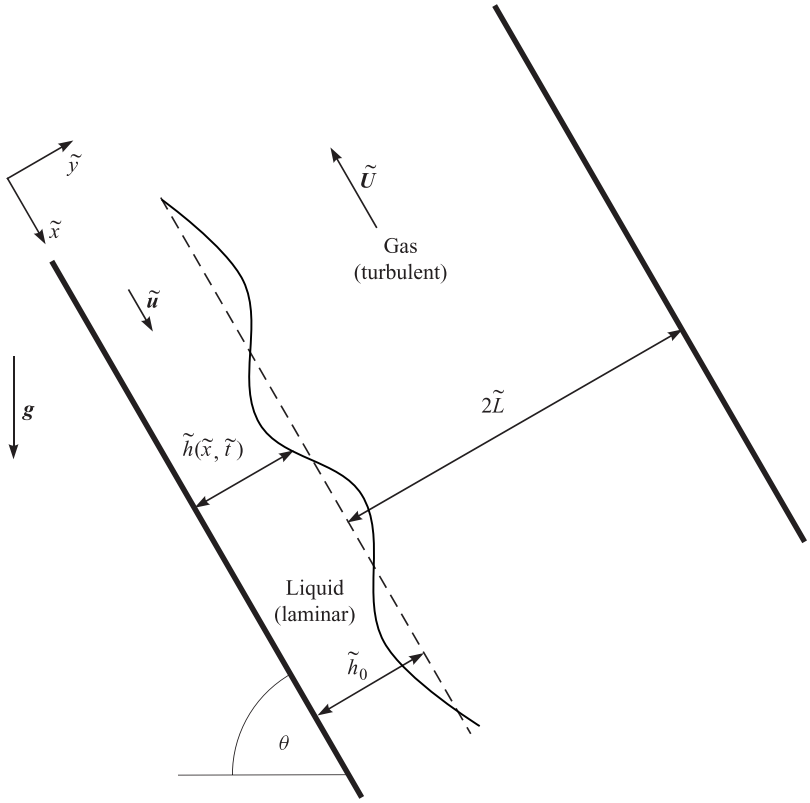

Figure 4.2.: Schematic illustration of a falling liquid film in contact with a countercurrent turbulent gas. θ is the inclination angle of the channel with respect to the horizontal.

This work is structured as follows: In section 4.2, we derive the modified O-S equation from the Navier–Stokes equations and the boundary conditions, and in section 4.3 we recall the low-dimensional models of Tseluiko and Kalliadasis (2011) and derive their linearised versions by considering the interface to be flat. By assuming normal mode solutions, we examine the temporal stability of the system in section 4.4, and in section 4.5 we devise a methodology to analyse absolute/convective instabilities, also explaining the numerical strategy employed in solving the O-S equation. The linear stability results are supplemented by time-dependent computations of the linearised WIBL model in section 4.6. Finally, we summarise our findings in section 4.7.

4.2. Formulation of modified Orr–Sommerfeld problem

4.2.1. Dimensionless governing equations

Our prototypical system consists of a two-dimensional channel that is inclined at an angle θ with respect to the horizontal with the gas flow in the negative x direction, as depicted in figure 4.2. To derive the Orr–Sommerfeld equation for gas-liquid film flow in an inclined channel, we begin by considering the dimensionless form of the Navier-Stokes equations (3.29a) - (3.29c) of chapter 3. Though the boundary conditions are very similar to the ones derived in section 3.4, we rewrite them here for completeness also accounting for the countercurrent gas flow. The no-slip and no-penetration boundary conditions at the bottom wall are

$$u = v = 0, \quad \text{at} \quad y = 0. \tag{4.1}$$

We have the following conditions at the gas-liquid interface. The kinematic condition is given by

$$h_t + uh_x = v, \quad \text{at} \quad y = h(x,t), \tag{4.2}$$

with the tangential stress condition given by

$$-\frac{1}{1+h_x^2}\left[2(u_x - v_y)h_x - (u_y + v_x)(1-h_x^2)\right] = \hat{\tau}_w[h] \quad \text{at} \quad y = h(x,t), \tag{4.3}$$

where $\hat{\tau}_w[h]$ is the shear stress at the interface due to countercurrent gas flow that could be computing using equations (3.32) and (3.33). The normal stress balance is given by

$$p = \hat{P}_w[h] + \frac{2}{1+h_x^2}\left[u_x h_x^2 - (u_y + v_x)h_x + v_y\right] - \frac{Re\ We\ h_{xx}}{(1+h_x^2)^{3/2}}, \quad \text{at} \quad y = h(x,t), \tag{4.4}$$

where $\hat{P}_w[h]$ is the contribution to the normal stress at the interface due to countercurrent gas flow ((3.34)–(3.35)). The dimensionless parameter, We is the Weber number that signifies the ratio of surface tension forces to the inertial forces (3.37).

We eliminate the pressure term from the Navier-Stokes equations (3.29a)–(3.29b) by cross-differentiation, followed by making use of the definition of the stream function, $u = \Psi_y$, $v = -\Psi_x$ to obtain

$$\left(\frac{\partial}{\partial t} + \frac{\partial \Psi}{\partial y}\frac{\partial}{\partial x} - \frac{\partial \Psi}{\partial x}\frac{\partial}{\partial y}\right)\nabla^2\Psi = \frac{1}{Re}\nabla^4\Psi. \tag{4.5}$$

4.2.2. Linear stability equations

The *base-state* stream function for the case of a flat-film in the presence of gas-shear at the interface is given by:

$$\psi_0 = -\left(\frac{y^3}{3} - y^2\right) + \frac{\hat{\tau}_{w0}}{2} y^2, \tag{4.6}$$

where it has been assumed that the width of the channel is much larger than the mean film thickness. As a next step, we shall introduce infinitesimal perturbations to the base flow by writing $\Psi = \psi_0 + \psi_1$, where $|\psi_1| \ll 1$. We make this substitution for Ψ in equation (4.5) and retain only the linear terms to obtain

$$\left(\frac{\partial}{\partial t} + u_0 \frac{\partial}{\partial x}\right) \nabla^2 \psi_1 - u_0'' \frac{\partial \psi_1}{\partial x} = \frac{1}{Re} \nabla^4 \psi_1, \tag{4.7}$$

where prime denotes differentiation with respect to y, and u_0 is the base-state velocity given by equation (4.6). Further, by writing the perturbation ψ_1 in the form of normal modes, $\psi_1 = \epsilon \phi(y) \mathrm{e}^{\mathrm{i}k(x-ct)}$, equation (4.7) results in the following classical Orr–Sommerfeld equation

$$\phi'''' - 2k^2 \phi'' + k^4 \phi = \mathrm{i}kRe \left[(u_0 - c)\left(\phi'' - k^2 \phi\right) - u_0'' \phi\right]. \tag{4.8}$$

The no-penetration and no-slip conditions at the bottom wall, respectively are

$$\phi(0) = 0, \qquad \phi'(0) = 0. \tag{4.9}$$

The perturbation to the flat interface can be represented as $y = h + \epsilon \eta(x,t)$. Therefore, the waveform of the interface disturbance is given by $\eta(x,t) = A_1 \mathrm{e}^{\mathrm{i}k(x-ct)}$, where A_1 is a complex quantity. Substituting these in equation (4.2), we obtain the linearised form of the kinematic condition

$$\phi(1) = (c - 1 - \hat{\tau}_{w0}) A_1, \tag{4.10}$$

and from the tangential stress balance condition (4.3), we have

$$\phi''(1) + k^2 \phi(1) - \left[|\hat{\tau}_{w0}| \nu \tau_{w1} (k/\nu) + 2\right] = 0. \tag{4.11}$$

The normal stress balance condition (4.4) becomes

$$\begin{aligned} &\phi'''(1) + k\left[\mathrm{i}Re(c - 1 - \hat{\tau}_{w0}) - 3k\right] \phi'(1) + \mathrm{i}kRe\hat{\tau}_{w0}\phi(1) \\ &-k\left[2\mathrm{i}\cot\theta + \mathrm{i}k^2 We Re + 2k\hat{\tau}_{w0} + \mathrm{i}|\hat{\tau}_{w0}|\nu P_{w1}(k/\nu)\right] A_1 = 0. \end{aligned} \tag{4.12}$$

The Orr–Sommerfeld (O-S) equation (4.8) together with the boundary conditions (4.9), (4.10), (4.11) and (4.12) constitute a generalised eigenvalue problem, where c has been taken as the eigenvalue.

4.3. Low-dimensional models and linearisation

Solving the full Navier-Stokes equations for the gas and liquid problems is an arduous task. To alleviate this difficulty, low-dimensional models that capture the essential physics of the underlying process for a range of values in the parameter space were developed by Tseluiko and Kalliadasis (2011). Here, we recall only the main ideas and the final equations, for details on the derivation the reader is referred to Tseluiko and Kalliadasis (2011).

4.3.1. Long-wave (LW) model

To derive the long-wave model, it is assumed that the waves are of long wavelength when compared to the thickness of the film. By applying the classical long-wave expansion for the velocity and pressure fields, first proposed by Benney (1966), Tseluiko and Kalliadasis (2011) obtained

$$h_t + 2h^2 h_x + \left(\left(\frac{8}{15} Re\, h^6 - \frac{2}{3} \cot\theta h^3 \right) h_x + \frac{1}{3} Re\ We\, h^3 h_{xxx} \right)_x + \frac{\hat{\tau}_{w0}}{2} \left(h^2 \left(1 + \frac{8Re}{15} h^3 h_x + \nu \hat{\tau}_{w1}[h] \right) \right)_x = 0. \quad (4.13)$$

By ignoring the terms multiplying $\hat{\tau}_{w0}$ in the parentheses that represent the effect of turbulent gas flow, we obtain the classic Benney's equation for the case of a falling film. Though this nonlinear PDE is probably the simplest possible model that correctly predicts the linear stability threshold for long waves, the disadvantage with this model is that it suffers finite-time blow up when Re exceeds a limiting value.

4.3.2. Weighted integral boundary layer (WIBL) model

In order to overcome the shortcomings of the long-wave model, we then consider the WIBL model derived in section 3.4.2. The coupled equations for the evolution of film thickness

(h) and the local flow rate (q) in the presence of countercurrent gas flow is given by

$$q_t = -\frac{17}{7}\frac{q\,q_x}{h} + \frac{9}{7}\frac{q^2\,h_x}{h^2} - \frac{5}{2\,Re}\frac{q}{h^2} + \frac{5}{3\,Re}h - \frac{5\cot\theta}{3Re}hh_x + \frac{5\,We}{6}hh_{xxx} + \hat{\tau}_{w0}\left(\frac{5}{4\,Re} - \frac{19\hat{\tau}_{w0}}{672}h^2h_x - \frac{19}{336}hq_x - \frac{5}{112}qh_x + \frac{5\,\mathrm{sign}\,(\hat{\tau}_{w0})\,\nu}{4Re}\hat{\tau}_{w1}[h]\right), \quad (4.14)$$

$$h_t + q_x = 0. \quad (4.15)$$

The terms multiplying $\hat{\tau}_{w0}$ corresponds to the influence of turbulent gas on the liquid film dynamics, and by setting $\hat{\tau}_{w0}$ to zero we recover the case of a free-falling liquid film (Ruyer-Quil and Manneville, 2000). The advantage with this WIBL model is that it is applicable for moderately large values of Re in addition to predicting the correct value for the linear stability threshold.

4.3.3. Linearised equations and dispersion relations

In order to understand the linear stability of the flat-film solution ($h = 1$), we linearise the equation (4.13) by substituting $h = 1 + f$, where $|f| \ll 1$ and retaining only the first-order terms, we obtain

$$f_t + af_x + bf_{xx} + cf_{xxxx} + d\,(\hat{\tau}_{w1}[f])_x = 0, \quad (4.16)$$

where

$$a = 2 + \hat{\tau}_{w0}, \quad b = \frac{8Re}{15} - \frac{2\cot\theta}{3} + \frac{4Re\hat{\tau}_{w0}}{15}, \quad c = \frac{Re\,We}{3}, \quad d = \frac{|\hat{\tau}_{w0}|\nu}{2}. \quad (4.17)$$

This linearised long-wave equation (4.16) represents the evolution of an infinitesimal perturbation f. We look for solutions in the form of normal modes, $f \propto \mathrm{e}^{s(k)t+\mathrm{i}kx}$ to obtain the following dispersion relation:

$$s(k) = -\mathrm{i}ak + bk^2 - ck^4 - \mathrm{i}dk\tau_{w1}\,(k/\nu)\,. \quad (4.18)$$

In a similar fashion, by substituting $h = 1 + f$ and $q = \frac{2}{3} + \frac{\hat{\tau}_{w0}}{2} + g$, where $|f| \ll 1$ and $|g| \ll 1$ in equations (4.14) and (4.15), the linearised form of the WIBL model is obtained as

$$f_t + g_x = 0, \quad (4.19)$$

$$g_t = -\left(\frac{34}{21}+\frac{61}{48}\hat{\tau}_{w0}\right)g_x - \frac{5}{2Re}g + \frac{5\,We}{6}f_{xxx} + \left(\frac{4}{7}+\frac{139}{168}\hat{\tau}_{w0}+\frac{13}{48}\hat{\tau}_{w0}^2-\frac{5\cot\theta}{3Re}\right)f_x + \frac{5}{2Re}\left(2+\hat{\tau}_{w0}\right)f + \frac{5\,\mathrm{sign}\left(\hat{\tau}_{w0}\right)\nu}{4Re}\hat{\tau}_{w0}\hat{\tau}_{w1}[f]. \quad (4.20)$$

As with the long-wave model, we look for solutions in the form of normal modes, $(f,g)\propto \mathrm{e}^{s(k)t+\mathrm{i}kx}$ to obtain the following quadratic dispersion relation:

$$\begin{aligned} s^2(k) + \frac{1}{336Re}\left[840+\mathrm{i}kRe\left(427\hat{\tau}_{w0}+544\right)\right]s(k) + \frac{5\,We}{6}k^4 \\ +\frac{1}{336Re}\left[-Re\left(192+278\hat{\tau}_{w0}+91\hat{\tau}_{w0}^2\right)+560\cot\theta\right]k^2 \\ +\mathrm{i}\frac{5}{4Re}\left[4+2\hat{\tau}_{w0}+\mathrm{sign}\left(\hat{\tau}_{w0}\right)\hat{\tau}_{w0}\nu\tau_{w1}\left(k/\nu\right)\right]=0. \end{aligned} \quad (4.21)$$

It should be noted that the linearised equations (4.19)–(4.20) and the dispersion relation (4.21) are very similar to the equations (3.60), (3.61) and (3.62) derived for the co-current case, with the only difference coming from the tangential wall shear terms corresponding to the countercurrent gas flow. The above set of dispersion relations (4.18), (4.21), along with the O-S system, (4.8)–(4.12) will be utilised in the stability calculations that will be presented in the following sections.

4.4. Temporal stability

In order to analyse the temporal stability of the system, the wavenumber k is taken to be real whereas c is complex. This implies that the real part of c gives the phase speed, whereas kc_i is the growth rate of the perturbation with c_i being the imaginary part of the complex quantity c.

4.4.1. Numerical method

The Orr–Sommerfeld equation (4.8) along with the boundary conditions (4.9)-(4.12) is solved using a Chebyshev pseudo-spectral method (Trefethen, 2000). By making use of the transformation $z=2y-1$, we map the physical film domain $0\le y\le 1$ onto the canonical interval $-1\le z\le 1$. Under this mapping, the O-S equation together with the boundary conditions become

$$\begin{aligned} 16\phi'''' - 8k^2\phi'' + k^4\phi - \mathrm{i}kRe\left[\left(\frac{z+1}{4}\right)\left(3+2\hat{\tau}_{w0}-z\right)\left(4\phi''-k^2\phi\right)+2\phi\right] \\ = -\mathrm{i}kcRe\left(4\phi''-k^2\phi\right), \end{aligned} \quad (4.22)$$

$$\phi(-1) = 0, \qquad \phi'(-1) = 0, \tag{4.23}$$

$$\phi(1) + (1 + \hat{\tau}_{w0})A_1 = cA_1, \tag{4.24}$$

$$4\phi''(1) + k^2\phi(1) - \big[|\hat{\tau}_{w0}|\nu\tau_{w1}(k/\nu) + 2\big]A_1 = 0, \tag{4.25}$$

$$\begin{aligned} &8\phi'''(1) - k\big[2\mathrm{i}\cot\theta + \mathrm{i}k^2\,WeRe + 2k\hat{\tau}_{w0} + \mathrm{i}|\hat{\tau}_{w0}|\nu P_{w1}(k/\nu)\big]A_1 \\ &-2k\big[\mathrm{i}Re(1 + \hat{\tau}_{w0}) + 3k\big]\phi'(1) + \mathrm{i}kRe\hat{\tau}_{w0}\phi(1) = -2\mathrm{i}kcRe\phi'(1), \end{aligned} \tag{4.26}$$

where the superscript prime denotes differentiation with respect to z. We could further eliminate A_1 from the system of equations using (4.25), followed by making the substitution for A_1 in the equations (4.24) and (4.26). By this, one could avoid appending the differentiation matrices with zeros and ones in order to solve for A_1. Nevertheless, as a general practice, we have done all our computations by retaining A_1 in our model system. But a comparison of the solutions obtained by both these approaches are exactly the same.

Boomkamp et al. (1997) developed a collocation method based on Chebyshev polynomials to solve the eigenvalue problem governing the stability of parallel two-phase flow, which is also similar to the methodology proposed by Orszag (1971) to investigate the stability of Poiseuille's flow. In this approach, we begin by expanding the eigenfunction $\phi(z)$ as a truncated series of Chebyshev polynomials, $T_i(z)$ (defined on the interval $[-1, 1]$),

$$\phi(z) = \sum_{i=0}^{M} a_{i+1}T_i(z), \tag{4.27}$$

with ϕ given on the Chebyshev points, $z_j = \cos(\beta_j)$, $\beta_j = (j-1)\pi/M$, $j = 1, \ldots, M+1$. In the 'FFT-based' formulation, Chebyshev differentiation is implemented by using the Fast Fourier Transform (Trefethen, 2000). The boundary conditions are imposed by replacing the last four rows (corresponding to the highest modes) with five boundary conditions that we have. This results in a matrix eigenvalue problem of the form

$$\mathbf{A}\mathbf{w} = c\mathbf{B}\mathbf{w}, \tag{4.28}$$

where $\mathbf{w} = (a_0, \ldots, a_M, A_1)^T$, and $\mathbf{A}$ and $\mathbf{B}$ are square matrices of size $M + 2$.

In the 'matrix-based' approach, as the name suggests, the derivative of a function is computed by matrix-vector multiplication. The entries of the differentiation matrix are computed by taking the analytical derivative of the interpolating polynomial, followed by evaluation at the Chebyshev points. To enforce the no-slip and no-penetration boundary conditions at the bottom wall, we follow the approach of Trefethen, of multiplying the interpolating polynomial by another polynomial (Trefethen, 2000), such that both the

conditions are satisfied implicitly. This approach would enable us to impose the bottom-wall boundary conditions accurately, i.e. exactly at the boundary point. This results in a matrix eigenvalue problem as before, but the square matrices **A** and **B** now are of size $M+1$.

The generalised eigenvalue problem (4.28) can be solved using a package such as MatLab. The large entries in **A** coming from the higher-order derivatives, and the null rows in **B** (coming from the bottom-wall boundary conditions) result in spurious and 'infinite' eigenvalues. We ignore such eigenvalues, and consider only the meaningful finite ones for our calculations. Typically, $20-30$ collocation points are sufficient to capture the essential behaviour of the system.

4.4.2. Case: No gas flow

Before proceeding further with the numerical solution to the original O-S problem for gas-liquid film flow, we shall switch off the gas flow to see if we can recover the analysis for a free falling liquid film. This is realised by setting $\hat{\tau}_{w0}=0$, $\tau_{w1}(k/\nu)=0$ and $P_{w1}(k/\nu)=0$.

In order to confirm the validity of our numerical results, we also perform an asymptotic analysis (Kalliadasis et al., 2012) of the O-S equation along with the boundary conditions. Making use of the long-wave expansions for ϕ and c,

$$\phi = \phi_0 + k\phi_1 + \cdots, \tag{4.29a}$$

$$c = c_0 + kc_1 + \cdots, \tag{4.29b}$$

in equations (4.22), (4.23), (4.25) and (4.26) with A_1 being eliminated, at $\mathcal{O}(1)$, we have

$$\phi_0'''' = 0, \tag{4.30a}$$

$$\phi_0(-1) = 0, \qquad \phi_0'(-1) = 0, \tag{4.30b}$$

$$2(c_0-1)\phi_0''(1) - \phi_0(1) = 0, \tag{4.30c}$$

$$\phi_0'''(1) = 0. \tag{4.30d}$$

The solution to the above system (4.30a), (4.30b), (4.30c) and (4.30d) is found to be

$$\phi = B(z+1)^2, \tag{4.31a}$$

$$c_0 = 2, \tag{4.31b}$$

where B is any arbitrary constant, which we can set to 1 for simplicity.

At $\mathcal{O}(k)$, we have

$$\phi_1'''' = \frac{1}{2}\mathrm{i}Re(z-1), \tag{4.32}$$

subject to

$$\phi_1(-1) = 0 \qquad \phi_1'(-1) = 0, \tag{4.33a}$$

$$4\phi_1'''(1) + \mathrm{i}\left[Re\phi_0'(1) - 2\cot\theta\phi_0''(1)\right] = 0, \tag{4.33b}$$

$$2(1-c_0)\phi_1''(1) + \phi_1(1) = 2c_1\phi_0''(1). \tag{4.33c}$$

The solution at this order is given by

$$\begin{aligned}\phi_1 = \frac{1}{240}\mathrm{i}Rez^5 - \frac{1}{48}\mathrm{i}Rez^4 + \frac{1}{6}\left[-\frac{3}{4}\mathrm{i}Re + \mathrm{i}\cot\theta\right]z^3 + \frac{1}{2}\left[-\frac{41}{120}\mathrm{i}Re + \frac{2}{3}\mathrm{i}\cot\theta + 2\right]z^2 \\ + \left[-\frac{17}{240}\mathrm{i}Re + \frac{1}{6}\mathrm{i}\cot\theta + 2\right]z + 1,\end{aligned} \tag{4.34a}$$

$$c_1 = \mathrm{i}\left(\frac{8}{15}Re - \frac{2}{3}\cot\theta\right). \tag{4.34b}$$

Therefore, the total solution can be written as

$$\begin{aligned}\phi = (z+1)^2 + k\Bigg[\frac{1}{240}\mathrm{i}Rez^5 - \frac{1}{48}\mathrm{i}Rez^4 + \frac{1}{6}\left(-\frac{3}{4}\mathrm{i}Re + \mathrm{i}\cot\theta\right)z^3 \\ + \frac{1}{2}\left(-\frac{41}{120}\mathrm{i}Re + \frac{2}{3}\mathrm{i}\cot\theta + 2\right)z^2 + \left(-\frac{17}{240}\mathrm{i}Re + \frac{1}{6}\mathrm{i}\cot\theta + 2\right)z + 1\Bigg] + \cdots,\end{aligned} \tag{4.35a}$$

$$c = 2 + \mathrm{i}k\left(\frac{8}{15}Re - \frac{2}{3}\cot\theta\right) + \cdots. \tag{4.35b}$$

From equation (4.35b), it can be inferred that the long waves travel at twice the surface velocity of the undisturbed flow. Hence, the expression for growth rate is given by

$$s_r = -\mathrm{Re}(\mathrm{i}kc) \equiv k^2\left(\frac{8}{15}Re - \frac{2}{3}\cot\theta\right). \tag{4.36}$$

The flat film solution becomes unstable when $s_r > 0$, from which we can deduce the critical Reynolds number at which the instability sets in as

$$Re_c = \frac{5}{4}\cot\theta. \tag{4.37}$$

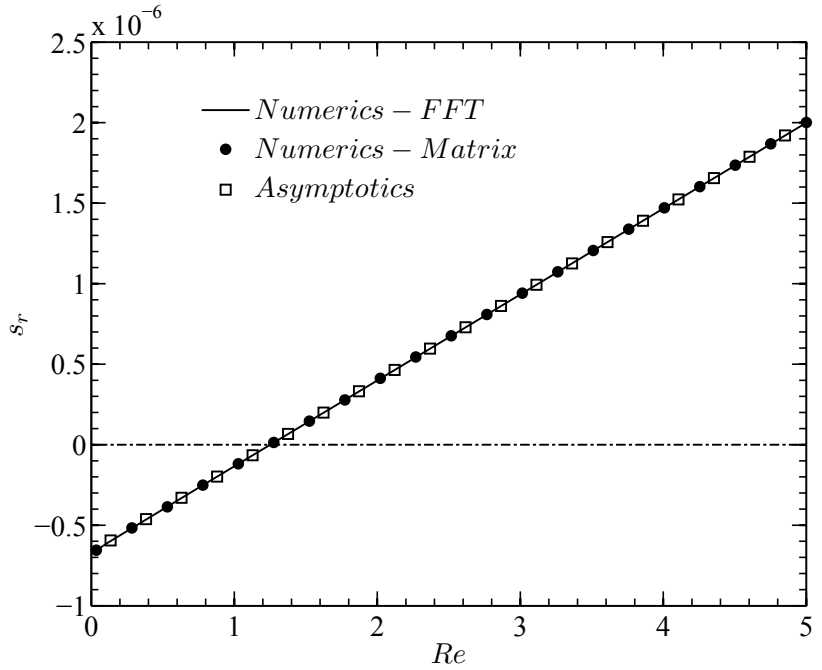

Figure 4.3.: Growth rate vs Re for a falling liquid film, $\Theta = 0$, $\theta = \pi/4$, $k = 0.001$ and $Ka = 1988.5$.

In our analysis, we could have considered terms that are of higher order, but we are only interested to see if our numerics captures the critical behaviour.

Figure 4.3 shows the growth rate of the disturbance (s_r) as a function of Reynolds number (Re), with the wavenumber $k = 0.001$ and $\theta = \pi/4$. Our computation by two different techniques, namely the 'FFT-based' and 'Matrix-based' agrees very well with the asymptotic result. Beyond the critical Reynolds number ($Re_c \equiv 5\cot\theta/4$), the flat film solution becomes unstable and the growth rate increases with increase in Re. As we increase the wavenumber ($k = 0.01$) further, the growth rate increases for any given Re, but the numerics still predicts the critical Reynolds number very well (as shown in figure 4.4).

Figure 4.5 shows the growth rates, corresponding to the most dominant (unstable) normal mode for the case of a vertically falling liquid film ($\theta = \pi/2$), for various Re. As can be observed from the plot, the vertically falling liquid film is unstable to long-wavelength disturbances (for any Re), and the band of unstable wavenumbers increases as Re is increased. As the wavenumber is increased beyond a particular value, the growth rate becomes negative, implying that the short wave disturbances are stabilising.

Another way to analyse the linear stability of the gas-liquid system is to consider the

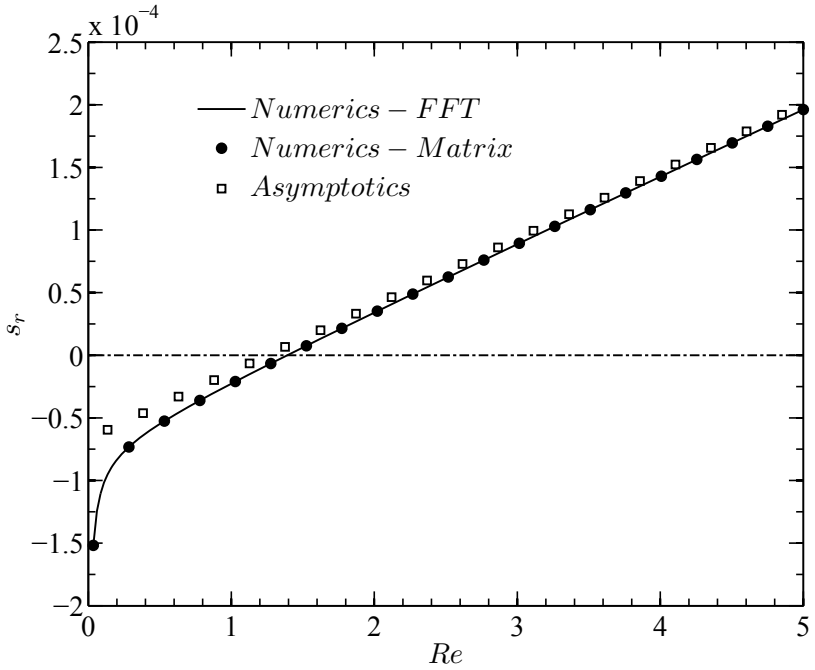

Figure 4.4.: Growth rate vs Re for a falling liquid film, $\Theta = 0$, $\theta = \pi/4$, $k = 0.01$ and $Ka = 1988.5$.

neutral stability curves. In figure 4.6, we have compared the neutral curves computed from our O-S formulation (with the gas flow switched-off) with Kalliadasis et al. (2012) for the parameter values, $Ka = 528.8$ and $\theta = \pi/2$, which shows an excellent agreement.

As a next step, we compare the neutral curves obtained by solving the dispersion relations for the long-wave (4.18) and WIBL models (4.21) with the O-S system for the vertical configuration ($\theta = \pi/2$) and $Ka = 1988.5$. From figure 4.7, it can be observed that the long-wave and WIBL models correctly predict the linear stability threshold for Re up to 10, beyond which the agreement becomes poorer as the inertial effects become important that are not captured by the low-dimensional models.

4.4.3. Case: with gas flow

As the gas flow influences the liquid problem through the nonlocal terms in the tangential and normal stress balances, (4.25), (4.26), analytical progress becomes unfeasible. Therefore, we resort to numerical treatment of the O-S equations and the low-dimensional models. In the experiments of Zapke and Kröger (2000a,b) on flooding in rectangular channels with an emphasis on geometrical effects, helium (g) was used in the gas phase and methanol (ℓ) in the liquid. We adopt the same as our working fluids, the physical

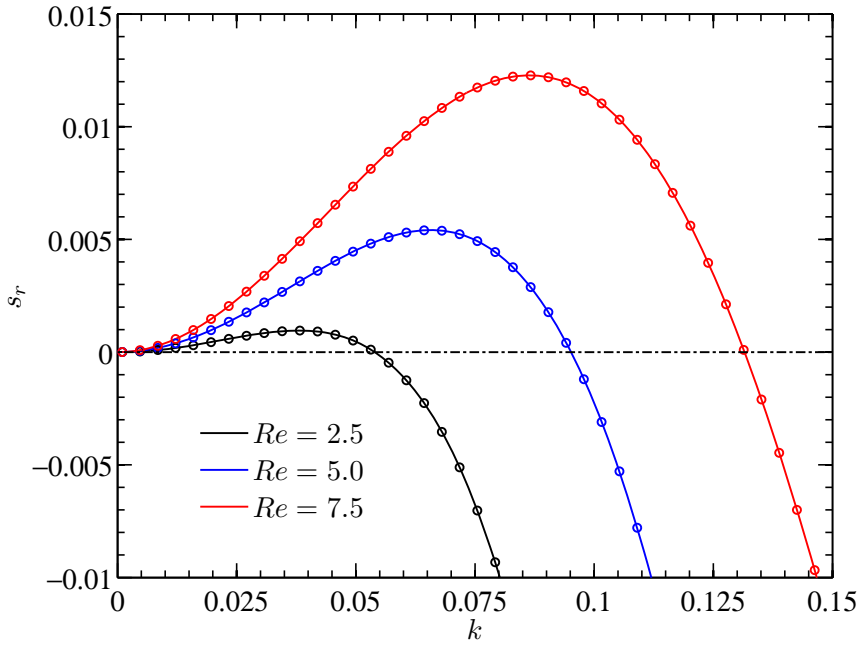

Figure 4.5.: Growth rate vs wavenumber (k) for a falling liquid film, $\Theta = 0$, $\theta = \pi/2$ and $Ka = 1988.5$. Solid curves correspond to solution from 'FFT-based' method, open circles correspond to solution from 'Matrix-based' technique.

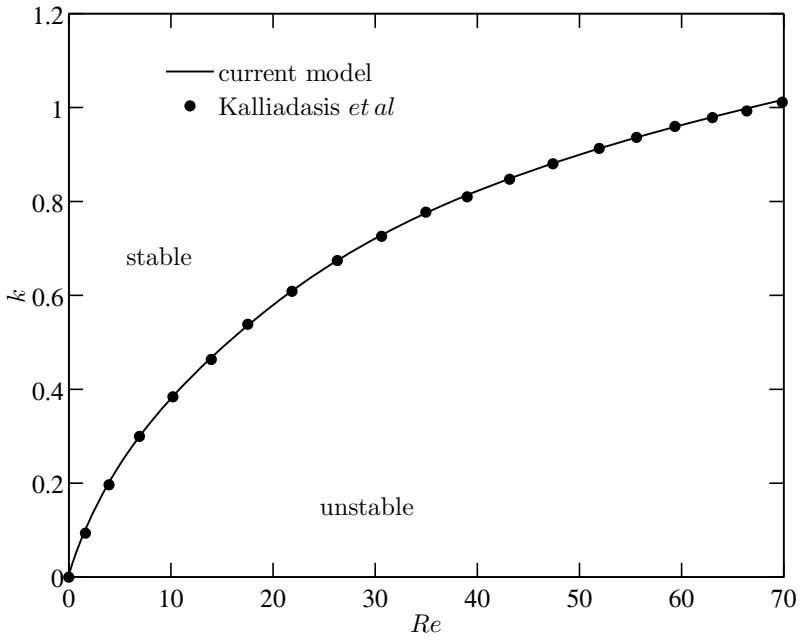

Figure 4.6.: Neutral stability curve for a vertically falling film, $\Theta = 0$, $\theta = \pi/2$ and $Ka = 528.8$; solid curve corresponds to our O-S system, whereas the closed circles correspond to Kalliadasis et al. (2012).

properties of those are as follows:

$$\rho_g = 0.165\,\mathrm{kg/m^3}, \quad \mu_g = 2 \times 10^{-5}\,\mathrm{Pa\ s}, \tag{4.38a}$$

$$\rho_\ell = 791\,\mathrm{kg/m^3}, \quad \mu_\ell = 5.75 \times 10^{-4}\,\mathrm{Pa\ s}, \quad \sigma = 22 \times 10^{-3}\,\mathrm{N/m}, \tag{4.38b}$$

which in terms of dimensionless numbers in our formulation are given by

$$Ka = 1988.5, \quad N = 0.4. \tag{4.39}$$

First, we present the neutral curves of the long-wave model (figure 4.8), WIBL model (figure 4.9) and the O-S equation (figure 4.10). We can observe that the stability boundaries obtained from the long-wave and WIBL models are marginally different from the O-S equations. The region of stability increases with increasing the gas shear, but beyond a particular value of Θ, the stability boundary changes location (figure 4.10). This difference in the region of stability could be partly attributed to the pressure terms in the normal stress balance coming from the gas flow.

In order to make a better comparison between the various models, we plot the stability

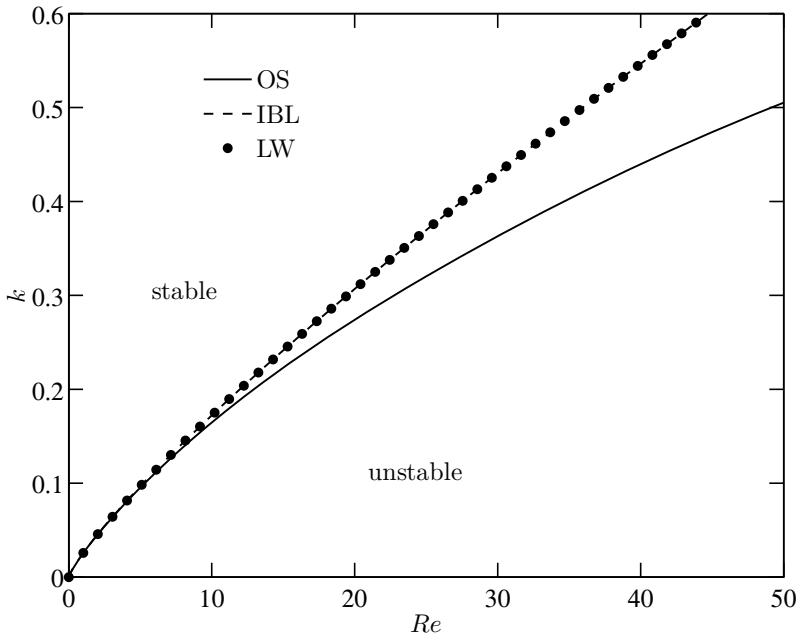

Figure 4.7.: Neutral stability curve for a vertically falling film, $\Theta = 0$, $\theta = \pi/2$ and $Ka = 1988.5$; solid curve corresponds to O-S, closed circles correspond to long-wave model, and dashed curve corresponds to WIBL model.

boundary on k–Θ plane for two different values of Re. It can be seen from figure 4.11 that both the long-wave and WIBL models show good agreement with O-S for $Re = 5$, but as the Reynolds number is increased to $Re = 18$, the WIBL model shows an overall better agreement than the long-wave model.

4.5. Absolute/Convective instability

4.5.1. Methodology

In this section, we provide an outline of the methodology to analyse absolute and convective instabilities which is based on Fokas and Papageorgiou (2005), by considering the dispersion relation obtained from the long-wave model. To begin, let us assume that $f(x, 0) = f_0(x)$ is the given initial condition. Therefore, the solution of the linearised equation can be written as

$$f(x, t) = \frac{1}{2\pi} \int_{-\infty}^{\infty} \mathrm{e}^{s(k)t + \mathrm{i}kx} \hat{f}_0(k)\, \mathrm{d}k, \tag{4.40}$$

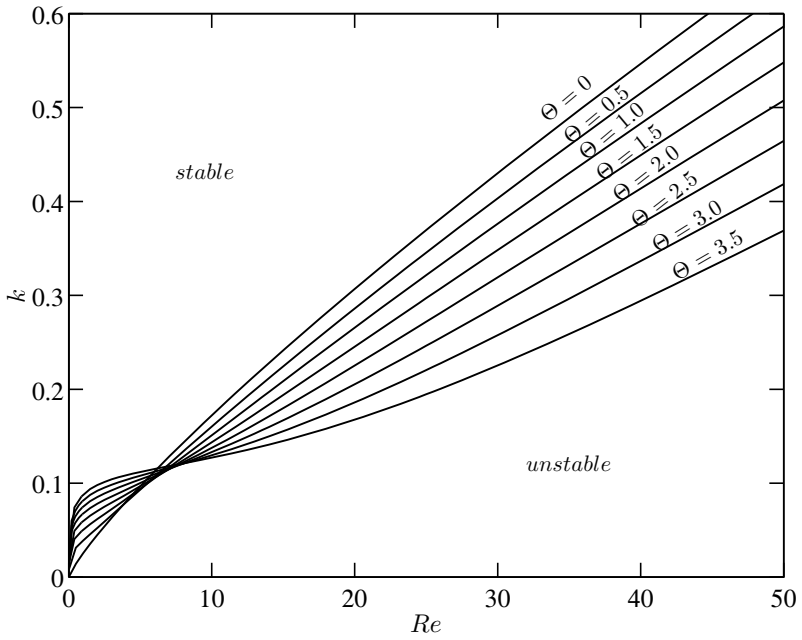

Figure 4.8.: Neutral stability curves from the long-wave model for a vertically falling film in contact with counter-current gas flow for various values of gas shear Θ, $\theta = \pi/2$, $Ka = 1988.5$ and $N = 0.4$.

where $\hat{f}_0(k)$ is the Fourier transform of the initial condition:

$$\hat{f}_0(k) = \int_{-\infty}^{\infty} \mathrm{e}^{-\mathrm{i}kx} f_0(x)\,\mathrm{d}x. \tag{4.41}$$

There are two possibilities: If $\mathrm{Re}[s(k)] \leq 0$ for all k, the flat-film solution is linearly stable. On the other hand if $\mathrm{Re}[s(k)] > 0$ at least for some k, then the flat-film solution is unstable, and the instability could be either absolute or convective. Noting that $\tau_{w1}(-\alpha) = \overline{\tau_{w1}(\alpha)}$ for real α, where the bar denotes complex conjugation, the growth rate can be written as

$$s(k) = \begin{cases} -\mathrm{i}ak + bk^2 - ck^4 - \mathrm{i}dk\,\overline{\tau_{w1}(k/\nu)} \equiv s_-(k), & \text{if } k < 0, \\ -\mathrm{i}ak + bk^2 - ck^4 - \mathrm{i}dk\,\tau_{w1}(k/\nu) \equiv s_+(k), & \text{if } k \geq 0. \end{cases} \tag{4.42}$$

The growth rates are related by $s_-(-k) = \overline{s_+(k)}$. As a next step, we denote the real part of the growth rate as $s_r(k) \equiv \mathrm{Re}[s_+(k)] = bk^2 - ck^4 + dk\,\mathrm{Im}[\tau_{w1}(k/\nu)]$. The integral (4.40) can be rewritten as

$$f(x,\,t) = \frac{1}{2\pi}[I(x,\,t) + J(x,\,t)], \tag{4.43}$$

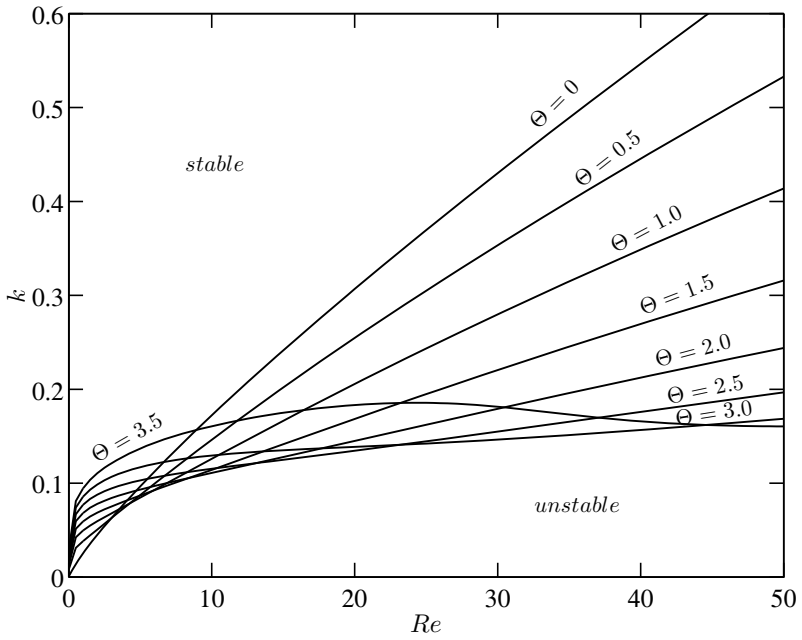

Figure 4.9.: Neutral stability curves from the WIBL model for a vertically falling film in contact with counter-current gas flow for various values of gas shear Θ, $\theta = \pi/2$, $Ka = 1988.5$ and $N = 0.4$.

where

$$I(x,\,t) = \left(\int_{-\infty}^{-k_1} + \int_{k_1}^{\infty}\right) \mathrm{e}^{s(k)t+\mathrm{i}kx}\,\hat{f}_0(k)\,\mathrm{d}k \tag{4.44}$$

and

$$J(x,\,t) = \left(\int_{-k_1}^{0} + \int_{0}^{k_1}\right) \mathrm{e}^{s(k)t+\mathrm{i}kx}\,\hat{f}_0(k)\,\mathrm{d}k, \tag{4.45}$$

with k_1 being the critical wavenumber below which the flat film solution is unstable. It can be easily shown that for a fixed x/t, the long-time behaviour of $I(x,\,t)$ decays to zero. Now, we shall analyse the other integral, $J(x,\,t)$:

$$J(x,\,t) = \int_{-k_1}^{0} \mathrm{e}^{s_-(k)t+\mathrm{i}kx}\,\hat{f}_0(k)\,\mathrm{d}k + \int_{0}^{k_1} \mathrm{e}^{s_+(k)t+\mathrm{i}kx}\,\hat{f}_0(k)\,\mathrm{d}k \tag{4.46}$$

$$= \int_{0}^{k_1} \mathrm{e}^{s_-(-k)t-\mathrm{i}kx}\,\hat{f}_0(-k)\,\mathrm{d}k + \int_{0}^{k_1} \mathrm{e}^{s_+(k)t+\mathrm{i}kx}\,\hat{f}_0(k)\,\mathrm{d}k. \tag{4.47}$$

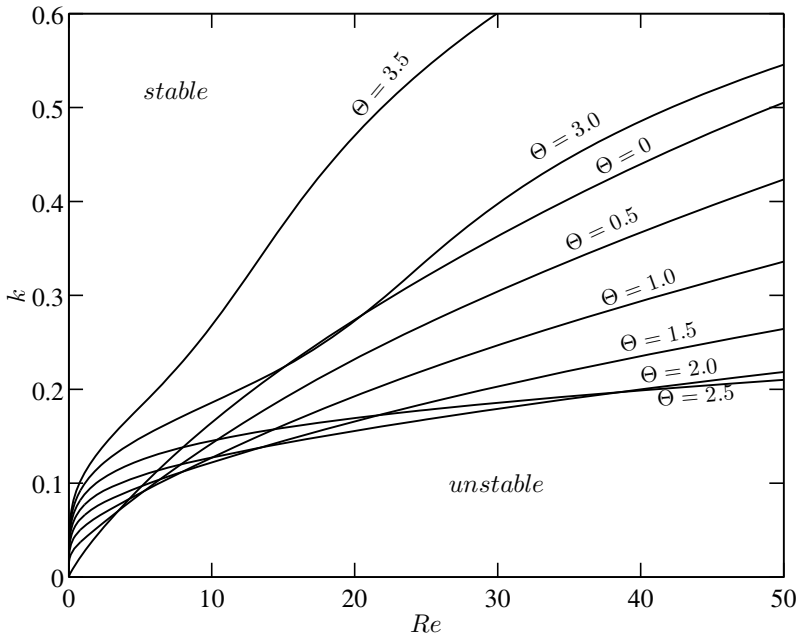

Figure 4.10.: Neutral stability curves from the O-S equations for a vertically falling film in contact with counter-current gas flow for various values of gas shear Θ, $\theta = \pi/2$, $Ka = 1988.5$ and $N = 0.4$.

By making use of the fact that $s_-(-k) = \overline{s_+(k)}$ for real k, and that $\hat{f}_0(-k) = \overline{\hat{f}_0(k)}$ as $f_0(x)$ is a real function, we obtain

$$J(x,\,t) = \int_0^{k_1} \left[\mathrm{e}^{\overline{s_+(k)}t - \mathrm{i}kx}\, \overline{\hat{f}_0(k)} + \mathrm{e}^{s_+(k)t + \mathrm{i}kx}\, \hat{f}_0(k) \right] \mathrm{d}k \tag{4.48}$$

$$= \int_0^{k_1} \left[\overline{\mathrm{e}^{s_+(k)t + \mathrm{i}kx}\, \hat{f}_0(k)} + \mathrm{e}^{s_+(k)t + \mathrm{i}kx}\, \hat{f}_0(k) \right] \mathrm{d}k \tag{4.49}$$

$$= 2\mathrm{Re}\left[K(x,\,t)\right], \tag{4.50}$$

where

$$K(x,\,t) = \int_0^{k_1} \mathrm{e}^{s_+(k)t + \mathrm{i}kx}\, \hat{f}_0(k)\, \mathrm{d}k. \tag{4.51}$$

The functions $s_+(k)$ has been defined for real non-negative values of k, since $\tau_{w1}(\alpha)$ is obtained by solving the equation (3.13) with homogeneous boundary conditions (3.14) and (3.15) for positive values of α. But the coefficients in equation (3.13) are analytic functions of α. Therefore, we can obtain an analytic continuation of $\tau_{w1}(\alpha)$ from the non-negative real semi-axis to the whole complex plane by simply solving (3.13) with homogeneous

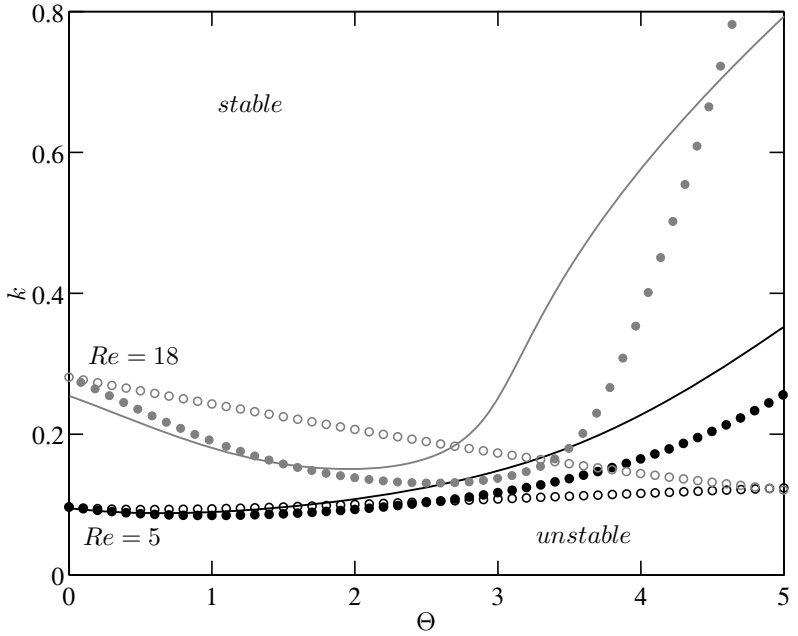

Figure 4.11.: Neutral stability curves: solid curves corresponds to O-S, open circles correspond to long-wave model and closed circles correspond to WIBL model. Black shading and grey shading correspond to $Re = 5$ and $Re = 18$ respectively, with $\theta = \pi/2$, $Ka = 1988.5$ and $N = 0.4$.

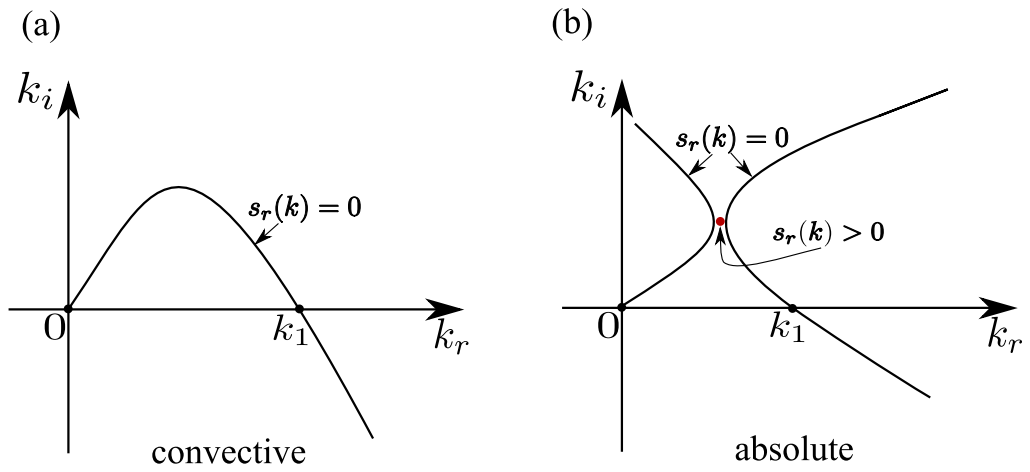

Figure 4.12.: Schematic representation of (a) convective and (b) absolute instabilities on the complex wavenumber plane.

boundary conditions (3.14) and (3.15) when α is an arbitrary complex number.

Now, having obtained $\tau_{w1}(\alpha)$ for complex values of α, the analysis of $K(x, t)$ depends on the topology of the curves $s_r(k) = 0$ in the complex k-plane, where $s_r(k)$ denotes the real part of $s_+(k)$. There are two possibilities:

Case I: There is a part of the curve $s_r(k) = 0$ that connects the origin $(0, 0)$ and $(k_1, 0)$ in the $k_r k_i$-plane, with k_r and k_i denoting the real and the imaginary parts of k, respectively. In addition, if $\hat{f}_0(k)$ can be analytically continued off the real axis so that $\hat{f}_0(k)$ is analytic in a neighbourhood of the curve $s_r(k) = 0$ connecting the points $(0, 0)$ and $(k_1, 0)$ as shown in figure 4.12(a) (this is the case, for example, when $f_0(x)$ has a sufficiently fast exponential decay as $|x| \to \infty$). The integration contour for $K(x, t)$ can then be deformed to follow that part of the curve $s_r(k) = 0$ which connects $(0, 0)$ to $(k_1, 0)$. The Riemann–Lebesgue lemma then implies that for a fixed x, $K(x, t) \to 0$ as $t \to \infty$, and we have *convective instability*.

Case II: The other possibility is that it is impossible to connect the origin with $(k_1, 0)$ using the part of the curve $s_r(k) = 0$ in the $k_r k_i$-plane. In such a scenario, there must exist a saddle point (also called the pinch point) of $s_+(k)$, at which $s_r(k)$ is positive (see figure 4.12(b)), so that the integration contour can be deformed into a steepest descent path passing through this saddle point. Here $K(x, t)$ is seen to grow for a fixed x as $t \to \infty$ (Hinch, 1991), and the type of instability in this case is *absolute*. We also note here that the saddle point corresponds to the mode with zero group velocity.

4.5.2. Results

Before presenting the results on absolute and convective instabilities, we provide an outline of the numerical scheme implemented for the case of O-S. We split the matrices $\mathbf{A}$ and $\mathbf{B}$, and the eigenvector $\mathbf{w}$ into their real and imaginary parts as

$$\mathbf{A} = \mathbf{A}_r + \mathrm{i}\mathbf{A}_i, \qquad \mathbf{B} = \mathbf{B}_r + \mathrm{i}\mathbf{B}_i, \qquad \mathbf{w} = \mathbf{w}_r + \mathrm{i}\mathbf{w}_i. \tag{4.52}$$

Now, the matrix eigenvalue problem can be written in terms of two real equations, for any given Re and Θ:

$$\mathbf{A}_r(k_r, k_i)\mathbf{w}_r - \mathbf{A}_i(k_r, k_i)\mathbf{w}_i = c_r \left[\mathbf{B}_r(k_r, k_i)\mathbf{w}_r - \mathbf{B}_i(k_r, k_i)\mathbf{w}_i\right], \tag{4.53a}$$

$$\mathbf{A}_r(k_r, k_i)\mathbf{w}_i + \mathbf{A}_i(k_r, k_i)\mathbf{w}_r = c_r \left[\mathbf{A}_r(k_r, k_i)\mathbf{w}_i + \mathbf{A}_i(k_r, k_i)\mathbf{w}_r\right], \tag{4.53b}$$

$$k_r c_i + k_i c_r = 0. \tag{4.53c}$$

The last equation (4.53c) comes from the requirement that the real part of the growth rate is zero, i.e. $s_r(k_r, k_i) = 0$. So far, we have $2M + 3$ equations for $2M + 6$ unknowns in $k_r, k_i, \mathbf{w}_r, \mathbf{w}_i, c_r$ and c_i. By making the eigenvector $\mathbf{w}$ unique, i.e., by fixing the magnitude and the angle, respectively, we can write

$$\mathbf{w}_r^T \mathbf{w}_r + \mathbf{w}_i^T \mathbf{w}_i = 1, \qquad \mathbf{w}_r^T \mathbf{w}_i = 0. \tag{4.54}$$

Finally, we look for solutions at a small distance ε_k from the previous point (k_{r_0}, k_{i_0}) on the curve $s_r(k_r, k_i) = 0$. Therefore, we can write

$$(k_r - k_{r_0})^2 + (k_i - k_{i_0})^2 = \varepsilon_k^2. \tag{4.55}$$

The above set of nonlinear equations can be conveniently solved using Newton's method, given an initial solution on $s_r(k_r, k_i) = 0$, which can be obtained by setting k_i=0. The typical value of ε_k considered is $\sim 10^{-3}$.

We begin by presenting in figure 4.13 the curves $s_r(k) = 0$ in the (k_r, k_i) plane for various values of gas shear, Θ for $Re = 5$, corresponding to the dispersion relation (4.18) obtained from the long-wave model. It can be observed from figure 4.13 that for very small values of Θ, the origin is connected to $(k_r, 0)$ by the curve $s_r(k) = 0$. This implies that the long-time behaviour of the integral (4.51) vanishes, therefore, we have convective instability. This is only to be expected, as any localised disturbance introduced on the system is convected downstream, i.e. along '$+x$'. The situation is similar for large values of

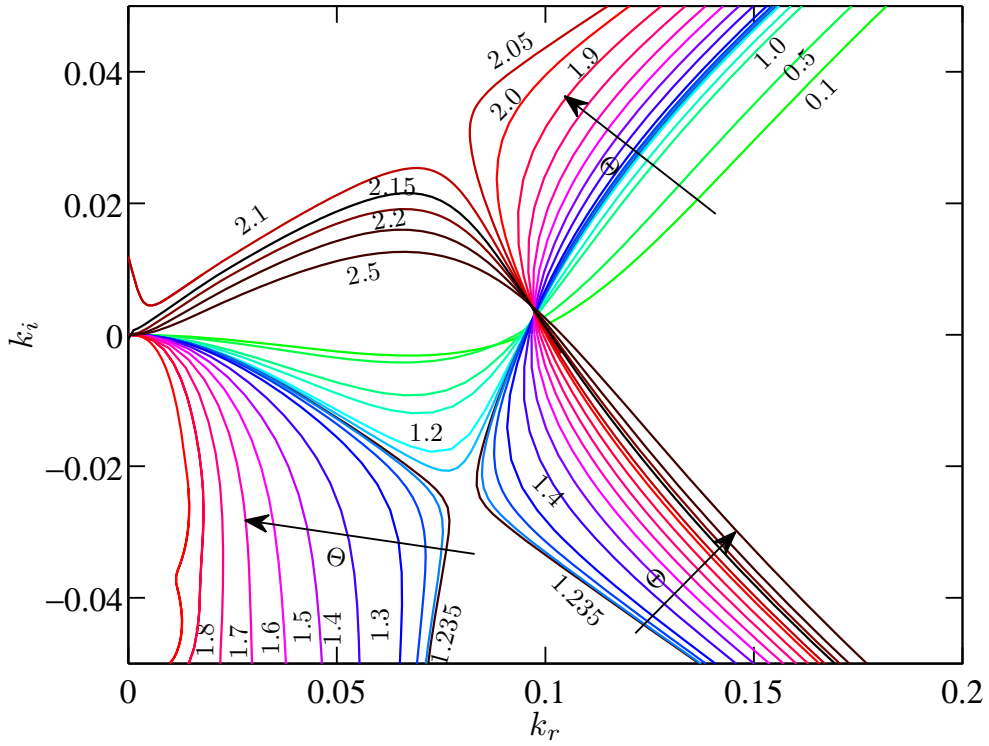

Figure 4.13.: Curves of $s_r(k) = 0$ on the complex wavenumber plane (k_r, k_i) from the long-wave model for various values of gas shear, Θ, with $Re = 5$, $\theta = \pi/2$, $Ka = 1988.5$ and $N = 0.4$.

Θ, but the disturbance is convected along '$-x$' as the waves start traveling in the upward direction because of the increase in the strength of gas flow when compared to that of the liquid. But there exist a band of gas flow rates ($1.235 \leq \Theta \leq 2.1$) for which the origin is not connected to $(k_r, 0)$ by $s_r(k) = 0$, but there exist a saddle point at which $s_r(k) > 0$ and the instability could be absolute.

Figure 4.14 shows the curves $s_r(k) = 0$ corresponding to the quadratic dispersion relation (4.21) obtained from the WIBL model. Note that for the WIBL model there exist two branches, $s_{r1}(k)$ and $s_{r2}(k)$. However, for the parameter space under consideration, only for one of these branches there exists a band of unstable wave numbers. We denote this branch by $s_r(k)$. The results obtained using the WIBL model are similar to those obtained from the long-wave model with only minor differences.

Finally, we present the curves $s_r(k) = 0$, on the (k_r, k_i) plane corresponding to the most dominant mode in the O-S equations (see figure 4.15), which also turns out to be the

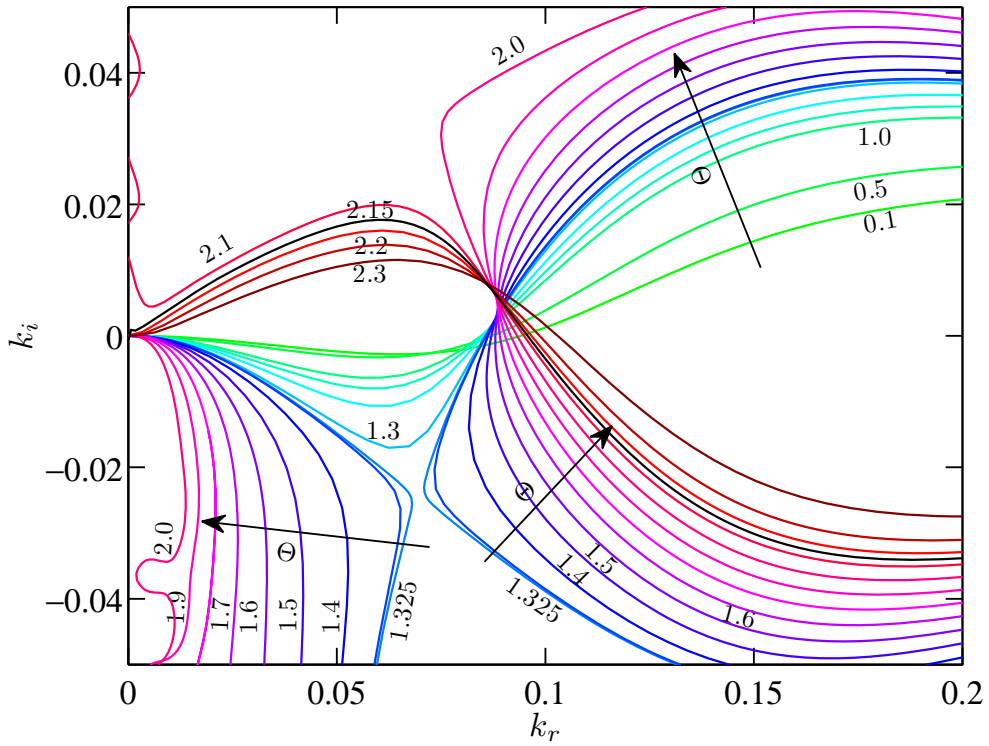

Figure 4.14.: Curves of $s_r(k) = 0$ on the complex wavenumber plane (k_r, k_i) from the WIBL model for various values of gas shear, Θ, with $Re = 5$, $\theta = \pi/2$, $Ka = 1988.5$ and $N = 0.4$.

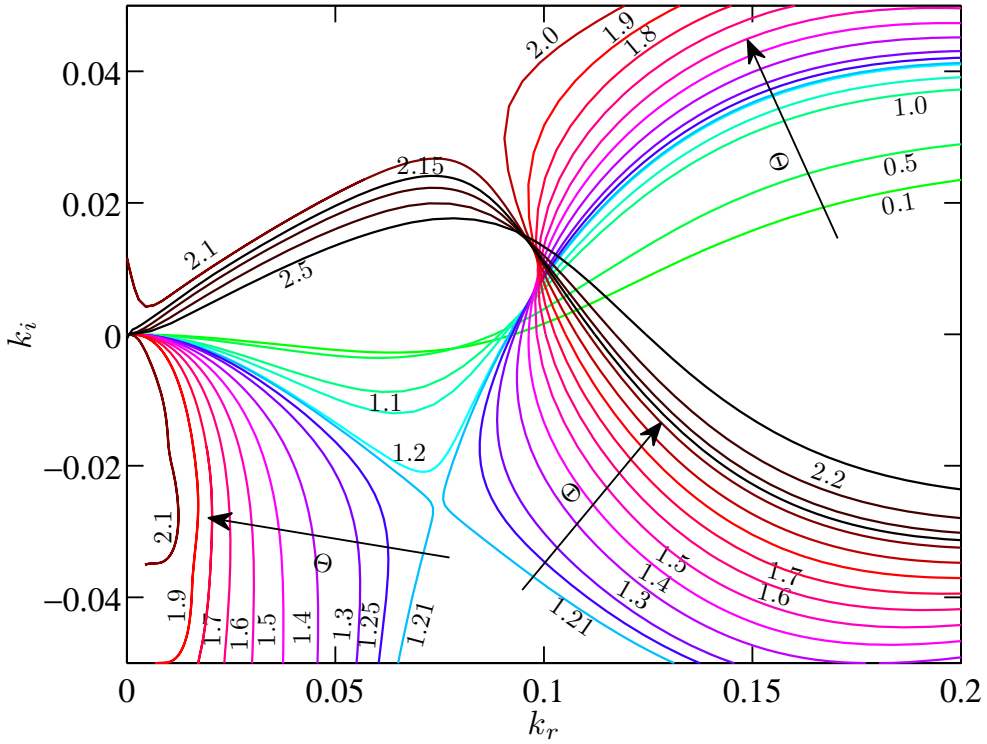

Figure 4.15.: Curves of $s_r(k) = 0$ on the complex wavenumber plane (k_r, k_i) by solving the O-S equation for various values of gas shear, Θ, with $Re = 5$, $\theta = \pi/2$, $Ka = 1988.5$ and $N = 0.4$.

only unstable mode for the parameter values considered. The results are again similar to that presented earlier with the long-wave and WIBL models, with the region of absolute instability predicted to be $1.21 \leq \Theta \leq 2.1$. This is not very surprising as the liquid flow rate that we have considered is sufficiently small for the low-dimensional models to have good agreement with the O-S (see also figure 4.11, from the temporal analysis). Moreover, we find that the WIBL model has a better quantitative agreement with the OS equations than the long-wave model, in the flow regime considered.

We note in addition, the non-linear computations of the WIBL model of Tseluiko and Kalliadasis (2011) reveal that the flooding point (defined as the point at which there appear large-amplitude nearly stationary waves) is close to $\Theta \sim 2.5$. Interestingly, this flooding point is also close to the upper limit of the absolute instability regime ($\Theta \sim 2.1$) predicted by our analysis.

4.6. Time-dependent computation

In order to supplement the absolute and convective instability regimes predicted by our linear analysis in section 4.5, we solve the linearised WIBL model ((4.19)–(4.20)) as an initial-value problem subject to a localised initial condition. This is carried out numerically using a scheme which is based on a Fourier pseudo-spectral representation of the derivatives along the spatial direction and an adaptive stepping along time. We choose the initial condition of the interface disturbance, $f(x,t)$ to be localised about $x = 0$, defined by the gaussian function, $f(x,0) = 0.1\exp(-0.5x^2)$ and $g(x,0) = 0$. The liquid Reynolds number is taken to be $Re = 5$, consistent with that in the previous section. The equations are integrated on a long periodic domain $[-750, 750]$ for sufficiently long time, say $t \approx 500$ to determine the evolution of the wave packets.

We begin with a relatively small value of the gas shear, $\Theta = 1.0$, and the corresponding evolution of the disturbance is depicted as a space-time plot in figure 4.16a. It can be observed that the wave packet starts propagating downstream along the positive x-direction, therefore the instability is convective. On the other side of the gas flow spectrum, i.e., for $\Theta = 2.2$ the instability is again convective with the wave packet propagating upstream along the negative x-direction (figure 4.16b). This can further be confirmed by examining the wave profile at a sufficiently long time instant and the time evolution of the disturbance, $f(x,t)$ at $x = 0$. From figure 4.17, it can be ascertained that the wave profiles for $\Theta = 1.0$ and $\Theta = 2.2$ are entirely in $+x$ and $-x$ respectively, and also the disturbance, $f(0,t)$ eventually decays to zero. Therefore, for $0 \leq \Theta < 1.45$ and $\Theta > 1.85$ the flow system is convectively unstable. For intermediate values of gas flow rates, for e.g., $\Theta = 1.5$ and $\Theta = 1.65$ shown in figure 4.18, the wave packet invades both the negative and positive x-directions, and for further long times they are expected to contaminate the whole domain. This can also be established from figure 4.19, where the disturbance $f(0,t)$ after initial transients grows exponentially. From further numerical simulations, we found that for $1.45 \leq \Theta \leq 1.85$ the gas-liquid system exhibits absolute instability. These results are in good agreement with the band of gas flow rates, $1.2 \leq \Theta \leq 2.0$ predicted by our analysis of various models in section 4.5.

4.7. Conclusion

We have analysed absolute and convective instabilities in a gas-liquid system, where the liquid film is considered to be laminar and the countercurrent gas flow is turbulent. From the full governing equations and boundary conditions, we formulated Orr–Sommerfeld system

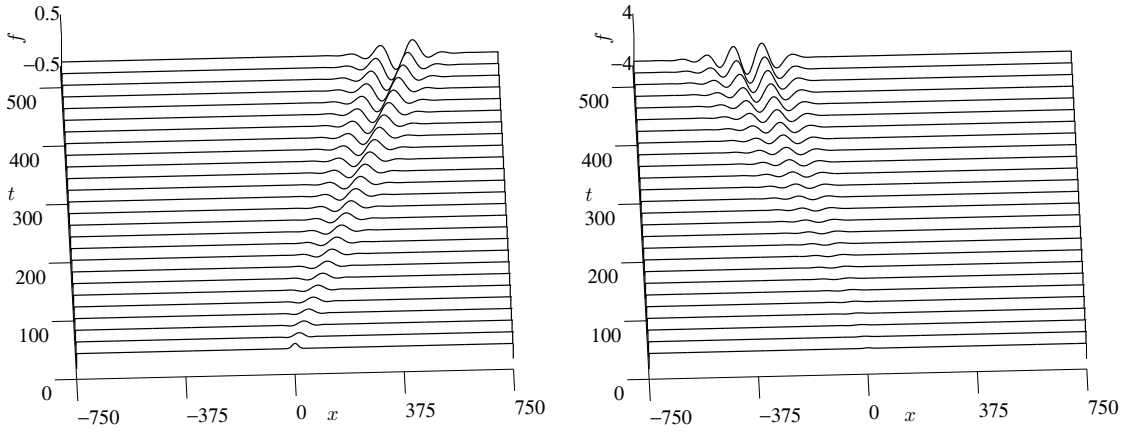

(a) $\Theta = 1.0$ (b) $\Theta = 2.2$

Figure 4.16.: Time-dependent computation of the linearised WIBL model subject to a localised disturbance, showing convective instability for (a) $\Theta = 1.0$ and (b) $\Theta = 2.2$ with $Re = 5$, $\theta = \pi/2$, $Ka = 1988.5$ and $N = 0.4$.

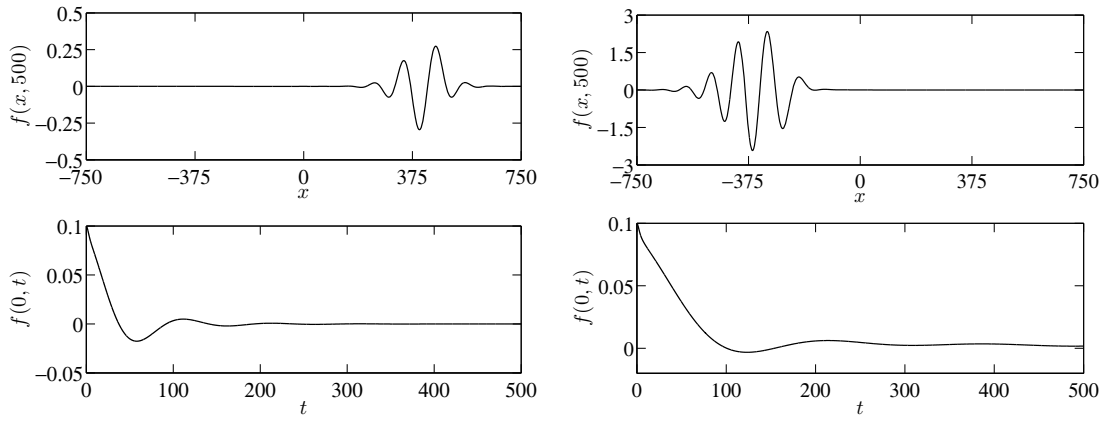

(a) $\Theta = 1.0$ (b) $\Theta = 2.2$

Figure 4.17.: Time-dependent computations of the linearised WIBL model depicting wave profiles at $t = 500$ and time evolution of the disturbance at $x = 0$ for (a) $\Theta = 1.0$ and (b) $\Theta = 2.2$ with $Re = 5$, $\theta = \pi/2$, $Ka = 1988.5$ and $N = 0.4$.

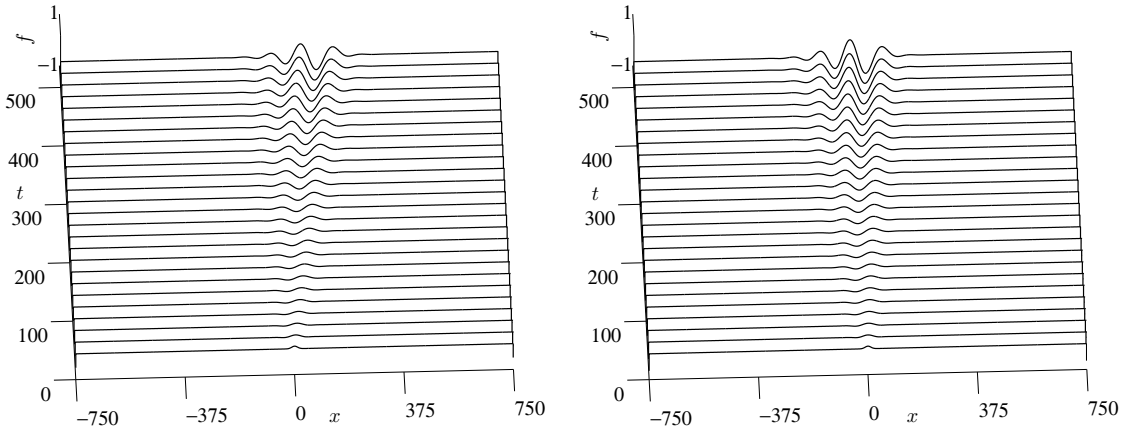

(a) $\Theta = 1.5$ (b) $\Theta = 1.65$

Figure 4.18.: Time-dependent computation of the linearised WIBL model subject to a localised disturbance, showing absolute instability for (a) $\Theta = 1.5$ and (b) $\Theta = 1.65$ with $Re = 5$, $\theta = \pi/2$, $Ka = 1988.5$ and $N = 0.4$.

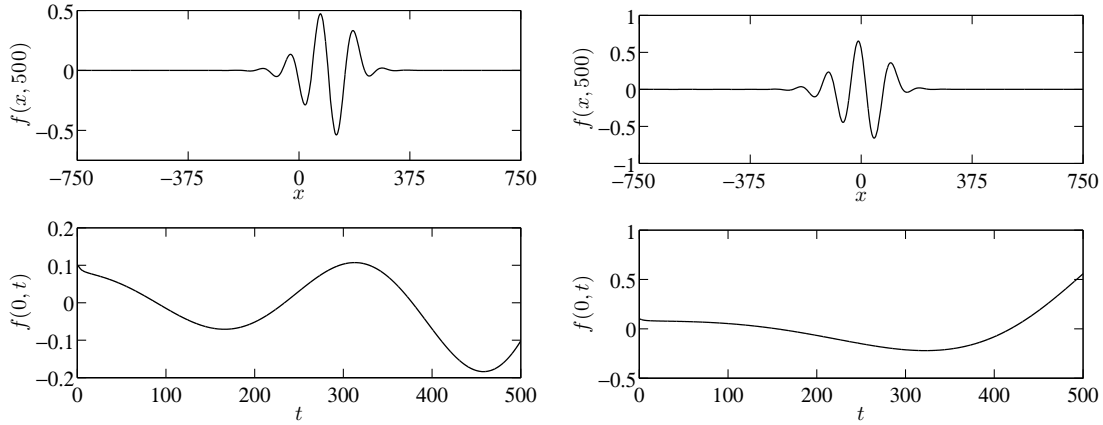

(a) $\Theta = 1.5$ (b) $\Theta = 1.65$

Figure 4.19.: Time-dependent computations of the linearised WIBL model depicting wave profiles at $t = 500$ and time evolution of the disturbance at $x = 0$ for (a) $\Theta = 1.5$ and (b) $\Theta = 1.65$ with $Re = 5$, $\theta = \pi/2$, $Ka = 1988.5$ and $N = 0.4$.

of equations, that could be applied for all values of Reynolds numbers and wavenumbers. We developed a generalised methodology to scrutinise absolute and convective instabilities in a flow system by analysing the nature of growth rate curves on a complex wavenumber plane. By applying this methodology to O-S equation, and the low-dimensional models, namely the long-wave and WIBL models developed by Tseluiko and Kalliadasis (2011), we obtained the flow conditions for which the system exhibits these instabilities. More precisely, we found that for a fixed liquid Reynolds number, at low and high gas flow rates, the system is convectively unstable, and for a range of intermediate gas flow rates we have absolute instability. Further, we supplemented our analysis by doing time-dependent computations of the linearised WIBL model subject to a localised initial condition, which showed that the band of gas flow rates calculated to show absolute and convective instabilities are in good agreement with our analysis. It is interesting to note that the upper limit of the absolute instability regime is close to the flooding point obtained from the fully non-linear computations of the WIBL model of Tseluiko and Kalliadasis (2011). We can therefore conclude that the linear analysis presented above can be used for predicting the flooding point.

5. Conclusions

The evolution of interfaces has been analysed under two different situations, namely in the bounded setting of spreading of droplets on chemically heterogeneous substrates, and in the unbounded setting of a down-flowing thin liquid film in the presence of co-current/countercurrent gas flow. For a more detailed overview of the individual problems considered, the reader is referred to the concluding sections of chapters 2, 3 and 4. In this chapter, we provide a brief summary of the conclusions and plausible future directions.

5.1. Droplets on chemically heterogeneous substrates

In Chapter 2, we considered a partially wetting liquid spreading on a solid substrate that was perfectly flat but chemically inhomogeneous. The chemical nature of the substrate was incorporated into the spreading dynamics through a spatially varying microscopic contact angle boundary condition, and a slip condition was prescribed to allow contact line motion. In the limit of slow spreading, by the method of matched asymptotic expansions, the original nonlinear free boundary problem was simplified to a set of coupled ordinary differential equations for the evolution of the contact points. Even though a comparison of the solution to the simplified equations obtained by matching with the original partial differential equation showed excellent agreement, they also lead to completely different behaviours when the initial condition was chosen close to the unstable manifold.

Interestingly, the introduction of heterogeneity in the substrate leads to multiple equilibrium droplet configurations, and these are significantly influenced by the initial location of the contact points and the nature of chemical heterogeneity. Such equilibria were readily extracted by doing a phase plane analysis of the ordinary differential equations obtained by matching. The presence of heterogeneities naturally leads to hysteresis-like effect. In addition, when the heterogeneity is localised and the strength exceeds a critical value, the droplet was shown to get trapped between these heterogeneities, which is also dependent on the initial location of the contact points. A particular class of periodic heterogeneous substrates demonstrated stick-slip motion of the contact line, whereas a substrate with a favourable wettability gradient resulted in a unidirectional motion of the droplet.

In this study, the heterogeneity was considered to be deterministic. However, randomness in heterogeneity is more common (Savva et al., 2010), and this analysis could naturally be extended to examine spreading on such substrates. Another plausible extension of the current work would be to investigate spreading on heterogeneous substrates in the presence of gas flow. Shear-driven droplets are widely observed in nature and industrial settings such as droplet motion in wind shields and spin coating. As an exploratory study, we considered the influence of a gas jet on the spreading dynamics (see Appendix D) by assuming a simple model for the gas flow, i.e., a quadratic pressure distribution. Though the system revealed interesting features such as the formation of dimples at the droplet free surface, the model in its present form is linearly unstable. A possible approach that could be undertaken in the future to cure this shortcoming would be to have a better model for an arbitrary configuration of gas flow. When an inviscid potential flow is assumed for the gas phase, it would be impossible to displace the droplet from the existing configuration as a consequence of d'Alembert's paradox. Therefore, viscous corrections in the gas phase close to the droplet free surface have to be taken into account.

5.2. Thin liquid film in the presence of a co-current gas flow

The dynamics of a thin liquid film in the presence of a co-current turbulent gas stream in an inclined channel was described in Chapter 3. The liquid film was driven by gravity and gas shear, both acting along the liquid flow direction. The gas and liquid problems were solved separately by combining a number of reasonable assumptions with the fact of a negligible viscosity ratio between the gas and the liquid, as in Tseluiko and Kalliadasis (2011). The interfacial shear stress computed by solving the gas problem influences the liquid problem through the boundary conditions at the interface. A weighted integral-boundary-layer (WIBL) model was developed to describe the liquid layer dynamics, where the influence of gas flow enters the liquid problem through a nonlocal term. A linear stability analysis of the flat film solution showed that the presence of gas flow leads to destabilisation of the flat interface.

The WIBL model was utilised to mainly analyse two types of solution that the system exhibits, namely a solitary-wave solution and a travelling-wave solution. The interface thickness in the far field was fixed to a constant value for the solitary-wave, whereas the volume of liquid inside a travelling-wave was considered constant. These solutions were computed for a helium-methanol flow system in a vertical channel using a pseudo-arclength continuation algorithm. It was found that both the wave velocity and amplitude increase with increase in liquid Reynolds number as well as gas shear, which was different

in a counter-current setting. Our time-dependent computations of the WIBL model on a periodic domain showed good agreement with the continuation results.

Especially at high gas shear rates and liquid Reynolds numbers, the results of our numerical continuation revealed turning points in the wave velocity. As the turning points continued to exist even for sufficiently long domains, this could also be due to a limitation of the current model. A potential future work in this direction would be to appropriately regularise the highest nonlinearity in the existing model, and also to develop a more sophisticated model that includes effects such as viscous dispersion.

5.3. Stability of a liquid film in the presence of countercurrent gas flow

Absolute and convective instabilities of a thin liquid film in contact with a countercurrent gas flow was examined in Chapter 4. In order to understand the stability of this gas-liquid system, we began by deriving the Orr–Sommerfeld equation from the full Navier-Stokes equations and associated boundary conditions. The temporal stability problem was analysed by solving the Orr–Sommerfeld equation numerically as an eigenvalue problem, and the neutral curves were computed using a continuation scheme. A generalised methodology was developed to investigate absolute and convective instabilities by analysing the growth rate curves on a complex wavenumber plane. By applying this formalism to the Orr–Sommerfeld equation and the long-wave and WIBL models developed by Tseluiko and Kalliadasis (2011), the regimes of absolute and convective instabilities were obtained. For a fixed liquid Reynolds number, it was found that convective instability exists for low and high gas flow rates, where the disturbance gets convected upstream and downstream with respect to the initial liquid flow direction. On the other hand, for intermediate gas flow rates, absolute instability prevails with the disturbance contaminating the whole domain. Comparisons were made with time-dependent computations of the linearised WIBL model subject to a localised initial condition, which showed good agreement with our analysis. The upper limit of the absolute instability regime was found to be close to the flooding point obtained from the time-dependent computations of the WIBL model of Tseluiko and Kalliadasis (2011).

The current framework for the liquid film in the presence of gas flow could also be explored to consider gas-driven droplet motion by taking into account the disjoining pressure effects necessary to analyse a wetting phenomena.

Bibliography

S. Alekseenko, V. Antipin, A. Cherdantsev, S. Kharlamov, and D. Markovich. Two-wave structure of liquid film and wave interrelation in annular gas-liquid flow with and without entrainment. *Phys. Fluids*, 21:061701, 2009.

S. V. Alekseenko, V. E. Nakoriakov, and B. G. Pokusaev. *Wave Flow of Liquid Films*. Begell House, New York, 1994.

A. J. Archer. Dynamical density functional theory for molecular and colloidal fluids: A microscopic approach to fluid mechanics. *J. Chem. Phys.*, 130:014509, 2009.

R. W. Atherton and G. M. Homsy. On the derivation of evolution equations for interfacial waves. *Chem. Engng Comm.*, 2:57–77, 1976.

N. J. Balmforth. Solitary waves and homoclinic orbits. *Annu. Rev. Fluid Mech.*, 27: 335–373, 1995.

T. B. Benjamin. Wave formation in laminar flow down an inclined plane. *J. Fluid Mech.*, 2:554–574, 1957.

T. B. Benjamin. Shearing flow over a wavy boundary. *J. Fluid Mech.*, 6:161–205, 1959.

D. J. Benney. Long waves on liquid films. *J. Math. Phys.*, 45:150–155, 1966.

A. L. Bertozzi and M. P. Brenner. Linear stability and transient growth in driven contact lines. *Phys. Fluids*, 9:530, 1997.

O. Bliznyuk, E. Vereshchagina, E. S. Kooij, and B. Poelsema. Scaling of anisotropic droplet shapes on chemically stripe-patterned surfaces. *Phys. Rev. E*, 79:041601, 2009.

R. Blossey. Self-cleaning surfaces–virtual realities. *Nature Mater.*, 2:301, 2003.

D. Bonn, J. Eggers, J. Indekeu, J. Meunier, and E. Rolley. Wetting and spreading. *Rev. Mod. Phys.*, 81:739, 2009.

P. A. M. Boomkamp and R. H. M. Miesen. Classification of instabilities in parallel two-phase flow. *Intl J. Multiphase Flow*, 22:67–88, 1996.

P. A. M. Boomkamp, B. J. Boersma, R. H. M. Miesen, and G. V. Beijnon. A Chebyshev collocation method for solving two-phase flow stability problems. *J. Comput. Phys.*, 132:191–200, 1997.

S. Brandon and A. Marmur. Simulation of contact angle hysteresis on chemically heterogeneous surfaces. *J. Colloid Interface Sci.*, 183:351–355, 1996.

L. Brevdo, P. Laure, F. Dias, and T. J. Bridges. Linear pulse structure and signalling in a film flow on an inclined plane. *J. Fluid Mech.*, 396:37–71, 1999.

R. Briggs. *Electron–Stream Interactions with Plasmas.* MIT Press, 1964.

F. Brochard. Motions of droplets on solid surfaces induced by chemical or thermal gradients. *Langmuir*, 5:432, 1989.

J. W. M. Bush and D. L. Hu. Walking on water: biolocomotion at the interface. *Annu. Rev. Fluid Mech.*, 38:339–369, 2006.

A. B. D. Cassie. Contact angles. *Discuss. Faraday Soc.*, 3:11–16, 1948.

H.-C. Chang and E. A. Demekhin. *Complex wave dynamics on thin films.* Elsevier, 2002.

H.-C. Chang, E. A. Demekhin, and E. N. Kalaidin. Interaction dynamics of solitary waves on a falling film. *J. Fluid Mech.*, 294:123–154, 1995.

H. Chaté and P. Manneville. Phase diagram of the two-dimensional complex Ginzburg-Landau equation. *Physica A*, 224:348–368, 1996.

M. K. Chaudhury and G. M. Whitesides. How to make water run uphill. *Science*, 256: 1539, 1992.

K. H. Chu, R. Xiao, and E. N. Wang. Uni-directional liquid spreading on asymmetric nanostructured surfaces. *Nature Mater.*, 9:413, 2010.

L. S. Cohen and T. J. Hanratty. Generation of waves in the concurrent flow of air and a liquid. *AIChE J.*, 11:138–144, 1965.

R. G. Cox. The dynamics of the spreading of liquids on a solid surface. Part 1. Viscous flow. *J. Fluid Mech.*, 168:169, 1986.

A. D. D. Craik. Wind generated waves in thin liquid films. *J. Fluid Mech.*, 26:369 – 392, 1966.

R. V. Craster and O. K. Matar. Dynamics and stability of thin liquid films. *Rev. Mod. Phys.*, 81:1131, 2009.

R. Crawford, L. K. Koopal, and J. Ralston. Contact angles on particles and plates. *Colloids and Surfaces*, 27:57, 1987.

V. Cristini and Y. C. Tan. Theory and numerical simulation of droplet dynamics in complex flow – a review. *Lab Chip*, 4:257–264, 2004.

T. Cubaud and M. Fermigier. Advancing contact lines on chemically patterned surfaces. *J. Colloid Interface Sci.*, 269:171, 2004.

A. A. Darhuber and S. M. Troian. Principles of microfluidic actuation by modulation of surface stresses. *Annu. Rev. Fluid Mech.*, 37:425, 2005.

P.-G. de Gennes. Wetting: statics and dynamics. *Rev. Mod. Phys.*, 57:827, 1985.

P.-G. de Gennes, F. Brochard-Wyart, and D. Queré. *Capillarity and wetting phenomena: Drops, bubbles, pearls, waves*. Springer, 2004.

C. Decamps and J. De Coninck. Dynamics of spontaneous spreading under electrowetting conditions. *Langmuir*, 16:10150, 2000.

R. D. Deegan, O. Bakajin, T. F. Dupont, G. Huber, S. R. Nagel, and T. A. Witten. Capillary flow as the cause of ring stains from dried liquid drops. *Nature*, 389:827–829, 1997.

E. A. Demekhin. Nonlinear waves in a liquid film entrained by a turbulent gas stream. *Fluid Dyn.*, 16:188–193, 1981.

E. A. Demekhin, E. N. Kalaidin, S. Kalliadasis, and S. Yu. Vlaskin. Three-dimensional localized coherent structures of surface turbulence: Model validation with experiments and further computations. *Phys. Rev. E*, 82:036322, 2010.

G. F. Dietze and C. Ruyer-Quil. Wavy liquid films in interaction with a confined laminar gas flow. *J. Fluid Mech.*, 722:348–393, 2013.

E. B. Dussan. On the spreading of liquids on solid surfaces: static and dynamic contact lines. *Annu. Rev. Fluid Mech.*, 11:371, 1979.

P. Ehrhard and S. H. Davis. Non-isothermal spreading of liquid drops on horizontal plates. *J. Fluid Mech.*, 229:365, 1991.

A. S. Fokas and D. T. Papageorgiou. Absolute and Convective Instability for Evolution PDEs on the Half-Line. *Stud. Appl. Math.*, 114:95–114, 2005.

A. M. Frank. Shear driven solitary waves on a liquid film. *Phys. Rev. E*, 74:065301, 2006.

L. Gao and T. J. McCarthy. How Wenzel and Cassie were wrong. *Langmuir*, 23:3762, 2007.

L. Gao and T. J. McCarthy. An attempt to correct the faulty intuition perpetuated by the Wenzel and Cassie "laws". *Langmuir*, 25:7249, 2009.

M. Gaster. A note on the relation between temporally-increasing and spatially-increasing disturbances in hydrodynamic stability. *J. Fluid Mech.*, 14:222–224, 1962.

H. Gau, S. Herminghaus, P. Lenz, and R. Lipowsky. Liquid morphologies on structured surfaces: from microchannels to microchips. *Science*, 283:46, 1999.

K. B. Glasner and T. P. Witelski. Coarsening dynamics of dewetting films. *Phys. Rev. E*, 67:016302, 2003.

K. B. Glasner and T. P. Witelski. Collision versus collapse of droplets in coarsening of dewetting thin films. *Physica D*, 209:80–104, 2005.

K.B. Glasner. A boundary integral formulation of quasi-steady fluid wetting. *J. Comp. Phys.*, 207:529, 2005.

H. P. Greenspan. On the motion of a small viscous droplet that wets a surface. *J. Fluid Mech.*, 84:125, 1978.

R. J. Gumerman and G. M. Homsy. The stability of radially bounded thin films. *Chem. Engng Comm.*, 2:27–36, 1975.

T. J. Hanratty and J. M. Engen. Interaction between a turbulent air stream and a moving water surface. *AIChE J.*, 3:299–304, 1957.

D. Herde, U. Thiele, S. Herminghaus, and M. Brinkmann. Driven large contact angle droplets on chemically heterogeneous substrates. *Europhys. Lett.*, 100:16002, 2012.

S. Herminghaus. Roughness-induced non-wetting. *Europhys. Lett.*, 52:165, 2000.

F. Heslot, A. M. Cazabat, P. Levinson, and N. Fraysse. Experiments on wetting on the scale of nanometers: Influence of the surface energy. *Phys. Rev. Lett.*, 65:599, 1990.

E. J. Hinch. *Perturbation Methods*. Cambridge University Press, 1991.

L. M. Hocking. The spreading of a thin drop by gravity and capillarity. *Q. J. Mech. Appl. Math.*, 36:55, 1983.

J. J. Huang, C. Shu, and Y. T. Chew. Numerical investigation of transporting droplets by spatiotemporally controlling substrate wettability. *J. Colloid Interface Sci.*, 328:124, 2008.

P. Huerre. Open shear flow instabilities. In *Perspectives in Fluid Dynamics: a Collective Introduction to Current Research* (eds. G.K. Batchelor, H.K. Moffatt & M.G. Worster). Cambridge University Press, 2000.

P. Huerre and P. A. Monkewitz. Local and global instabilities in spatially developing flows. *Annu. Rev. Fluid Mech.*, 22:473–537, 1990.

C. Huh and L. E. Scriven. Hydrodynamic model of steady movement of a solid/liquid/fluid contact line. *J. Colloid Interface Sci.*, 35:85, 1971.

H. E. Huppert. Propagation of two-dimensional and axisymmetric viscous gravity currents over a rigid horizontal surface. *J. Fluid Mech.*, 121:43–58, 1982.

K. Ichimura, S. K. Oh, and M. Nakagawa. Light-driven motion of liquids on a photoresponsive surface. *Science*, 288:1624, 2000.

D. Jacqmin. Contact-line dynamics of a diffuse fluid interface. *J. Fluid Mech.*, 402:57–88, 2000.

S. Jayanti, A. Tokarz, and G. F. Hewitt. Theoretical investigation of the diameter effect on flooding in countercurrent flow. *Int. J. Multiphase Flow*, 22:307–324, 1996.

J. F. Joanny and P.-G. de Gennes. A model for contact angle hysteresis. *J. Chem. Phys.*, 81:552, 1984.

K. John, M. Bär, and U. Thiele. Self-propelled running droplets on solid substrates driven by chemical reactions. *Eur. Phys. J. E*, 18:183–199, 2005.

S. W. Joo and S. H. Davis. Instabilities of three-dimensional viscous falling films. *J. Fluid Mech.*, 242:529–547, 1992.

D. D. Joseph, R. Bai, K. P. Chen, and Y. Y. Renardy. Core-annular flows. *Ann. Rev. Fluid Mech.*, 29:65–90, 1997.

M. P. Juniper. The effect of confinement on the stability of two-dimensional shear flows. *J. Fluid Mech.*, 565:171–195, 2006.

L. A. Jurman and M. J. McCready. Study of waves on thin liquid films sheared by turbulent gas flows. *Phys. Fluids A*, 1:522–536, 1989.

S. Kalliadasis, C. Bielarz, and G. M. Homsy. Steady free-surface thin film flows over topography. *Phys. Fluids*, 12:1889, 2000.

S. Kalliadasis, E. A. Demekhin, C. Ruyer-Quil, and M. G. Velarde. Thermocapillary instability and wave formation on a film falling down a uniformly heated plane. *J. Fluid Mech.*, 492:303–338, 2003.

S. Kalliadasis, C. Ruyer-Quil, B. Scheid, and M. G. Velarde. *Falling Liquid Films*. Applied Mathematical Sciences. Springer, 2012.

P. L. Kapitza. *Collected Papers of P. L. Kapitza*, pages 662–689. Pergamon (Oxford), 1965.

H. B. Keller. *Numerical solution of bifurcation and nonlinear eigenvalue problems*. Academic Press, 1977.

P. G. Kim and H. A. Stone. Dynamics of the formation of antibubbles. *Europhys. Lett.*, 83:54001, 2008.

I. L. Kliakhandler. Long interfacial waves in multilayer thin films and coupled KuramotoSivashinsky equations. *J. Fluid Mech.*, 391:45–65, 1999.

H. Kusamaataja and J. M. Yeomans. Modeling contact angle hysteresis on chemically patterned and superhydrophobic surfaces. *Langmuir*, 23:6019, 2007.

S. T. Larsen and R. Taboryski. A Cassie-like law using triple phase boundary line fractions for faceted droplets on chemically heterogeneous surfaces. *Langmuir*, 25:1282, 2009.

J. C. Lasheras and E. J. Hopfinger. Liquid jet instability and atomization in a coaxial gas stream. *Ann. Rev. Fluid Mech.*, 32:275 – 308, 2000.

J. Lèopoldés and D. G. Bucknall. Droplet spreading on microstriped surfaces. *J. Phys. Chem. B*, 109:8973, 2005.

S. P. Lin. Finite amplitude side-band stability of a viscous film. *J. Fluid Mech.*, 63: 417–429, 1974.

S. P. Lin. *Breakup of liquid sheets and jets.* Cambridge University Press, 2003.

T. S. Lin and L. Kondic. Thin films flowing down inverted substrates: Two dimensional flow. *Phys. Fluids*, 22:052105, 2010.

J. S. Lioumbas, S. V. Paras, and A. J. Karabelas. Co-current stratified gas-liquid downflow – Influence of the liquid flow field on interfacial structure. *Int. J. Multiphase Flow*, 31: 869 – 896, 2005.

J. S. Lioumbas, A. A. Mouza, and S. V. Paras. Effect of surfactant additives on co-current gas-liquid downflow. *Chem. Engng Sci.*, 61:4605 – 4616, 2006.

J. S. Lioumbas, C. Kolimenos, and S. V. Paras. Liquid layer characteristics in gas-liquid flow in slightly inclined pipes: Effect of non-ionic surfactant additives. *Chem. Engng Sci.*, 64:5162 – 5172, 2009.

J. Liu and J. P Gollub. Solitary wave dynamics of film flows. *Phys. Fluids*, 6:1702–1712, 1994.

N. A. Malamataris and V. Balakotaiah. Flow structure underneath the large amplitude waves of a vertically falling film. *AIChE J*, 54:1725 –1740, 2008.

N. A. Malvadkar, M. J. Hancock, K. Sekeroglu, W. J. Dressick, and M. C. Demirel. An engineered anisotropic nanofilm with unidirectional wetting properties. *Nature Mater.*, 9:1023, 2010.

A. Marmur and E. Bittoun. When Wenzel and Cassie are right: reconciling local and global considerations. *Langmuir*, 25:1277, 2009.

B. J. Matkowsky and G. I. Sivashinsky. Propagation of a pulsating reaction front in solid fuel combustion. *SIAM J. Appl. Math.*, 35:465–478, 1978.

G. McHale. Cassie and Wenzel: were they really so wrong? *Langmuir*, 23:8200, 2007.

G. McHale, M. I. Newton, S. M. Rowan, and M. Banerjee. The spreading of small viscous stripes of oil. *J. Phys. D: Appl. Phys.*, 28:1925, 1995.

K. W. McQuillan, P. B. Whalley, and G. F. Hewitt. Flooding in vertical two-phase flow. *Int. J. Multiphase Flow*, 11:741–760, 1985.

R. Miesen and B. J. Boersma. Hydrodynamic stability of a sheared liquid film. *J. Fluid Mech.*, 301:175–202, 1995.

J. W. Miles. On generation of surface waves by shear flows. *J. Fluid Mech.*, 3:185 – 204, 1957.

J. A. Moriarty, L. W. Schwartz, and E. O. Tuck. Unsteady spreading of thin liquid films with small surface tension. *Phys. Fluids A: Fluid Dynamics*, 3:733, 1991.

S. Moulinet, C. Guthmann, and E. Rolley. Roughness and dynamics of a contact line of a viscous fluid on a disordered substrate. *Eur. Phys. J. E.*, 8:437, 2002.

F. Mugele, A. Klingner, J. Buehrle, D. Steinhauser, and S. Herminghaus. Electrowetting: a convenient way to switchable wettability patterns. *J. Phys. Condens. Matter*, 17:S559, 2005.

W. W. Mullins and S. F. Sekerka. Stability of a planar interface during solidification of a dilute binary alloy. *J. Appl. Phys.*, 35:444–451, 1964.

C. L. Navier. Mèmoire sur les lois du mouvement des fluides. *Mem. Acad. Sci. Inst. Fr.*, 6:389–440, 1823.

P. Neogi and C. A. Miller. Spreading kinetics of a drop on a smooth solid surface. *J. Colloid Interface Sci.*, 86:525, 1982.

Z. Nie and E. Kumacheva. Patterning surfaces with functional polymers. *Nature Mater.*, 7:277, 2008.

M. Nosonovsky. On the range of applicability of the Wenzel and Cassie Equations. *Langmuir*, 23:9919, 2007.

L Ó Náraigh, P. D. M Spelt, and T. A Zaki. Turbulent flow over a liquid layer revisited: multi-equation turbulence modelling. *J. Fluid Mech.*, 683:357–394, 2011.

L Ó Náraigh, P. D. M Spelt, and S. J. Shaw. Absolute linear instability in laminar and turbulent gas–liquid two-layer channel flow. *J. Fluid Mech.*, 714:58–94, 2013.

T. Ooshida. Surface equation of falling film flows with moderate Reynolds number and large but finite Weber number. *Phys. Fluids*, 11:3247, 1999.

A. Oron, S. H. Davis, and S. G. Bankoff. Long-scale evolution of thin liquid films. *Rev. Mod. Phys.*, 69:931, 1997.

S. A. Orszag. Accurate solution of the Orr-Sommerfeld stability equation. *J. Fluid Mech.*, 50:689–703, 1971.

M. V. Panchagnula and S. Vedantam. Comment on how Wenzel and Cassie were wrong by Gao and McCarthy. *Langmuir*, 23:13242, 2007.

M. N. Pantzali, A. A. Mouza, and S. V. Paras. Counter-current gas–liquid flow and incipient flooding in inclined small diameter tubes. *Chem. Engng Sci.*, 63:3966–3978, 2008.

C.-A. Peng, L. A. Jurman, and M. J. McCready. Formation of solitary waves on gas-sheared liquid layers. *Int. J. Multiphase Flow*, 17:767–782, 1991.

A. Pereira and S. Kalliadasis. Dynamics of a falling film with solutal Marangoni effect. *Phys. Rev. E*, 78:036312, 2008.

A. Pereira and S. Kalliadasis. Equilibrium gas–liquid–solid contact angle from density-functional theory. *J. Fluid Mech.*, 692:53, 2012.

L. M. Pismen and Y. Pomeau. Mobility and interactions of weakly nonwetting droplets. *Phys. Fluids*, 16:2604, 2004.

L. M. Pismen and U. Thiele. Asymptotic theory for a moving droplet driven by a wettability gradient. *Phys. Fluids*, 18:042104, 2006.

M. S. Plesset and A. Prosperetti. Bubble dynamics and cavitation. *Annu. Rev. Fluid Mech.*, 9:145–185, 1977.

M. N. Popescu, G. Oshanin, S. Dietrich, and A. M. Cazabat. Precursor films in wetting phenomena. *J. Phys. Condens. Matter*, 24:243102, 2012.

C. Pozrikidis. Instability of multi-layer channel and film flows. *Adv. Appl. Mech.*, 40: 179–239, 2004.

A. Pumir, P. Manneville, and Y. Pomeau. On solitary waves running down an inclined plane. *J. Fluid Mech.*, 135:27–50, 1983.

D. Queré. Non-sticking drops. *Rep. Prog. Phys.*, 68:2495, 2005.

D. Queré. Wetting and roughness. *Annu. Rev. Mater. Res.*, 38:71–99, 2008.

M. Renardy, Y. Renardy, and J. Li. Numerical simulation of moving contact line problems using a volume-of-fluid method. *J. Comp. Phys.*, 171:243–263, 2001.

O. Reynolds. On the Theory of Lubrication and Its Application to Mr. Beauchamp Tower's Experiments, Including an Experimental Determination of the Viscosity of Olive Oil. *Proc. R. Soc. London*, 40:191–203, 1886.

E. Ruckenstein and C. S. Dunn. Slip velocity during wetting of solids. *J. Colloid Interface Sci.*, 59:135–138, 1977.

C. Ruyer-Quil and P. Manneville. Modeling film flows down inclined planes. *Eur. Phys. J. B*, 6:277–292, 1998.

C. Ruyer-Quil and P. Manneville. Improved modeling of flows down inclined planes. *Eur. Phys. J. B*, 15:357–369, 2000.

N. Savva and S. Kalliadasis. Two-dimensional droplet spreading over topographical substrates. *Phys. Fluids*, 21:092102, 2009.

N. Savva and S. Kalliadasis. Dynamics of moving contact lines: A comparison between slip and precursor film models. *Europhys. Lett.*, 94:64004, 2011.

N. Savva, S. Kalliadasis, and G. A. Pavliotis. Two-dimensional droplet spreading over random topographical substrates. *Phys. Rev. Lett.*, 104:084501, 2010.

N. Savva, G. A. Pavliotis, and S. Kalliadasis. Contact lines over random topographical substrates. Part 2. Dynamics. *J. Fluid Mech.*, 672:358, 2011a.

N. Savva, G. A. Pavliotis, and S. Kalliadasis. Contact lines over random topographical substrates. Part 1. Statics. *J. Fluid Mech.*, 672:384, 2011b.

B. Scheid, C. Ruyer-Quil, S. Kalliadasis, M. G. Velarde, and R. Kh. Zeytounian. Thermocapillary long waves in a liquid film flow. Part 2. Linear stability and nonlinear waves. *J. Fluid Mech.*, 538:223–244, 2005a.

B. Scheid, C. Ruyer-Quil, U. Thiele, O. A. Kabov, J. C. Legros, and P. Colinet. Validity domain of the Benney equation including the Marangoni effect for closed and open flows. *J. Fluid Mech.*, 527:303–335, 2005b.

B. Scheid, C. Ruyer-Quil, and P. Manneville. Wave patterns in film flows: modelling and three-dimensional waves. *J. Fluid Mech.*, 562:183–222, 2006.

H. Schlichting. *Boundary-Layer Theory.* Springer, 2000.

L. W. Schwartz and R. R. Eley. Simulation of droplet motion on low-energy and heterogeneous surfaces. *J. Colloid Interface Sci.*, 202:173, 1998.

P. Seppecher. Moving contact lines in the Cahn-Hilliard theory. *Int. J. Engng. Sci*, 34: 977–992, 1996.

A. Sharma. Relationship of thin film stability and morphology to macroscopic parameters of wetting in the apolar and polar systems. *Langmuir*, 9:861–869, 1993.

Y. D. Shikhmurzaev. The moving contact line on a smooth solid surface. *Int. J. Multiphase Flow*, 19:589–610, 1993.

V. Ya. Shkadov. Wave flow regimes of a thin layer of viscous fluid subject to gravity. *Fluid Dyn.*, 2:29–34, 1967.

D. Sibley, A. Nold, N. Savva, and S. Kalliadasis. The contact line behaviour of solid-liquid-gas diffuse-interface models. *Phys. Fluids*, 25:092111, 2013.

J. H. Snoeijer and B. Andreotti. Moving contact lines: Scales, regimes, and dynamical transitions. *Annu. Rev. Fluid Mech.*, 45:269–292, 2013.

C. Sodtke, V. S. Ajaev, and P. Stephan. Dynamics of volatile liquid droplets on heated surfaces: theory versus experiment. *J. Fluid Mech.*, 610:343, 2008.

M. A. Spaid and G.M. Homsy. Stability of Newtonian and viscoelastic dynamic contact lines. *Phys. Fluids*, 8:460, 1996.

S. A. Suslov. Numerical aspects of searching convective/absolute instability transition. *J. Comp. Phys.*, 212:188–217, 2006.

P. S. Swain and R. Lipowsky. Contact angles on heterogeneous surfaces: A new look at Cassie's and Wenzel's laws. *Langmuir*, 14:6772, 1998.

L. H. Tanner. The spreading of silicone oil drops on horizontal surfaces. *J. Phys. D: Appl. Phys.*, 12:1473, 1979.

P. Tarazona and R. Evans. A simple density functional theory for inhomogeneous liquids: Wetting by gas at a solid-liquid interface. *Mol. Phys.*, 52:847–857, 1984.

U. Thiele and E. Knobloch. Thin liquid films on a slightly inclined heated plate. *Physica D*, 190:213–248, 2004.

U. Thiele and E. Knobloch. On the depinning of a driven drop on a heterogeneous substrate. *New J. Phys.*, 8:313, 2006a.

U. Thiele and E. Knobloch. Driven drops on heterogeneous substrates: onset of sliding motion. *Phys. Rev. Lett.*, 97:204501, 2006b.

U. Thiele, K. Neuffer, M. Bestehorn, Y. Pomeau, and M. G. Velarde. Sliding drops on an inclined plane. *Colloid Surf. A*, 206:87–104, 2002.

U. Thiele, L. Brusch, M. Bestehorn, and M. Bär. Modelling thin-film dewetting on structured substrates and templates: Bifurcation analysis and numerical simulations. *Eur. Phys. J. E*, 11:255–271, 2003.

U. Thiele, K. John, and M. Bär. Dynamical model for chemically driven running droplets. *Phys. Rev. Lett.*, 93:027802, 2004.

U. Thiele, J. M. Vega, and E. Knobloch. Long-wave Marangoni instability with vibration. *J. Fluid Mech.*, 546:61–87, 2006.

P. A. Thompson and S. M. Troian. A general boundary condition for liquid flow at solid surfaces. *Nature*, 389:360–362, 1997.

C.B. Thorsness, P.E. Morrisroe, and T.J. Hanratty. A comparison of linear theory with measurements of the variation of shear stress along a solid wave. *Chem. Engng Sci.*, 33: 579 – 592, 1978.

B. S. Tilley, S. H. Davis, and S. G. Bankoff. Linear stability theory of two-layer fluid flow in an inclined channel. *Phys. Fluids*, 6:3906, 1994a.

B. S. Tilley, S. H. Davis, and S. G. Bankoff. Nonlinear long-wave stability of superposed fluids in an inclined channel. *J. Fluid Mech.*, 277:55–83, 1994b.

S. M. Tobias, M. R. E. Proctor, and E. Knobloch. Convective and absolute instabilities of fluid flows in finite geometry. *Physica D*, 113:43–72, 1998.

L. N. Trefethen. *Spectral methods in MATLAB*. SIAM, Philadelphia, 2000.

P. M. J. Trevelyan and S. Kalliadasis. Dynamics of a reactive falling film at large Péclet numbers. II. Nonlinear waves far from criticality: Integral-boundary-layer approximation. *Phys. Fluids*, 16:3209–3226, 2004.

P. M. J. Trevelyan, S. Kalliadasis, J. H. Merkin, and S. K. Scott. Dynamics of a vertically falling film in the presence of a first-order chemical reaction. *Phys. Fluids*, 14:2402, 2002.

P. M. J. Trevelyan, A. Pereira, and S. Kalliadasis. Dynamics of a reactive thin film. *Math. Model. Nat. Phenom.*, 7:99–145, 2012.

Yu. Ya. Trifonov. Counter-current gas-liquid wavy film flow between the vertical plates analyzed using the Navier-Stokes equations. *AIChE J.*, 56:1975–1987, 2010.

D. Tseluiko and S. Kalliadasis. Nonlinear waves in counter-current gas-liquid film flow. *J. Fluid Mech.*, 673:19–59, 2011.

D. Tseluiko and D. T. Papageorgiou. Wave evolution on electrified falling films. *J. Fluid Mech.*, 556:361–386, 2006.

D. Tseluiko and D. T. Papageorgiou. Nonlinear dynamics of electrified thin liquid films. *SIAM J. Appl. Math.*, 67:1310–1329, 2007.

E. R. Van Driest. On turbulent flow near a wall. *J. Aerospace Sci.*, 23:1007–1011, 1956.

S. Varagnolo, D. Ferraro, P. Fantinel, M. Pierno, G. Mistura, G. Amati, L. Biferale, and M. Sbragaglia. Stick-slip sliding of water drops on chemically heterogeneous surfaces. *Phys. Rev. Lett.*, 111:066101, 2013.

M. G. Velarde. A few perliminary remarks, quotations and some references. *Eur. Phys. J. ST*, 197:3–9, 2011.

R. Vellingiri, N. Savva, and S. Kalliadasis. Droplet spreading on chemically heterogeneous substrates. *Phys. Rev. E*, 84:036305, 2011.

R. Vellingiri, D. Tseluiko, N. Savva, and S. Kalliadasis. Dynamics of a liquid film sheared by a co-flowing turbulent gas. *Int. J. Multiphase Flow*, 56:93–104, 2013.

M. Vlachogiannis and V. Bontozoglou. Observations of solitary wave dynamics of film flows. *J. Fluid Mech.*, 435:191–215, 2001.

M. Vlachogiannis and V. Bontozoglou. Experiments on laminar film flow along a periodic wall. *J. Fluid Mech.*, 457:133–156, 2002.

O. V. Voinov. Hydrodynamics of wetting. *Fluid Dyn.*, 11:714, 1976.

P. C. Wayner. Spreading of a liquid film with a finite contact angle by the evaporation/condensation process. *Langmuir*, 9:294–299, 1993.

H. Wong, I. Fatt, and C. J. Radke. Deposition and thinning of the human tear film. *J. Colloid Interface Sci.*, 184:44–51, 1996.

D. E. Woodmansee and T. J. Hanratty. Mechanism for the removal of droplets from a liquid surface by a parallel air flow. *Chem. Engng Sci.*, 24:299 – 307, 1969.

J. T. Woodward, H. Gwin, and D. K. Schwartz. Contact angles on surfaces with mesoscopic chemical heterogeneity. *Langmuir*, 16:2957, 2000.

G. Yamauchi, J. D. Miller, H. Saito, K. Takai, T. Ueda, H. Takazawa, H. Yamamoto, and S. Nislhi. Wetting characteristics of newly developed water-repellent material. *Colloids Surf. A*, 116:125, 1996.

C. S. Yih. Stability of a liquid flow down an inclined plane. *Phys. Fluids*, 6:321–334, 1963.

T. Young. An essay on the cohesion of fluids. *Philos. Trans. R. Soc. London*, 95:65–87, 1805.

A. Zapke and D. G. Kröger. Countercurrent gas-liquid flow in inclined and vertical ducts – I: Flow patterns, pressure drop characteristics and flooding. *Int. J. Multiphase Flow*, 26:1439 – 1455, 2000a.

A. Zapke and D. G. Kröger. Countercurrent gas-liquid flow in inclined and vertical ducts – II: The validity of the Froude–Ohnesorge number correlation for flooding. *Int. J. Multiphase Flow*, 26:1457 – 1468, 2000b.

D. P. Zilker, G. W. Cook, and T. J. Hanratty. Influence of the amplitude of a solid wavy wall on a turbulent flow. Part 1. Non-separated flows. *J. Fluid Mech.*, 82:29–51, 1977.

A. Integrated form of the governing equation

The central idea is to convert the free boundary problem to a fixed boundary problem and then make use of spectral methods to solve it numerically as done for topographical substrates in Savva and Kalliadasis (2009). By making a transformation $y = [2x - (a+b)]/(a-b)$, equation (2.35) can be re-written as

$$\partial_t h - \frac{\dot{a}\,(1+y) + \dot{b}\,(1-y)}{a-b}\,(\partial_y h) + \left(\frac{2}{a-b}\right)^4 \partial_y\left[h^2\,(h+\lambda)\,\partial_{yyy} h\right] = 0. \tag{A.1}$$

This mapping of a free boundary problem to a fixed boundary problem introduces two more unknowns a and b in the equation, requiring two more boundary conditions to completely define the system. The boundary conditions in the transformed domain are:

$$h\big|_{y=\pm 1} = 0, \tag{A.2a}$$

$$(\partial_y h)\,\big|_{y=\pm 1} = \mp\frac{a-b}{2} g\big|_{a,b}, \tag{A.2b}$$

$$\dot{a} = \lambda\left(\frac{2}{a-b}\right)^3 h\partial_{yyy} h\Big|_{y=+1}, \tag{A.2c}$$

$$\dot{b} = \lambda\left(\frac{2}{a-b}\right)^3 h\partial_{yyy} h\Big|_{y=-1}. \tag{A.2d}$$

The conditions for $\dot{a}$ and $\dot{b}$ come from the requirement that equation (A.1) is satisfied as the contact lines are approached. It can be observed from equations (A.2c)-(A.2d) that $(\partial_{yyy} h)$ needs to be singular in order for the contact line velocity to be finite. To capture this behaviour, we consider the integral of equation (A.1) with respect to y. By setting

$\mathscr{H} = \int h dy$, equation (A.1) can be written as:

$$\begin{aligned}\partial_t \mathscr{H} + \frac{\dot{a} - \dot{b}}{a - b}\mathscr{H} - \frac{\dot{a}\,(1+y) + \dot{b}\,(1-y)}{a-b}\left(\partial_y \mathscr{H}\right) + \\ \left(\frac{2}{a-b}\right)^4 \left(\partial_y \mathscr{H}\right)^2 \left(\partial_y \mathscr{H} + \lambda\right)\left(\partial_{yyyy} \mathscr{H}\right) = 0.\end{aligned} \tag{A.3}$$

The boundary conditions for equation (A.3) are:

$$\mathscr{H}\big|_{y=\pm 1} = \frac{k_\pm}{a-b}, \tag{A.4a}$$

$$h\big|_{y=\pm 1} = \left.\frac{\partial \mathscr{H}}{\partial y}\right|_{y=\pm 1} = 0, \tag{A.4b}$$

$$\partial_y h\Big|_{y=\pm 1} = \partial_{yy}\mathscr{H}\Big|_{y=\pm 1} = \mp \frac{1}{2}\,(a-b)\,g_{a,b}, \tag{A.4c}$$

where the constants $k_\pm$ are specified by integrating the initial droplet shape, and has to satisfy $k_+ - k_- = 4$. An additional advantage with this formulation is that we avoid direct evaluation of $(h\partial_{yyy}h)$ at the contact lines $y = \pm 1$. In order to make direct comparisons with the solutions of equations (2.60a) and (2.60b), we choose an initial condition that satisfies $\partial_{yyy}h \sim 0$ in the bulk and has a boundary layer of thickness $\mathcal{O}(\lambda)$ near the contact lines.

B. Pseudo-arclength continuation

Let the gas-liquid system be represented in a general form as

$$\mathbf{F}(\mathbf{u}, \Lambda) = \mathbf{0}, \tag{B.1}$$

where $\mathbf{u}$ is the dependent variable, and Λ is the parameter that can be independently varied. In our problem, the parameter Λ can be the liquid Reynolds number Re, or the gas shear control parameter Θ.

Differentiating equation (B.1) with respect to Λ, we get

$$\mathbf{F}_{\mathbf{u}}(\mathbf{u}, \Lambda)\dot{\mathbf{u}} + \mathbf{F}_{\Lambda}(\mathbf{u}, \Lambda) = \mathbf{0}, \tag{B.2}$$

where dot denotes differentiation with respect to Λ. In order to implement numerical continuation, we need a very good initial guess (i.e., a point on the solution curve C). Let us take the initial condition to be $(\mathbf{u}_0, \Lambda_0)$. Therefore,

$$\mathbf{F}_{\mathbf{u}}(\mathbf{u}_0, \Lambda_0)\mathbf{r}_0 + \mathbf{F}_{\Lambda}(\mathbf{u}_0, \Lambda_0) = \mathbf{0}, \tag{B.3}$$

which can be written as,

$$\mathbf{F}^0_{\mathbf{u}}\mathbf{r}_0 + \mathbf{F}^0_{\Lambda} = \mathbf{0}. \tag{B.4}$$

Therefore,

$$\mathbf{r}_0 = -\mathbf{F}^{0\,-1}_{\mathbf{u}}\mathbf{F}^0_{\Lambda}. \tag{B.5}$$

A unit tangent vector to $\mathbf{F}(\mathbf{u}, \Lambda) = 0$, at $(\mathbf{u}_0, \Lambda_0)$ can be written as

$$\begin{bmatrix} \mathbf{p}_0 \\ m_0 \end{bmatrix} = \frac{1}{(1 + (\mathbf{r}_0)^T\mathbf{r}_0)^{1/2}} \begin{bmatrix} \mathbf{r}_0 \\ 1 \end{bmatrix}.$$

This is the Newton's prediction step. Now, we step along the tangent by a distance Δs

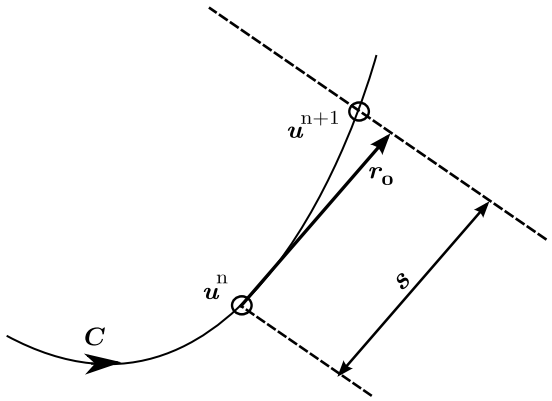

Figure B.1.: Schematic of the continuation procedure.

given by

$$\begin{bmatrix} \mathbf{u}_0{}^1 \\ \Lambda_0{}^1 \end{bmatrix} = \begin{bmatrix} \mathbf{u}_0 \\ \Lambda_0 \end{bmatrix} + \Delta s \begin{bmatrix} \mathbf{p}_0 \\ m_0 \end{bmatrix},$$

where s is the arclength parameter. Our next objective is to find a point on the curve $(\mathbf{u}_1, \Lambda_1) \in C$, at which the plane perpendicular to the tangent intersects the curve. In order to achieve this, we need to consider an extended system,

$$\mathbf{G}(\mathbf{u}, \Lambda, s) = \begin{bmatrix} \mathbf{F}(\mathbf{u}, \Lambda) \\ \mathbf{p}_0{}^T(\mathbf{u} - \mathbf{u}_0) + m_0(\Lambda - \Lambda_0) - (s - s_0) \end{bmatrix} = \begin{bmatrix} \mathbf{0} \\ 0 \end{bmatrix}, \tag{B.6}$$

where the equation in the second row is the arclength equation. The above system (B.6) can be solved using the Newton's method, which is also called the correction step, and is given by

$$\begin{bmatrix} \mathbf{u}_1{}^{k+1} \\ \Lambda_1{}^{k+1} \end{bmatrix} - \begin{bmatrix} \mathbf{u}_1{}^k \\ \Lambda_1{}^k \end{bmatrix} = \mathbf{J}_k^{-1}\mathbf{G}(\mathbf{u}_1{}^k, \Lambda_1{}^k), \tag{B.7}$$

where, $(\mathbf{u}_1{}^k, \Lambda_1{}^k)$ is the solution at the k^{th} iteration, and $\mathbf{J}$ is the Jacobian matrix evaluated at $(\mathbf{u}_1{}^k, \Lambda_1{}^k)$ given by

$$\mathbf{J} = \begin{bmatrix} \mathbf{F}_\mathbf{u} & \mathbf{F}_\Lambda \\ \mathbf{p}_0{}^T & m_0 \end{bmatrix}. \tag{B.8}$$

In our problem, the matrix $\mathbf{F}_\mathbf{u}$ is computed numerically at each step due to a nonlocal contribution arising from $\hat{\tau}_{w1}[h]$.

C. Numerical scheme for direct numerical simulation of the WIBL model

In order to solve the one dimensional WIBL model ((3.58) - (3.59)) as an initial value problem on a periodic domain, we use spectral differentiation in space and a finite difference scheme in time. Equations (3.58) and (3.59) can be written in a general form as

$$\partial_t (h, q)^{\mathrm{T}} = \mathbf{F}(h, q, h_x, q_x, h_{xxx}, \ldots), \tag{C.1}$$

where $\mathbf{F}$ is usually nonlinear. By discretising the system (C.1) in the spatial direction using a Fourier pseudo-spectral scheme, we obtain a coupled system of nonlinear ODEs in time. Such an analysis is usually referred to as the method of lines. To begin with, the discrete Fourier transform of $h(x,t)$ is defined as

$$\hat{h}_k(t) = \frac{2\pi}{N} \sum_{j=-\frac{N}{2}}^{\frac{N}{2}-1} h_j(t) \mathrm{e}^{-\mathrm{i}kj\left(\frac{2\pi}{N}\right)}, \tag{C.2}$$

and the inverse discrete Fourier transform is given by

$$h_j(t) = \frac{1}{2\pi} \sum_{k=-\frac{N}{2}}^{\frac{N}{2}-1} \hat{h}_k(t) \mathrm{e}^{\mathrm{i}kj\left(\frac{2\pi}{N}\right)}. \tag{C.3}$$

In order to compute the first derivative, $\partial_x h(t)$, we make use of the property of the Fourier transform, and simply multiply $\hat{h}_k(t)$ with $\frac{2\pi \mathrm{i}k}{N}$ followed by an inverse Fourier transform of the resulting quantity, i.e.,

$$\partial_x h_j(t) = \frac{1}{N} \sum_{k=-\frac{N}{2}}^{\frac{N}{2}-1} (\mathrm{i}k) \hat{h}_k(t) \mathrm{e}^{\mathrm{i}kj\left(\frac{2\pi}{N}\right)}, \tag{C.4}$$

and its generalisation to an arbitrary derivative is straightforward. Having computed the derivatives in the Fourier space, we move back to the real space to consider the nonlinear terms. Therefore, the right hand side of equation (C.1) reduces to a nonlinear function of h and q in the real space. This system is to be solved subject to the initial condition, which is a flat film superimposed with a small amplitude sinusoidal perturbation given by

$$h(x,0) = 1 + 0.05 \sin \frac{x}{2}, \quad q(x,0) = \frac{2}{3}. \tag{C.5}$$

For the time integration of the ODEs, the Matlab integrator `ode15s` for stiff equations that employs a variable step size is used to ensure stability and accuracy. The number of modes for spatial discretisation (N) ranges from 128 to 512, and a typical time step of 0.01 or smaller with a total integration time of about 13000 time units is considered.

D. Spreading of a two-dimensional droplet in the presence of gas jet

A brief initial investigation of droplet spreading in the presence of a gas jet is provided in this Appendix. The approach followed here to include the effect of a gas that is blowing down vertically takes inspiration from Moriarty et al. (1991). As a consequence, the gas flow is modeled as a parabolic distribution in pressure, $p = p_0 - kx^2/2$, which enters the droplet dynamics through the normal stress balance. In the above equation, p_0 is the maximum gas pressure at the droplet center and k is a positive constant that signifies the strength of gas flow. As in the second chapter, we use the Navier slip condition to account for the contact line motion.

D.1. Governing equations

In the thin film approximation, it can be readily shown that the dimensionless form of the governing equation for the droplet free surface deduces to

$$\partial_t h + \partial_x \left[h^2 (h + \lambda)(\partial_{xxx} h + Kx) \right] = 0, \tag{D.1}$$

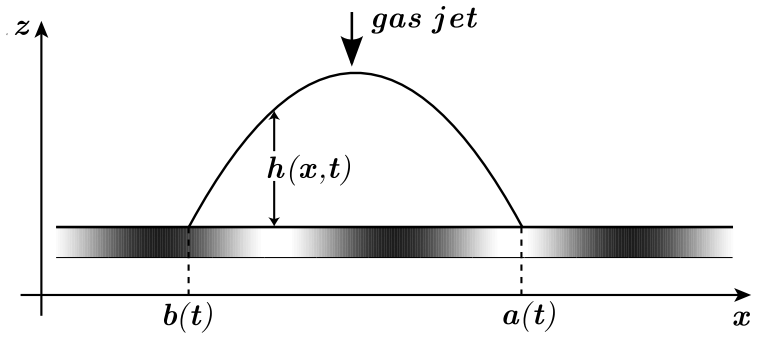

Figure D.1.: Schematic of a two-dimensional droplet spreading on a chemically heterogeneous substrate in the presence of gas jet.

where the dimensionless constant K denotes the strength of the gas jet. Equation (D.1) is supplemented by the following boundary conditions

$$h = 0 \quad \text{at} \quad x = a(t), b(t), \tag{D.2}$$

$$\partial_x h = g(b) \quad \text{at} \quad x = b(t), \tag{D.3a}$$

$$\partial_x h = -g(a) \quad \text{at} \quad x = a(t), \tag{D.3b}$$

and

$$\int_{b(t)}^{a(t)} h \, dx = 2. \tag{D.4}$$

In the limit of slow spreading, we can do an asymptotic expansion for the droplet free surface h, and obtain a leading order solution for the outer region. However, the matching of inner and outer regions results in more complex integral equations for the location of two contact points.

D.2. Numerical solution

Even though an asymptotic solution has thus far appeared intractable, we can solve the system of equations (D.1)–(D.4) numerically, by using a pseudo-spectral scheme as described in Appendix A. We present our results for two cases: one where the substrate heterogeneities are localised and the other a simple homogeneous substrate. In both these computations, the contact points of the droplet are initially located at $a(0) = -b(0) = 1$, and dimensionless slip length is taken to be $\lambda = 10^{-5}$.

First, we shall consider spreading on a localised heterogeneous substrate $g(x)$=1.0 + 2.0 [sech $20(x + 1.5)$ + sech $20(x - 1.5)$], where the heterogeneity spots are located at $x = \pm 1.5$. As the droplet starts to spread and approaches the heterogeneities, its gets pinned because of the contact angle being high at these locations, and a steady state is finally attained (figures D.2b and D.2c). As expected, the presence of the gas jet flattens the droplet free surface, and as it is sufficiently strong it also creates a dimple at the top, as can be seen from figure D.2a.

As a next setting, let us consider spreading on a homogeneous substrate, $g(x) = 1.0$. Although the initial condition of the droplet is symmetric about the z axis, we can observe from figure D.3 that the dynamics no longer remains symmetric after a finite time. This is due to the fact that the form of the forcing introduced by the gas jet renders the symmetric position of the droplet linearly unstable. As a result, it would require a better modeling

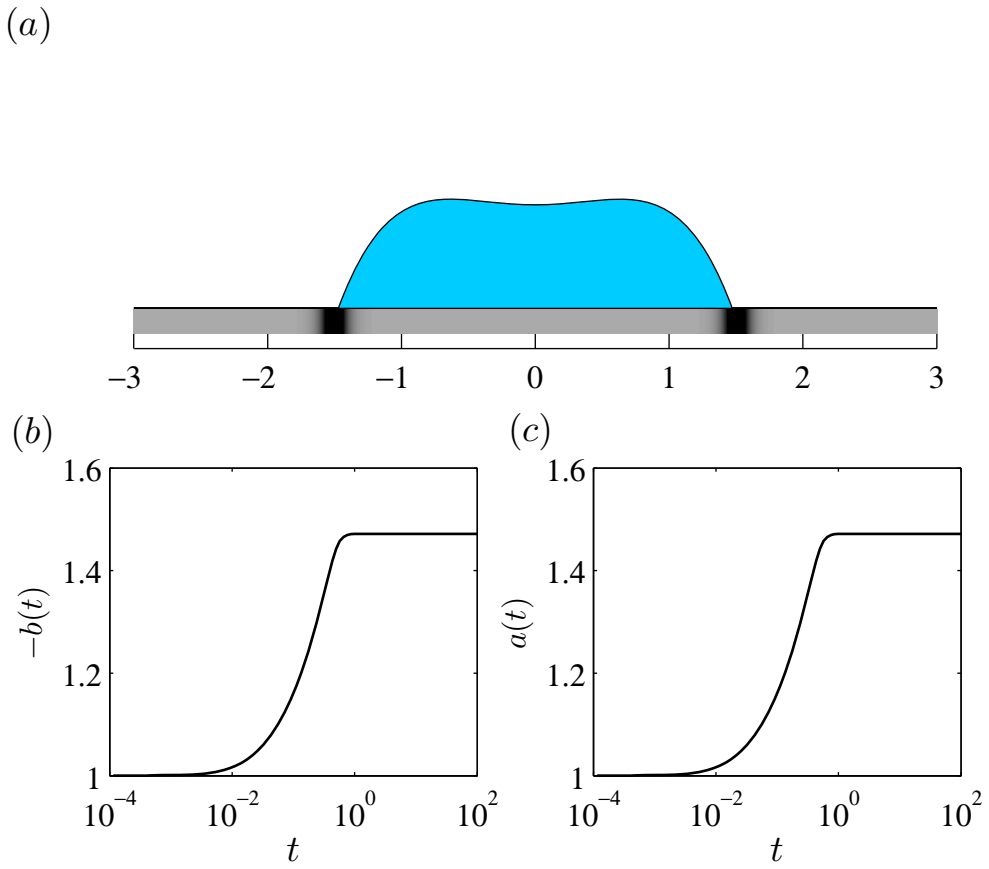

Figure D.2.: Two-dimensional droplet spreading on a localised heterogeneous substrate $g(x)$=1.0+2.0 [sech $20(x + 1.5)$ + sech $20(x - 1.5)$] in the presence of gas flow, $K = 20$, when $\lambda = 10^{-5}$ and $a(0) = -b(0) = 1$. Panel (a) shows the steady state droplet profile, whereas panels (b) and (c) depict the time-evolution of left and right contact points respectively.

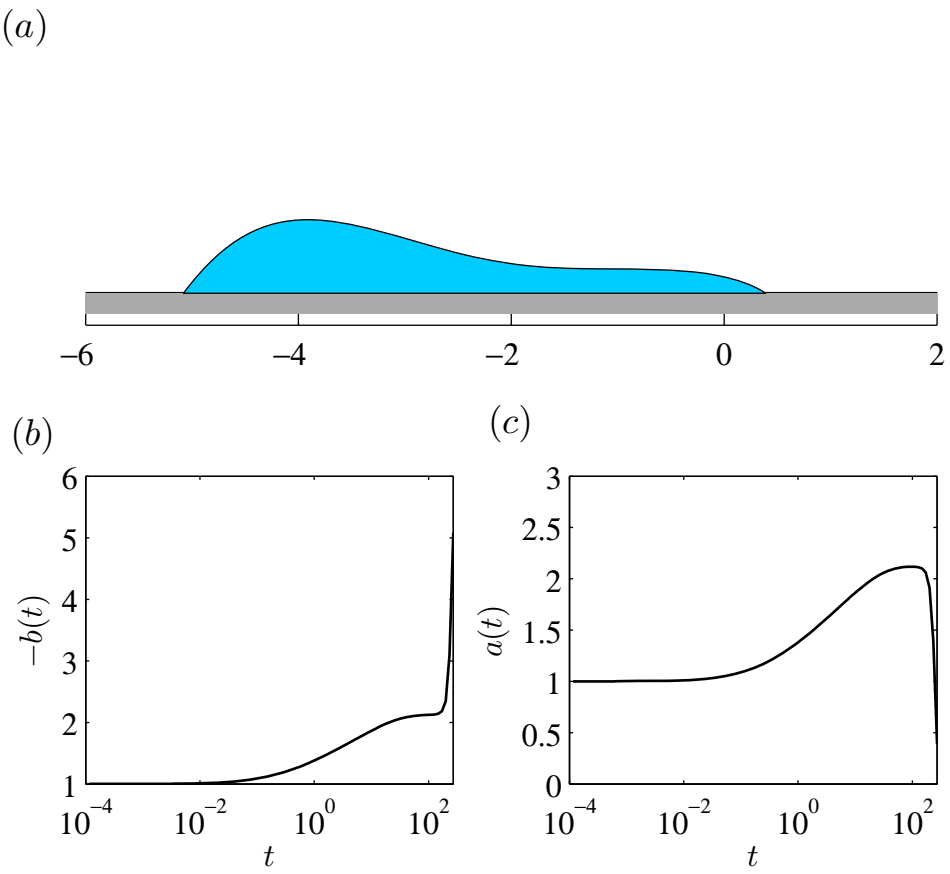

Figure D.3.: Two-dimensional droplet spreading on a homogeneous substrate $g(x)$=1.0 in the presence of gas flow, $K = 5$, when $\lambda = 10^{-5}$ and $a(0) = -b(0) = 1$. Panel (a) shows the droplet profile at $t = 270$, whereas panels (b) and (c) depict the time-evolution of left and right contact points respectively, with no steady state attained.

approach to include gas flow in the spreading dynamics of a droplet.